The merger history of the Milky Way and its dwarf galaxies

TILLY ANNE EVANS-HOFMANN

The merger history of the Milky Way and its dwarf galaxies

Using simulations to make predictions for observations

Tilly Anne Evans-Hofmann

A Thesis presented for the degree of
Doctor of Philosophy

Institute for Computational Cosmology
Ogden Centre for Fundamental Physics
Department of Physics
Durham University
United Kingdom

July 2023

The merger history of the Milky Way and its dwarf galaxies

Using simulations to make predictions for observations

Tilly Anne Evans-Hofmann

Submitted for the degree of Doctor of Philosophy

July 2023

Abstract: This thesis uses simulations to study the assembly history of the Milky Way (MW), make predictions for the upcoming James Webb Space Telescope (JWST) surveys and to identify the best regions in the universe to study the nature of dark matter using dwarf galaxies.

Chapter 2 presents the properties of simulated MW-mass halos constrained to have accretion histories similar to that of the MW, specifically the recent accretion of a Large Magellanic Cloud (LMC)-like galaxy and a merger analogous to the Gaia-Enceladus Sausage (GES), with a quiescent period between the GES merger and the infall of the LMC (the 'LMC and GES' category). We find that ∼16 per cent of MW-mass halos have an LMC; ∼5 per cent have a GES event and no further merger with an equally massive object since $z = 1$; and only 0.65 per cent belong to the LMC and GES category. The progenitors of the MWs in this last category are much less massive than average at early times but eventually catch up with the mean. The LMC and GES category of galaxies naturally end up in the 'blue cloud' in the colour–magnitude diagram at $z = 0$, tend to have a disc morphology and have a larger than average number of satellite galaxies.

Chapter 3 presents predictions, derived from the EAGLE ΛCDM cosmological hydrodynamical simulations, for the abundance and properties of galaxies expected to be detected at high redshift by JWST. We consider the galaxy population as a whole and focus on

the sub-population of progenitors of MW analogues, defined to be galaxies with accretion histories similar to the MW's, that is, galaxies that underwent a merger resembling the GES event and that contain an analogue of the LMC satellite today. We derive the luminosity function of all EAGLE galaxies in JWST/NIRCam passbands, in the redshift range $z = 2 - 8$, taking into account dust obscuration and different exposure times. For an exposure time of $T = 10^5$s, average MW progenitors are observable as far back as $z \sim 6$ in most bands, and this changes to $z \sim 5$ and $z \sim 4$ for the GES and LMC progenitors, respectively. The progenitors of GES and LMC analogues are, on average, ∼2 and ∼1 mag fainter than the MW progenitors at most redshifts. They lie, on average, within ∼60 and 30 arcsec, respectively, of their future MW host at all times, and thus will appear within the field of view of JWST/NIRCam. We conclude that galaxies resembling the main progenitor of the MW and its major accreted components should be observable with JWST beyond redshift 2, providing a new and unique window in studying the formation history of our own galaxy.

Chapter 4 studies the effect of environment on the merger rates of dark matter halos, with an emphasis on the mass regime relevant for dwarf galaxies ($M_{\rm halo} = 10^9 - 10^{11}\,{\rm M}_\odot$) in both a cold and warm dark matter cosmology. A halo's environment has been explored using two different methods, 1) probing the cosmic web geometry using the NEXUS algorithm and 2) probing the local environment using halo counts. We find that the nature of dark matter has a much bigger impact on halo mergers than any environmental differences. Low mass halos ($M_{\rm halo} = 10^9 - 10^{9.5}\,{\rm M}_\odot$) have roughly 9 (5) times more minor (major) mergers in CDM than in WDM. We also find that there are differences between the assembly histories of $10^{11} - 10^{12}\,{\rm M}_\odot$ mass halos in CDM and WDM. In CDM, halos would have experienced roughly three times more major mergers in their lifetime. The environmental impact on halo mergers affects when a halo experiences its mergers, but not how many it has in its lifetime. Furthermore, the large-scale structure has a bigger impact on early mergers, and the local environment has a bigger impact on recent mergers. We find that low mass halos ($10^9 - 10^{9.5}\,{\rm M}_\odot$) are up to four times more likely to have experienced a recent major merger in a low local environment density in CDM than in WDM. Therefore, a low density local

scale environment would be the ideal regime for observing the differences between CDM and WDM using dwarf galaxies.

Declaration

The work described in this thesis was undertaken between October 2019 and July 2023 while the author was a research student under the supervision of Dr. Alis Deason and Dr. Azadeh Fattahi in the Institute for Computational Cosmology at Durham University, England. No part of this thesis has been submitted for any degree or qualification at Durham University or elsewhere.

Chapters 2 and 3 have been published as a papers in Monthly Notices of the Royal Astronomical Society (MNRAS):

Evans T. A., Fattahi A., Deason A. J., Frenk C. S. 2020, MNRAS, **497**, 4

Evans T. A., Fattahi A., Deason A. J., Frenk C. S. 2022, MNRAS, **495**, 12

Chapter 4 is being prepared for publication.

All figures in this thesis were prepared by the author, or have been properly attributed in the figure caption.

Acknowledgements

This certainly was not the PhD experience I had imagined! The COVID-19 lockdown began 6 months into my PhD and changed everything in our lives for the best part of 2 years.

Firstly, I would like to thank my supervisory team: Alis, Azi, and Carlos, for their incredible support and guidance throughout my PhD journey. Their expertise and encouragement have been absolutely invaluable.

I would also like to thank everyone in the Galactic group for all the insightful discussions! Thank you all for being such a significant part of my PhD and for broadening my knowledge of the Milky Way, dwarf galaxies, and simulations.

A special shout-out goes to my family and friends for their unwavering love, encouragement, and belief in me. Your support during the highs and lows of this journey has meant the world to me.

Last but definitely not least, I want to say a massive thank you to my amazing husband, Beni. Your love, patience, and understanding have really helped me get through all the long hours, the bugs, and those moments of self-doubt. I simply couldn't have done this without you by my side. Thank you from the bottom of my heart.

Tilly Evans-Hofmann,

July 2023, Durham UK

Contents

List of Figures

List of Tables

CHAPTER 1

Introduction

1.1 The universe

The universe is a vast and mysterious place, and studying it can help us to better understand our place in the cosmos. By studying the universe, we can learn about its origins, its evolution, and its ultimate fate. Understanding how galaxies form and evolve relies on understanding the underlying dark matter halo.

1.1.1 Dark matter

Dark matter is responsible for everything: large-scale structure, galaxies, stars, and planets. The existence of dark matter has been theorised since as early as 1933, when Zwicky (1933) found that the baryonic matter in the Coma cluster (the stellar content) could not explain the measured velocity dispersion. If the velocity dispersion was measured correctly, then the mass of the Coma cluster needed to be over 400 times that measured by the stellar component. This missing matter was dubbed “dark matter”. The current estimate for the dark matter content in the universe is roughly 5 times that of baryonic matter (Planck Collaboration et al., 2014). Clearly the measurements by Zwicky (1933)

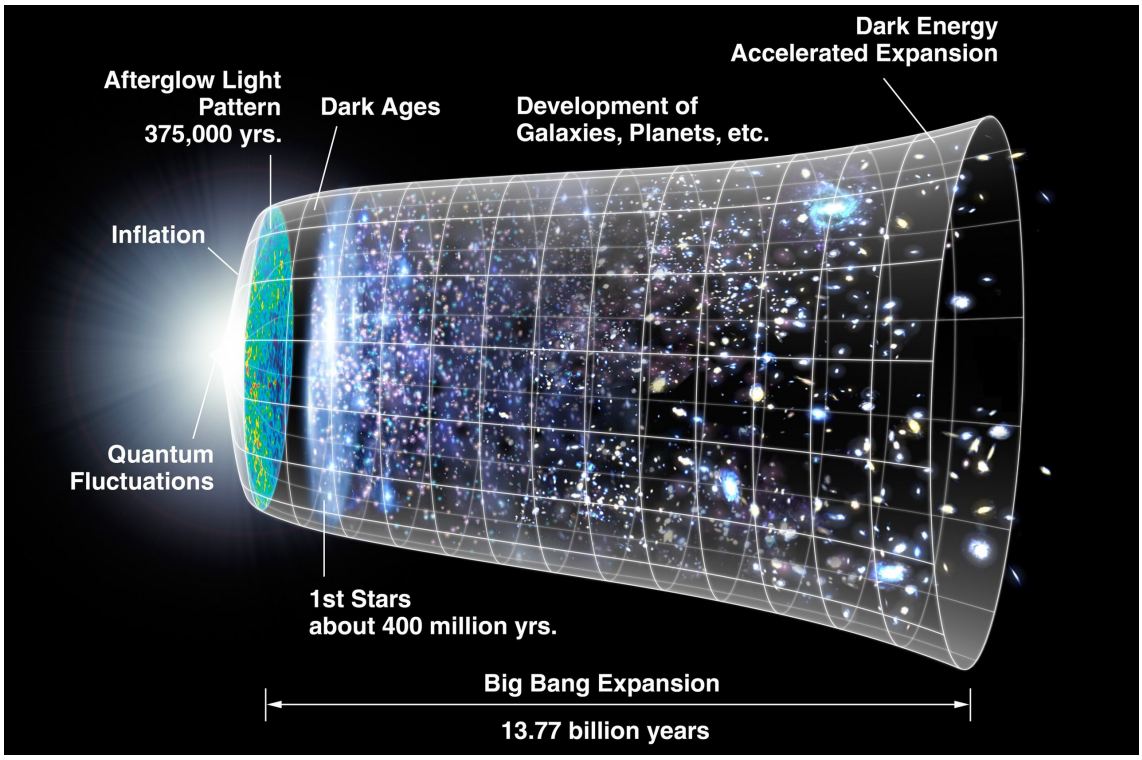

Figure 1.1
An illustration of the evolution of the universe since the big bang. Image credit: NASA

were very different from those we can achieve today. One of the reasons his estimate for the dark matter content of the Coma cluster was so much greater was because his estimate for the distance was very inaccurate due to the value of Hubble's constant at that time (where $H_0 = 558$ km s^{-1} Mpc^{-1}, meaning that Zwicky thought the Coma cluster was much closer than it is). Not only was the value of H_0 incorrect, Zwicky was also unaware of the X-ray emitting gas in the Coma cluster that he could not observe from the ground, and which contains more mass than the visible galaxies.

Dark matter became more widely accepted in the 1980s and 1990s after it was proven that the electron neutrino mass (discovered by Lyubimov et al., 1981)* could not account for the missing matter in galaxies. N-body simulations using electron neutrinos as the missing matter failed to reproduce the clustering of the universe (Frenk et al., 1983; White et al.,

*The mass estimate for the electron neutrino in this work were later found to be incorrect by Bennett et al. (1981) who found that the basis of the work in Lyubimov et al. (1981, where subshell ratios in heavy nuclei were used to extract a neutrino mass) was not adequate to estimate the mass of the neutrino. For more details about the different techniques used to measure neutrino mass see Formaggio et al. (2021, and references therein).

1983), which contradicted the results of Davis et al. (1982). The reign of the cold dark matter (CDM) model of the universe began when Davis et al. (1985) demonstrated that the clustering of the universe could only be explained if the missing matter was "cold" and beyond the scope of the standard model of physics.

The cosmic microwave background (CMB) provided strong evidence for the existence of dark matter through precise measurements of the initial temperature perturbations (Melchiorri et al., 2000; Hanany et al., 2000; Spergel et al., 2003). The CMB indicates that our universe can be assumed to be flat and isotropic on scales above $\sim$ 100 Mpc. Furthermore, the CMB reveals that dark matter accounts for approximately 85% of all matter in the universe.

1.1.2 ΛCDM, its successes and failures

In the late 1990s, it became evident from measurements of Type 1a supernovae that our universe is expanding, and not only that, but the expansion is actually accelerating (Riess et al., 1998; Perlmutter et al., 1999). The driving force behind this expansion remains unclear, and the energy associated with it has been labelled "dark energy". Dark energy is represented by the cosmological constant, denoted as Λ, and is a crucial component of the Lambda cold dark matter (ΛCDM) model of the universe.

Today, the ΛCDM model is widely used in astronomy as the prevailing framework for understanding the universe. According to this model, the universe consists of 68% dark energy, 27% dark matter, and 5% ordinary matter in terms of matter distribution. During the early stages of the universe, small overdensities in the dark matter distribution led to the formation of gravitationally bound clumps called dark matter halos. Through a series of mergers, these dark matter halos grew hierarchically. An illustration depicting the evolution of the universe is presented in Fig. 1.1.

Although the ΛCDM model has achieved significant success, it also faces several "problems" on smaller scales. Here, I will provide a brief overview of these small-scale issues, and for a more comprehensive review refer to Bullock & Boylan-Kolchin (2017).

(i) One prominent problem is known as the missing satellites problem, which became apparent through large dark matter-only simulations. These simulations predicted a greater abundance of dwarf galaxies and substructures in the Local Group than what we actually observe (Klypin et al., 1999; Moore et al., 1999). According to dark matter-only simulations, the Milky Way should be surrounded by approximately 10,000 dwarf galaxies with dark matter masses above around 10^5 $M_\odot$ (Springel et al., 2008). However, we have only detected around 50 galaxies (Adelman-McCarthy et al., 2007; Bechtol et al., 2015; Drlica-Wagner et al., 2015; Koposov et al., 2015). Some of these dwarf galaxies may be too faint to observe within the limits of current surveys, but this cannot account for all the missing satellites (Koposov & Belokurov, 2008; Tollerud et al., 2008; Hargis et al., 2014; Kim et al., 2018; Newton et al., 2018). Recent studies have suggested that feedback and re-ionisation could prevent smaller halos from forming stars, providing a potential explanation for the observed population of Milky Way satellites in hydrodynamical simulations (Benitez-Llambay & Frenk, 2020; Sawala et al., 2015; Bose et al., 2018).

(ii) The too big to fail problem is closely related to the missing satellites problem, as highlighted by Boylan-Kolchin et al. (2011b, 2012). These studies focused on the discrepancy between the observed massive halos around the Milky Way (MW) and the predictions from the ΛCDM simulations. The known satellites of the MW are not as massive as what the simulations suggest. While the simulations did produce halos of similar size, they did not include them among the ten most massive satellites. The too big to fail problem questions why the most massive dark matter halos fail to form stars when smaller halos do. This is not only a problem for MW satellites, it has also been seen for satellites of Andromeda, the Local Group and even isolated dwarf galaxies (Ferrero et al., 2012; Kirby et al., 2014).

(iii) The plane of satellites problem refers to the arrangement of satellite galaxies around the MW. The observed MW satellites appear to align in a plane perpendicular to the galactic disc (Lynden-Bell, 1976; Kunkel & Demers, 1976). This configuration of

satellites is not only challenging for the ΛCDM model but also for the hierarchical growth of galaxies, as both would predict a more isotropic distribution of satellites. While simulations have shown the existence of planes of satellites, this phenomenon is quite rare, occurring in only around 1% of disc galaxies (Shao et al., 2019). The work of Cautun et al. (2015) carefully examines the statistical aspects of a planar distribution of satellites, which helps alleviate the tension with the ΛCDM model.

(iv) The core-cusp problem arises from the inconsistency between dark matter-only simulations and observations. According to dark matter-only simulations, the density distribution of a dwarf galaxy should exhibit a central cusp. However, observations of nearby dwarf galaxies using HI rotation curves suggest that the central regions have a core in the dark matter density profile (Moore, 1994; Read et al., 2016; Genina et al., 2018). Interestingly, when baryonic feedback processes are taken into account in the simulations, it is possible to generate cores in the density profile, as demonstrated in the study by Benítez-Llambay et al. (2019).

1.1.3 Alternative dark matter models

The small-scale problems with ΛCDM have motivated alternative dark matter models, such as warm dark matter and self-interacting dark matter. In warm dark matter (WDM) models of the universe, the dark matter particles are warmer than their CDM counterparts. In the WDM model, there is a cut-off in the power spectrum, and halos that are less massive than a characteristic mass (caused by the cut-off in the power spectrum) cannot form (Avila-Reese et al., 2001; Schneider et al., 2012; Lovell et al., 2012).

The most commonly used candidates for WDM are thermal relic WDM particles and sterile neutrinos. A thermal relic WDM model consists of dark matter particles that were produced in thermodynamic equilibrium with photons and other relativistic particles in the early universe (e.g, Bertone et al., 2005). After the universe started cooling, these dark matter particles would decouple from the surrounding plasma, it's density would be frozen in time and it would start to free stream. The sterile neutrino model would have particles

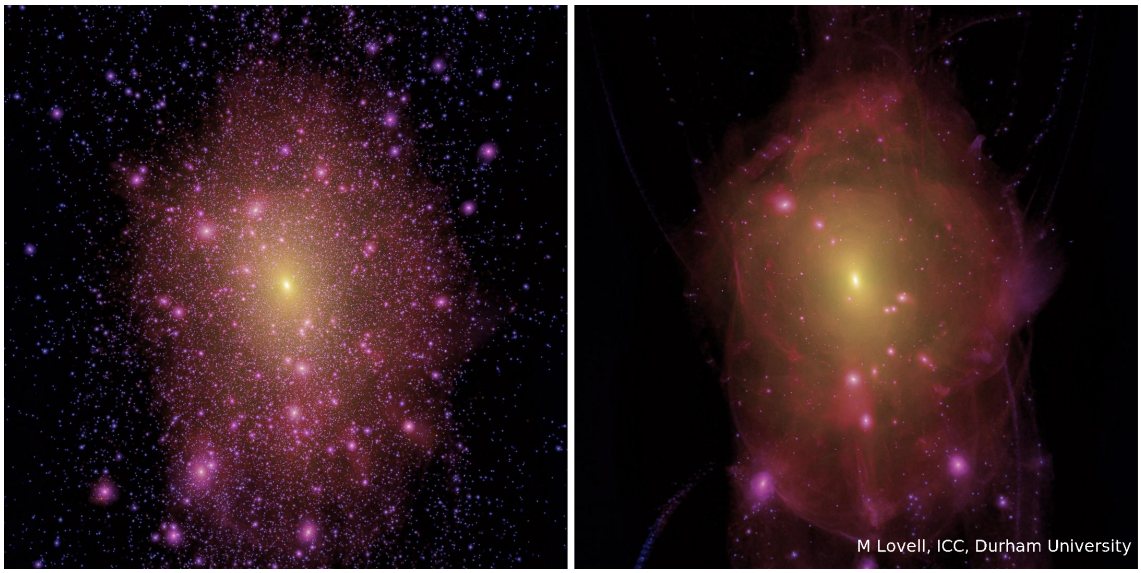

Figure 1.2
Comparison of cold and warm dark matter models. Image credit: Mark Lovell.

similar to the Standard Model neutrinos but without interactions. Sterile neutrinos are also CDM candidates. For more information about other candidates for dark matter particles see Section 3 in Bertone et al. (2005) and Bertone & Hooper (2018).

The mass of the WDM candidate is responsible for the cut-off in the matter power spectrum when compared with CDM. Thermal relic WDM particles affect the cut-off in the power spectrum in a simple monotonic way. However, non-thermal candidates such as the sterile neutrino include other parameters which affect the cut-off in the power spectrum such as e.g., lepton asymmetry (see e.g., Boyarsky et al., 2009a).

WDM particles which are not "too warm" are consistent with the observed matter power spectrum (Boyarsky et al., 2009b) provided they have masses greater than ~ 1 keV. More recently, the mass of WDM particles has been estimated far colder than previously thought, with current lower limits for a thermal relic WDM particle of $m > 5.3$ keV in Iršič et al. (2017) from the Lyman-α measurements and $m > 4.4$ keV from measurements of Milky Way satellite observations in Dekker et al. (2022).

As previously mentioned, the WDM model, there is a cut-off in the power spectrum. If the smallest halos cannot form, then WDM would, in part, solve the missing satellites problem as shown in Fig. 1.2. However, the lack of smaller halos has consequences for the growth of the more massive halos, causing them to have later formation times. Later

formation times of the more massive halos would also solve the too big to fail problem due to their smaller $V_{\rm max}$ values (Anderhalden et al., 2013; Lovell et al., 2016; Newton et al., 2019). Not only does the lack of smaller halos cause later formation times, it also affects the mergers a halo experiences. Recent work by Deason et al. (2022) showed that there are more mergers occurring per halo in CDM than in WDM for halos in the relevant mass range for dwarf galaxies. If a halo has less mergers across its lifetime, this could have a significant impact on it's properties and growth. See Chapter 4 for an in depth discussion of mergers in CDM vs WDM. A WDM universe does not solve the core-cusp problem as halos do not form large cores (Shao et al., 2013).

Another proposed model is self-interacting dark matter (SIDM; Spergel & Steinhardt, 2000), where dark matter can interact with itself instead of being a collisionless fluid. In SIDM, dark matter cores can be produced when there is a large enough cross-section, and dark matter is able to scatter in the central region of the halo. The presence of a dark matter core lowers the central density (when compared with CDM), which solves the too big to fail problem (Vogelsberger et al., 2012; Elbert et al., 2015). The missing satellites problem is not solved in SIDM since the power spectrum resembles that of CDM (Rocha et al., 2013).

1.2 Dwarf galaxies

Dwarf galaxies hold significant importance in many fields of astronomy. Their small size and low mass make them highly susceptible to various astrophysical phenomena. As previously mentioned, these galaxies could play a crucial role in constraining the nature of dark matter. Not only are dwarf galaxies in an optimal regime for studying dark matter, they are also highly suited to studies of reionisation and the early universe, as well as galaxy formation and evolution. Here, I will provide a brief overview of how dwarf galaxies could help advance the studies of these fields:

(i) Due to their low mass, dwarf galaxies would have been the most affected by reionisation. Early in the history of the universe, ultraviolet radiation from the first

stars reionises the hydrogen (Doroshkevich et al., 1967; Couchman & Rees, 1986), preventing the gas from cooling and halting star formation in low mass galaxies (Rees, 1986; Efstathiou, 1992; Loeb & Barkana, 2001). Therefore, studying the abundances of dwarf galaxies can reveal hidden details about the epoch of reionisation and the early universe (e.g., Bose et al., 2018).

(ii) Galaxy formation at low mass scales is currently an open question in astronomy. For example, the stellar mass-halo mass relation is very uncertain on dwarf galaxy scales, and several studies have suggested that the scatter is much larger than for higher mass halos, possibly increasing as halo mass decreases (e.g., Garrison-Kimmel et al., 2017; Munshi et al., 2021). Therefore, we do not yet know the minimum mass a halo needs to be in order to form stars.

(iii) Dwarf galaxies drive the evolution of bigger galaxies through merging onto them (as predicted by ΛCDM, for more details about mergers see Section 1.4.2 and Chapter 4). In the Milky Way we are in the privileged position to study not only surviving dwarf galaxies but also destroyed ones in the Galactic stellar halo.

Therefore, it is clear that studying dwarf galaxies could unlock many mysteries of the universe.

1.3 Simulations

1.3.1 Hydrodynamical cosmological simulations

Since the 1970s and 1980s, simulations have grown in popularity for studying the universe around us. The earliest simulations by Press & Schechter (1974) and Davis et al. (1985) were dark matter, gravity-only simulations. In 1992, Katz (1992) made the first hydrodynamical simulations. Hydrodynamical cosmological simulations track the evolution of dark matter, stars, and gas. The dark matter particles evolve purely according to gravitational forces, whereas baryonic matter can be implemented in two ways: smoothed

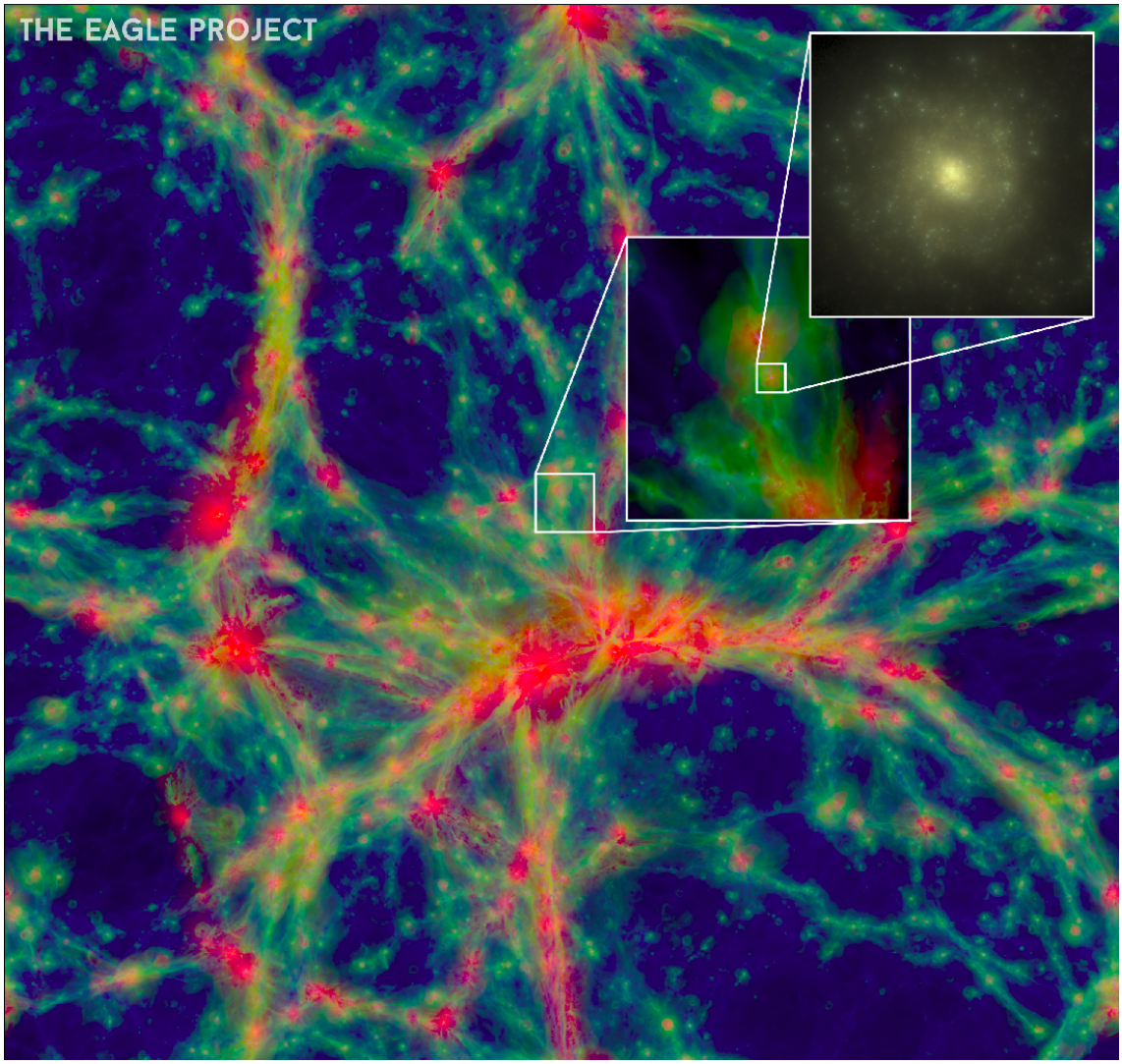

Figure 1.3
The EAGLE simulation box. The colour indicates the density of particles, where red is the most dense. Image credit: the EAGLE team.

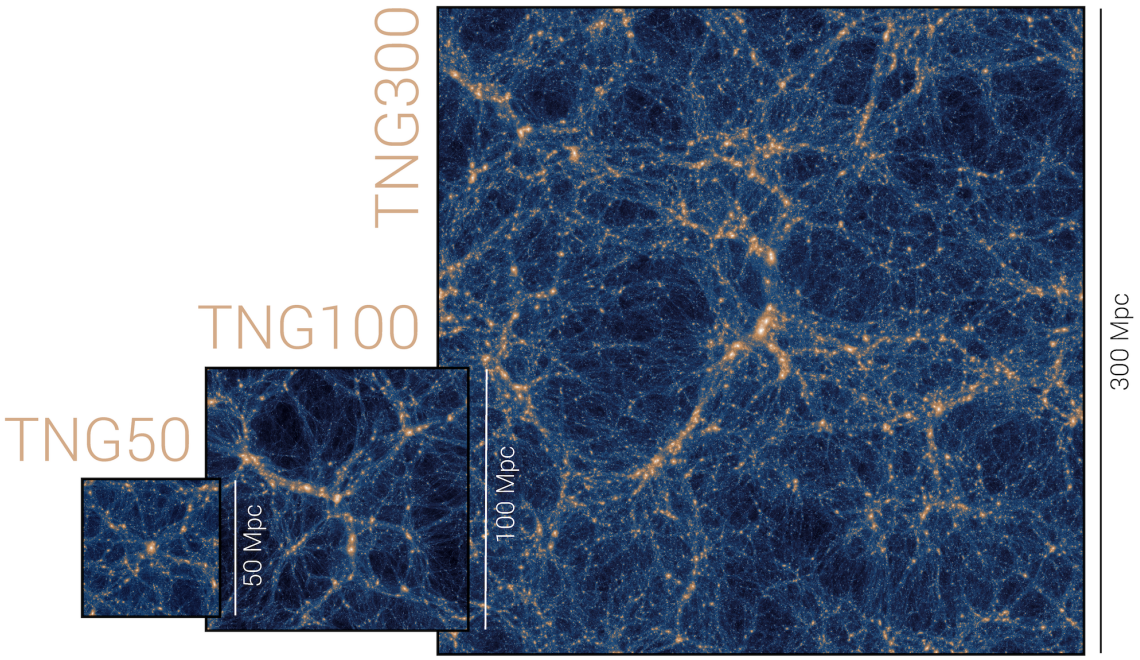

Figure 1.4
The IllustrisTNG simulations. A comparison between TNG50, TNG100 and TNG300 (roughly to scale). Each panel shows the projected dark matter density. Image credit: the IllustrisTNG team.

particle hydrodynamics (SPH) or adaptive mesh cells. The most recent examples of these approaches are the EAGLE simulations (Fig. 1.3; Schaye et al., 2015; Crain et al., 2015) which is run using the Gadget3 code (Springel, 2005), and the IllustrisTNG simulations (Fig. 1.4; Marinacci et al., 2018; Naiman et al., 2018; Nelson et al., 2018; Pillepich et al., 2018; Springel et al., 2018) which uses the AREPO moving mesh code (Springel, 2010). Both of these simulation suites reproduce properties of the observed universe.

Modern hydrodynamical simulations include the following processes: gas cooling and heating, stellar winds, chemical evolution, and AGN feedback. The simulations are typically calibrated to match observations at redshift $z = 0$. However, several regimes in these simulations are not very well constrained. Future simulations, such as the upcoming COLIBRE simulations, will improve the subgrid physics, especially on smaller scales (e.g., molecular gas in the interstellar medium, which was not previously resolved).

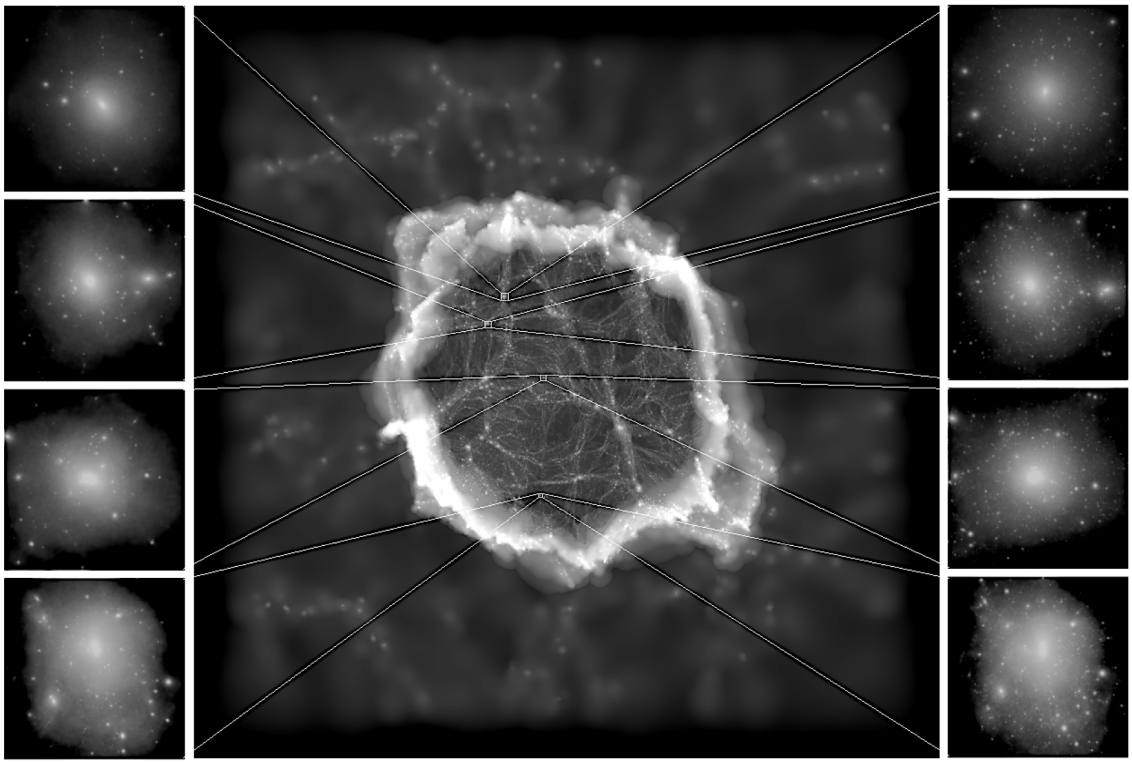

Figure 1.5
Density map of the COCO simulation centred on the high resolution region at $z = 0$. The side panels show individual halos matched in COCO-COLD (right) and COCO-WARM (left) at redshift $z = 0$ by Bose et al. (2016).

1.3.2 Zoom-in simulations

Zoom-in simulations typically have a much smaller volume than cosmological simulations and are focused on either a small volume or one individual galaxy (Katz & White, 1993; Tormen et al., 1997; Frenk et al., 1999; Bertschinger, 2001; Gao et al., 2005; Hahn & Abel, 2011; Jenkins, 2013). Often, individual galaxies or regions of large cosmological volumes are used to initiate the "zoom-in" simulation, as demonstrated in Fattahi et al. (2016). The particles within the interested regions are tracked back to their initial perturbations in their "Lagrangian region" to establish the necessary particles for re-simulation. Since zoom-in simulations have a much smaller volume, their resolution is generally far greater than that of cosmological simulations, allowing them to reveal more detailed properties about the galaxies within.

The Copernicus Complexio (COCO) simulation is a dark matter only zoom-in simulation (Bose et al., 2016; Hellwing et al., 2016). The initial conditions for COCO were selected

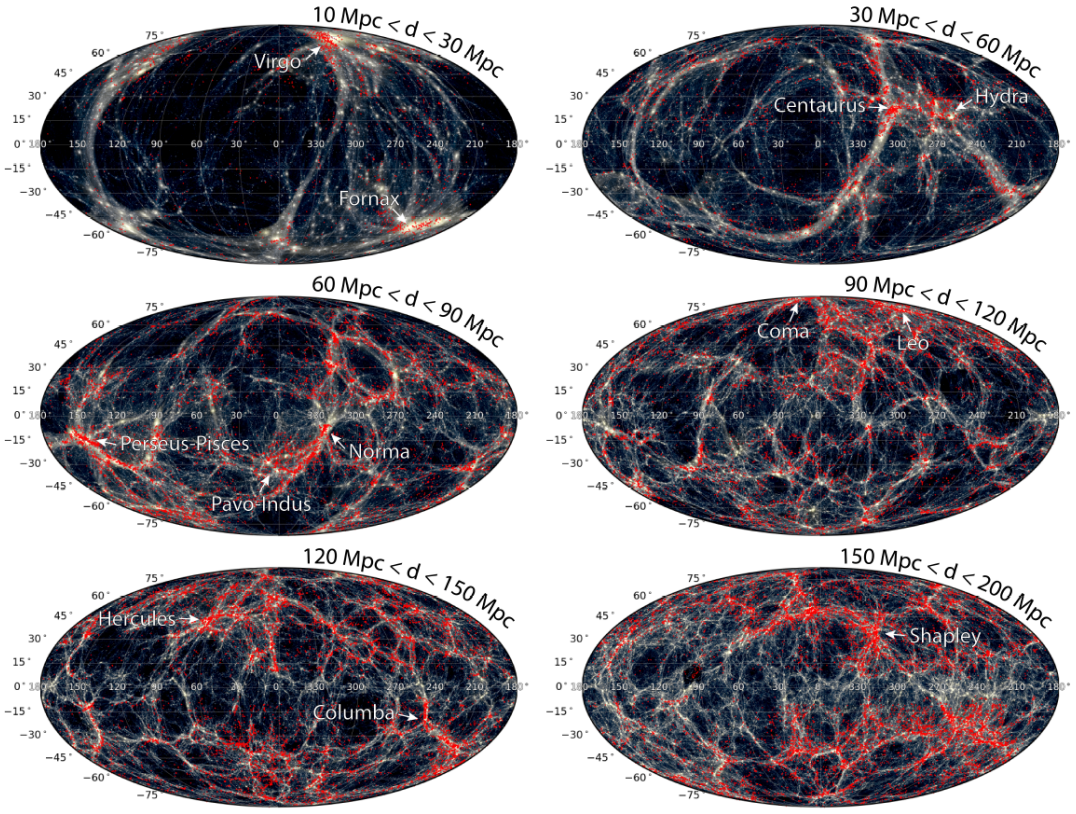

Figure 1.6
The SIBELIUS simulations. An all-sky map of the simulation with observational data from the 2MASS survey as red points to show how well the simulations reproduce the local universe. Image from McAlpine et al. (2022).

from its parent simulation, Copernicus Complexio Low Resolution (COLOR). Fig. 1.5 clearly shows the high-resolution region in the centre, which is surrounded by a lower-resolution region. Unlike large box simulations, zoom-in simulations do not have periodic boundary conditions around the high resolution region, so it is important to consider the particle regions when analysing these simulations.

Another type of zoom-in simulation is created using a constrained realisation technique. Constrained realisation simulations aim to reproduce the local observed volume. This technique can be done using two different methods. The first method was pioneered by Bertschinger (1987) and Hoffman & Ribak (1991), where they inferred the initial conditions for the simulation from a data set of galaxy redshifts or radial peculiar velocities. Many simulations have been made using these constrained realisation methods, such as those by Mathis et al. (2002), the "Constrained Local UniversE Simulations" (CLUES) project

(Yepes et al., 2014; Carlesi et al., 2016), the "Constrained LOcal & Nesting Environment Simulations" (CLONES) project (Sorce et al., 2021), the "ELUCID simulation" (Wang et al., 2016), and the "High-resolution Environmental Simulations of The Immediate Area" (HESTIA) project (Libeskind et al., 2020).

The second method for creating the initial conditions of a constrained realisation simulation uses a Bayesian inference model with a Hamiltonian Monte Carlo sampling approach, as described in Wang et al. (2014) and Jasche & Wandelt (2013).

The most recent example of a constrained realisation simulation is the Simulations beyond the local universe (SIBELIUS) project (as described in Sawala et al., 2022). The SIBELIUS project not only includes the larger cosmic structure but also a local group analogue at the centre. The initial presentation of this project was a dark matter only simulation, as shown in McAlpine et al. (2022). In Figure 1.6, the Sibelius Dark simulation is depicted, demonstrating its ability to reproduce the local universe. The density map in the background represents the simulation, while the red points correspond to observational data from the 2MASS survey.

1.3.3 Simulations relevant for this thesis

1.3.3.1 EAGLE

The EAGLE project is a suite of cosmological hydrodynamical simulations that follow the formation and evolution of galaxies, tracking the gas, stars and dark matter throughout cosmic history. The simulations use a modified version of the Tree-PM SPH code P-GADGET3 (developed first for the Aquarius Project Springel et al., 2008). The hydrodynamics solver uses a pressure-entropy formalism (see Schaller et al., 2015b, for details). The subgrid galaxy formation model includes homogeneous photoionising background radiation, metallicity-dependent star formation and cooling, stellar evolution and supernovae feedback, seeding and growth of supermassive black holes, and AGN feedback (see Schaye et al., 2015, for a full description of the model). The galaxy formation model was calibrated to reproduce the stellar mass function of galaxies at $z = 0.1$ and realistic galaxy sizes,

down to a stellar mass of $\sim 10^8\,\mathrm{M}_\odot$. The model has been shown to produce galaxies with realistic mass profiles and rotation curves (Schaller et al., 2015a). The stellar mass-halo mass relation shows that EAGLE has too low stellar mass compared with observations, the recalibration used for the ARTEMIS simulations (Font et al., 2020) improves this relation.

The fiducial EAGLE run has a periodic cubic volume of $(100\mathrm{Mpc})^3$ and was run with the 'REFERENCE' parameters (REF-L0100N1504 in the nomenclature of Schaye et al., 2015). The initial mass for gas and matter particles are 9.6×10^6 $\mathrm{M}_\odot$ and 1.81×10^6 $\mathrm{M}_\odot$, respectively. The Friends-of-Friends (FoF) algorithm was used to identify dark matter halos (Davis et al., 1985), and the SUBFIND algorithm was used to identify self-bound structures and substructures associated with each FoF group (Springel, 2005). The cosmological parameters adopted for the simulations are based on Planck Collaboration et al. (2014): $\Omega_m = 0.307$, $\Omega_\lambda = 0.693$, $\Omega_{bar} = 0.04825$, $H_0 = 67.77\,\mathrm{km\,s^{-1}Mpc^{-1}}$, $\sigma_8 = 0.8288$.

The large volume of the main EAGLE simulation provides a large number of MW-mass galaxies which have a variety of merger histories. The stellar mass, M_*, for each galaxy was calculated by summing the mass of the star particles bound to each galaxy within 30 kpc of the galaxy's centre. The halo mass and radius, M_{200} and R_{200} respectively, are defined as those of the sphere with average enclosed density equal to 200 times the critical density of the universe (ρ_{crit}). We define satellites as those subhalos within R_{200} of their host.

Several element abundances, including iron and hydrogen are tracked self-consistently in the simulations for gas and star particles. We convert those mass fractions to [Fe/H] assuming a solar abundance of $12 + \log_{10}(N_{Fe}/N_H) = 7.5$ from Asplund et al. (2009) to assign magnitudes to each star particle (described in more detail in Section 3.3).

1.3.3.2 IllustrisTNG

Chapter 3 includes several comparisons between the EAGLE simulation and the IllustrisTNG simulations suite. The following section will describe the simulations and highlight any key differences between EAGLE and IllustrisTNG.

Table 1.1
Parameters for IllustrisTNG simulation suite: number of gas cells (N_{gas}), number of dark matter particles (N_{dm}), baryon mass resolution (m_b) and dark matter mass resolution (m_{dm}).

IllustrisTNG simulation	N_{gas}	N_{dm}	m_b ($h^{-1}\,M_\odot$)	m_{dm} ($h^{-1}\,M_\odot$)
TNG50	2160^3	2160^3	5.7×10^4	3.1×10^5
TNG100	1820^3	1820^3	9.4×10^5	5.1×10^6
TNG300	2500^3	2500^3	7.4×10^6	4.0×10^7

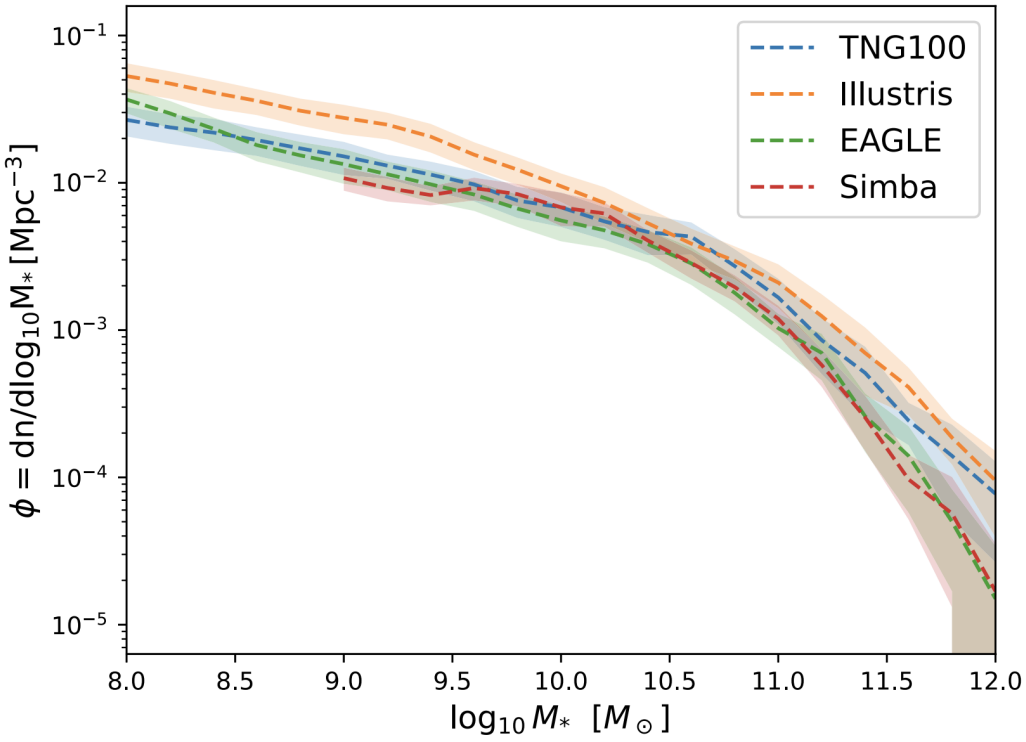

Figure 1.7
The stellar mass functions of EAGLE (green) and TNG100 (blue). Image credit: McGibbon & Khochfar (2023)

The IllustrisTNG suite of simulations (Marinacci et al., 2018; Naiman et al., 2018; Nelson et al., 2018; Pillepich et al., 2018; Nelson et al., 2019; Pillepich et al., 2019) is comprised of TNG50, TNG100 and TNG300 which have periodic volumes of $\sim 50^3$, 100^3, and 300^3 Mpc^3 respectively. The cosmological parameters used in IllustrisTNG are the following: $\Omega_m = 0.3089$, $\Omega_\lambda = 0.6911$, $\Omega_{bar} = 0.0486$, $H_0 = 67.74\,\mathrm{km\,s^{-1}Mpc^{-1}}$, $\sigma_8 = 0.8159$ from Planck Collaboration et al. (2016). A summary of the parameters are presented in Table 1.1. IllustrisTNG was run using the moving-mesh code AREPO (as mentioned in the previous section) with the IllustrisTNG galaxy formation model which has been shown to have stellar mass and r-band sizes consistent with observations for galaxies in the range $\mathrm{M}_* > 10^9\,\mathrm{M}_\odot$ and $z \leq 2$.

A comparison of the EAGLE and IllustrisTNG 100 stellar mass functions are shown in Fig. 1.7 in green and blue respectively. The stellar mass function of TNG100 is slightly higher for all masses above $\mathrm{M}_* > 10^{8.5}\,\mathrm{M}_\odot$. The differences between the stellar mass functions are much greater for the higher mass galaxies (with mass greater than $\mathrm{M}_* > 10^{11}\,\mathrm{M}_\odot$), therefore, there are more high mass galaxies present in TNG100 than there are in EAGLE.

1.4 The Milky Way

The Milky Way (MW) galaxy, our home in the universe, is a spiral galaxy that contains billions of stars. It is estimated to contain 100-400 billion stars and is home to our solar system. The MW has often been seen as the benchmark for spiral galaxies. The MW has a dark matter halo mass of $M_{200}^{MW} = 1.17^{+0.21}_{-0.15} \times 10^{12} M_\odot$ (see Callingham et al., 2019, and references therin). The MW is not only a massive galaxy but also a sizeable one, the galactic disc has a diameter of roughly 25-30 kpc (Bland-Hawthorn & Gerhard, 2016) and a dark matter halo diameter of roughly 290 kpc (Deason et al., 2020). The MW lives in the local group which is part of the Virgo supercluster of galaxies.

A brief account of the stellar component of the MW is outlined below. For a more detailed review of the MW, refer to Bland-Hawthorn & Gerhard (2016).

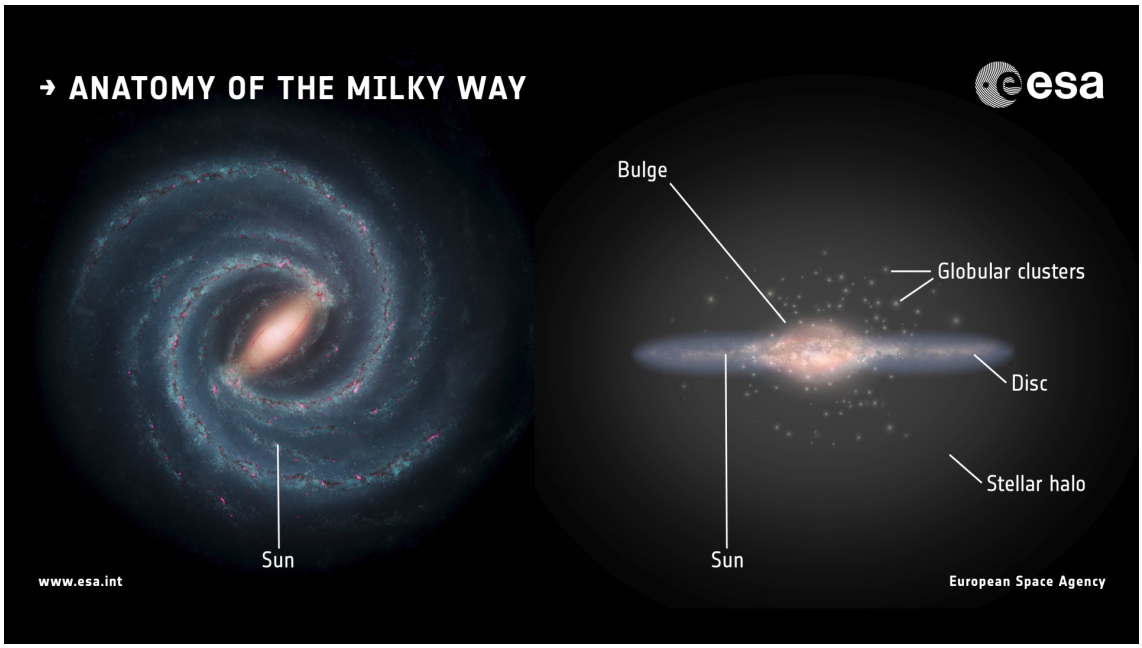

Figure 1.8
An illustration showing the anatomy of the Milky Way, including the position of the sun, bulge, disc, stellar halo and globular clusters. Image credit: ESA.

- The thin disc is the region of the galaxy that is actively forming stars. The star formation rate of the thin disc is estimated to be 1.6 $M_\odot$ year^{-1} (Licquia & Newman, 2015), and it appears to have been forming stars for approximately 8-9 Gyr (Tononi et al., 2019). The thin disc is home to the Sun at roughly 8 kpc. The stars in the thin disc move on approximately circular orbits.

- The thick disc is more diffuse than the thin disc. The stars in the thick disc are older and have a lower metallicity. The thick disc was formed at roughly the same time as the merger between the MW and GES (Belokurov et al., 2018).

- Our understanding of the MW's bar/bulge is limited since it is heavily obscured. The bulge of the MW is a boxy/peanut bulge. Most of the bulge stars are in the bar.

- The stellar halo is the most extended region of the Galaxy and typically contains the oldest and most metal-poor stars. The density profile of the Galactic stellar halo is described by a broken power law (Deason et al., 2011) and has a mass of roughly $1.3 \times 10^9\,M_\odot$ (Deason et al., 2019; Mackereth & Bovy, 2020).

Studying the MW is essential for our understanding of galaxy formation and evolution

because it is the only galaxy we can study these processes on a star-by-star basis. It is also necessary to understand how well the MW represents the galaxy population as a whole, so that we can relate what we learn about our Galaxy to all the other galaxies in the universe. A prominent theme of this thesis is the atypical features of the MW and how they could affect observing high redshift progenitors of MW analogue galaxies.

1.4.1 Observing the Milky Way

Our understanding of the MW has been revolutionised by the Gaia mission. The Gaia mission is a European Space Agency (ESA) satellite that was launched on 19 December 2013. Gaia's goal was to accurately measure the position and fluxes of the whole sky, including approximately 1 billion stars (Gaia Collaboration et al., 2018).

The sky as seen by Gaia's third data release is shown in Fig. 1.9. The disc of the MW is very prominent, and one can also see the halo stars extending out to roughly 100 kpc. Not only is Gaia taking astrometry measurements of stars, but it is also capturing spectra of the entire sky. Since Gaia observes the entire sky while orbiting, it provides accurate measurements of the velocities at which stars are moving or orbiting within the MW. Future releases of Gaia data are expected to further reduce uncertainties in proper motion velocities.

Complementary spectroscopic surveys to Gaia include: the Sloan Extension for Galactic Understanding and Exploration (SEGUE; Yanny et al., 2009), the APO Galactic Evolution Experiment (APOGEE ; Majewski et al., 2017), the GALactic Archaeology with HERMES (GALAH; Martell et al., 2017), Gaia-ESO (Gilmore et al., 2012), the RAdial Velocity Experiment (RAVE; Steinmetz et al., 2020) and the Large Sky Area Multi-Object Fibre Spectroscopic Telescope (LAMOST; Zhao et al., 2012). These can provide radial velocities and (sometimes) chemical abundances of MW stars, which, in combination with Gaia astrometry, allows for detailed chemodynamical (6D phase-space plus chemistry) studies of the Galaxy.

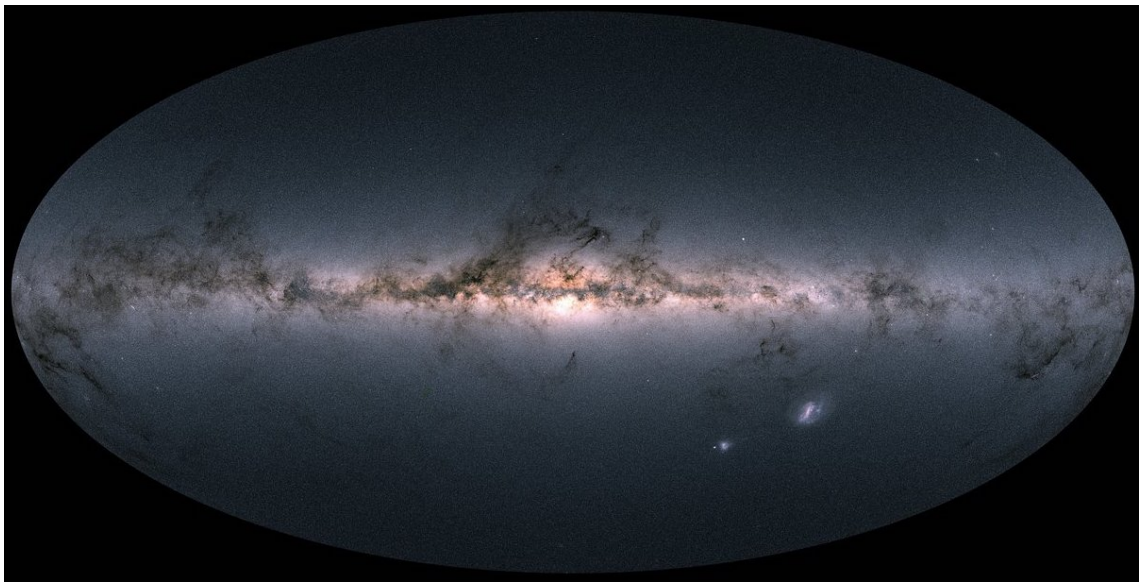

Figure 1.9
Edge on view of the Milky Way as seen by Gaia. Image credit: ESA/Gaia.

1.4.2 Assembly history and Galactic archaeology

The method for studying the assembly history of the MW is often referred to as galactic archaeology. In the 1950s, Roman (1950) showed that stars with different chemical abundances have different kinematics. In the 1960s, Eggen et al. (1962) made further connections between the chemistry and kinematics of stellar populations within the MW stellar halo. In their influential work, Searle & Zinn (1978) proposed that the Milky Way was assembled through the gradual merging of many smaller galaxies.

Low-mass stars form very early in the universe and have survived until the present day. Their chemistry reflects the environment in which they were born. Hence, stars with similar chemical abundances likely have a common source. If stars were born in another galaxy, then they are likely to all have a similar chemical signature, different from the stars that formed within our Galaxy.

According to predictions from the ΛCDM model of the universe, halos form and evolve through a sequence of hierarchical mergers (White & Rees, 1978; Davis et al., 1985). When a dwarf galaxy merges with the MW, stars from the merging galaxy get stripped by tidal forces, and they continue along similar trajectories as their host galaxy would have (Johnston et al., 1996; Johnston, 1998). This implies that if there were several smaller

mergers or accreted satellites, there would be several different "streams" of stars with several different orientations. If there was, however, just one massive merger, this would create an orbit of one large population of stars all following a similar path corresponding to that of its progenitor galaxy. Hence, by analysing the stars' chemistry (in these cases, their metallicity) and their velocities, different populations of stars could be identified.

Recently, with the 6D phase-space information of stars in the MW provided by the second data release of the Gaia mission, an ancient massive merger remnant was found by Helmi et al. (2018) and Belokurov et al. (2018). In this thesis, the merger will be referred to as the Gaia-Enceladus Sausage (GES). More details about the GES are included in Section 1.4.3.

The combination of astrometric data from the Gaia satellite and spectroscopy from large-scale high-resolution spectroscopic surveys has led to the discoveries of several dwarf mergers with the MW by various groups in the past few years, including the Sequoia (Barbá et al., 2019; Matsuno et al., 2019; Myeong et al., 2019), Thamnos (Koppelman et al., 2019), Nyx (Necib et al., 2020), LMS-1 (Yuan et al., 2020), Arjuna/Aleph/I'itoi (Naidu et al., 2020), and Cetus (Newberg et al., 2009), Heracles (Horta et al., 2021), and Pontus (Malhan et al., 2022). Other key mergers with the MW include the Sagittarius dwarf galaxy, which started its merger with the MW around 8 Gyr ago and is still ongoing. The estimated mass of the Sagittarius dwarf is roughly $5 \times 10^8\,M_\odot$, approximately 1-5% of the mass of the MW (see e.g., Dierickx & Loeb, 2017; Fardal et al., 2019, and references therein). The MW is also currently in the early stages of merging with its most massive satellite galaxy, the Large Magellanic Cloud (LMC). More details about the LMC are included in Section 1.4.4.

1.4.3 Gaia-Enceladus Sausage

The Gaia-Enceladus Sausage (GES) is the remains of a dwarf galaxy that merged with the MW about 8-11 Gyr ago. It represents the last major merger of the MW. The discovery of GES revolutionised our understanding of the inner Galactic halo.

GES was discovered independently by two teams, Helmi et al. (2018) and Belokurov et al.

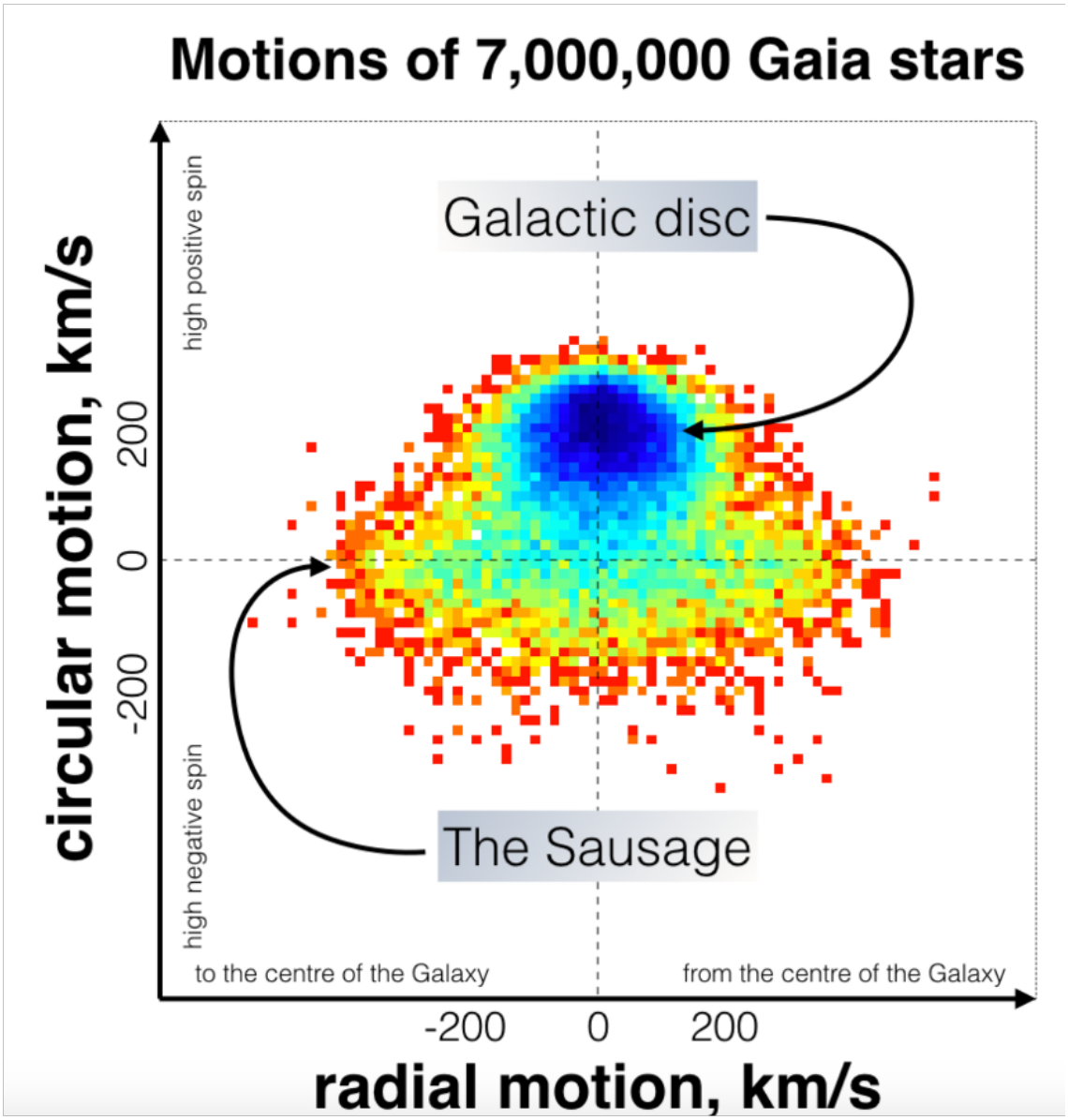

Figure 1.10
The distribution of stellar velocities in the Milky Way. The stars associated with 'The Sausage' are indicated in the image. Image credit: Belokurov et al. (2018).

(2018). Helmi et al. (2018) analysed the kinematics, chemistry, and positions of stars in the MW's thick disc and stellar halo and found that high-energy stars on retrograde orbits are also linked by their chemical compositions. They concluded that the inner halo is dominated by stars coming from a single object accreted around 8-11 Gyr ago. Belokurov et al. (2018) used kinematics and chemistry of stars from SDSS and Gaia DR1 to show that, at higher metallicity ([Fe/H] > -1.7), the orbits of the halo stars are very radially biased (with velocity anisotropy, $\beta \sim 0.9$, where $\beta = 1 - [(\sigma_\theta^2 + \sigma_\phi^2)/2\sigma_r^2]$). These authors argue that the extreme radial orbits in the inner stellar halo cannot have been caused by steady accretion of low-mass dwarf galaxies but instead must have come from a single merger event with a massive satellite some 8-11 Gyr ago.

GES is estimated to have contributed approximately two-thirds of highly eccentric stars in the stellar halo (e.g., Mackereth & Bovy, 2020). The GES stars exhibit a distinct sausage-like distribution in the radial-azimuthal velocity distribution, as observed in previous studies (Brook et al., 2003; Belokurov et al., 2018). The GES stars are characterised by their lower metallicity and reduced α-enhancement compared to the redder halo counterpart (Haywood et al., 2018; Helmi et al., 2018). These chemical properties suggest that protogalactic disc stars were dynamically expelled into the halo during the GES merger. This phenomenon, referred to as the Splash by Belokurov et al. (2020) and Bonaca et al. (2020), has been previously identified by earlier investigations (Bonaca et al., 2017; Haywood et al., 2018; Di Matteo et al., 2019; Gallart et al., 2019).

A connection was also made between the MW's stellar halo density profile and the GES merger by Deason et al. (2018). They found that the stars likely belonging to GES (metal-rich, highly eccentric halo stars) have a common apocenter at 20 kpc, roughly the value of the stellar halo breaking radius. Hence, it is likely that the break in the stellar halo density profile is due to the apocentric pile-up of the massive accretion event of the GES dwarf.

1.4.4 Large Magellanic Cloud

The Large Magellanic Cloud (LMC) is a satellite of the MW, roughly 50 ± 1 kpc away (e.g., Walker, 2012; Pietrzyński et al., 2013). The mass of the LMC is not fully constrained; many different techniques have been used, including using the LMC dynamics and modelling its rotation curve (e.g., Schommer et al., 1992; van der Marel & Kallivayalil, 2014). These techniques estimate the halo mass of the LMC to be roughly $2 \times 10^{10}\,M_{\odot}$. More recently, wide-field surveys have revealed a lot of debris around the outskirts of the LMC (e.g., Mackey et al., 2016; Besla et al., 2016; Belokurov & Koposov, 2016; Deason et al., 2017; Belokurov et al., 2017; Mackey et al., 2018; Navarrete et al., 2019; Nidever et al., 2019), which suggests that the previous measurements were significantly underestimating its mass. New estimates suggest the halo mass of the LMC is likely in the range $1 - 3 \times 10^{11}\,M_{\odot}$ (e.g., Peñarrubia et al., 2016; Erkal et al., 2019; Erkal & Belokurov, 2020; Vasiliev et al., 2021; Shipp et al., 2021; Correa Magnus & Vasiliev, 2022; Koposov et al., 2023). The stellar mass component of the LMC is estimated as $3 \times 10^{9}\,M_{\odot}$ (van der Marel et al., 2002; Stanimirović et al., 2004; Harris, 2007).

The presence of the LMC is very unusual since it has been shown in simulations that only 10% of MW-sized galaxies have such a massive nearby satellite (e.g., Boylan-Kolchin et al., 2011b; Busha et al., 2011; Liu et al., 2011; Tollerud et al., 2011). It's suspected that once the MW completes its merger with the LMC, some of the unusual properties of the MW (small black hole) will return the MW to a more normal state (Cautun et al., 2019).

1.5 Thesis Goals and Outline

This thesis aims to further our understanding of the MW and small-scale cosmology through studying mergers with the use of simulations. The following work is comprised of three science chapters.

Chapter 2: How unusual is the Milky Way's assembly history?

This chapter finds the Milky Way-like galaxies in EAGLE that have an assembly history most similar to that of our own Galaxy (with an LMC-like satellite and GES-like accretion). The properties of these galaxies are compared to those of an "average" Milky Way galaxy (defined only by its mass).

Chapter 3: Observing EAGLE galaxies with JWST: predictions for Milky Way progenitors and their building blocks

This chapter models the apparent magnitudes and dust for the EAGLE galaxies to make predictions for the upcoming JWST observations. The luminosity functions for all EAGLE galaxies were made at redshifts $z = 2, 4, 6, 8$ for the JWST/NIRCam passbands. The focus was to determine how far back in time we could observe progenitors of MW-like galaxies and their building blocks, i.e., their LMC-like satellites and their GES-like accretions. The goal was also to determine if progenitors of all three galaxies would be within one JWST/NIRCam Field-of-View at early times.

Chapter 4: Effect of environment on merger rates: cold vs warm dark matter

This chapter studies the mergers of low mass halos as a function of local scale and large-scale environment in the COCO dark matter-only simulations. The total number of mergers and timing of the mergers are compared between environments and dark matter models to determine the region best suited for targeted observations of dwarf galaxies with upcoming surveys.

Chapter 5: Conclusions

This chapter summarises the work of the thesis and outlines areas of future work.

CHAPTER 2

How Unusual is the Milky Way's Assembly History?

2.1 Introduction

The Milky Way (MW) is sometimes regarded as a template for studies of the structure and evolution of $L^\star$ spiral galaxies. Yet, the more we find out about the MW, the more we recognise that it is anything but typical; in fact, several of its properties are distinctly atypical. For example, the MW hosts a very massive satellite, the Large Magellanic Cloud (LMC), which has approximately 10% of the total MW halo mass (e.g. Peñarrubia et al., 2016; Erkal et al., 2019) . Studies using large samples of observed local galaxies, combined with cosmological simulations, find that only $\sim$ 10% of MW-mass galaxies host a satellite as massive as this (e.g. Liu et al., 2011; Busha et al., 2011; Boylan-Kolchin et al., 2011b; Tollerud et al., 2011). Not only is the presence of a massive satellite rare, but the scale of the damage the LMC is inflicting on the Galaxy has recently began to be recognised. This includes perturbing the barycentre of the MW (Gomez et al., 2015), disturbing the Galactic disc (Laporte et al., 2018) and inducing a large-scale gravitational "wake" in the stellar and dark matter halos (Garavito-Camargo et al., 2019). Clearly the accretion of the

LMC is a significant, transformative event in our Galaxy's history.

In addition to hosting the LMC, the MW has other peculiarities. Its central supermassive black hole has an abnormally small mass compared to other galaxies of similar stellar mass (e.g. Savorgnan et al., 2016); its satellite system has a strange planar alignment perpendicular to the MW disc (e.g. Lynden-Bell, 1976; Libeskind et al., 2005; Metz et al., 2008); the chemodynamical properties of the bulge suggest an uncommonly quiet merger history (Fragkoudi et al., 2020); and the Galactic stellar halo may be unusually low-mass and metal-poor (e.g. Bell et al. 2017; Harmsen et al. 2017, but see Conroy et al. 2019; Deason et al. 2019). Some of these seemingly atypical qualities could be explained by the paucity of mergers experienced by our Galaxy. For example, it is expected that our forthcoming merger with the LMC (in a couple of gigayears time) may return the MW back to "normality" (Cautun et al., 2019). In view of all these peculiarities, a natural question to ask is how similar or different is the MW assembly history to that of other galaxies of similar mass?

A fundamental prediction of the ΛCDM model is that MW-mass galaxies grow by accretion and mergers with smaller galaxies. Simulations show that large stellar halos form as a result of these accretion events (Bullock & Johnston, 2005; Abadi et al., 2006; Font et al., 2006; Cooper et al., 2010). Dynamical timescales in the stellar halo are long, so the phase-space distribution of halo stars can retain some memory of the past accretion events. Moreover, the chemistry of the debris of merger events reflects that of the progenitor galaxies: more massive dwarfs are more metal-rich than lower mass dwarfs, and have distinct sequences in chemical abundance space (e.g. Tolstoy et al., 2009). Hence, by analysing the stellar phase-space and chemistry properties, it may be possible to identify different accretion events. The link between the chemodynamics of halo stars and the Galaxy's assembly history can be traced back to the early work by Eggen et al. (1962). More recently, our view of the Galaxy has been transformed by the availability of 6D phase-space information for large numbers of halo stars provided by large astrometric, photometric and spectroscopic surveys.

The *Gaia* mission, in particular, is providing new detailed insights into the assembly history

of the MW. The first and second data releases led to the discovery of an ancient merger event, discovered independently by two teams who called it "Gaia Enceladus" (Helmi et al., 2018) and "Gaia Sausage" (Belokurov et al., 2018) respectively; here we will refer to both jointly as the Gaia-Enceladus Sausage (GES)^. For more details about the discovery of GES, see section 1.4.3.

In addition to halo stars, globular clusters can be used to identify accreted dwarf galaxies since, by virtue of their high stellar mass density, they are able to survive tidal disruption long after the dwarf galaxy, that brought them into the MW, has been destroyed (e.g. Kruijssen & Zwart, 2009; Penarrubia et al., 2009). Recent work using *Gaia* DR2 shows that the Galactic globular cluster population also points to a GES merger event (Myeong et al., 2018; Pfeffer et al., 2020). In particular, Myeong et al. (2018) show that at least eight Galactic globular clusters are likely to be associated with the GES. However, in addition to the GES, the globular cluster population has possibly revealed two additional merger events: Sequoia and Kraken (Myeong et al., 2019; Kruijssen et al., 2020). Sequoia is thought to have merged with the MW around the same time as the GES, but the progenitor had a much lower mass (Myeong et al., 2019). Kraken is thought to be much older (accretion at $z > 2$), but may have an even higher mass ratio relative to the MW than the GES merger (Pfeffer et al., 2020). The existence of this latter event is still under debate, and it may be more difficult to identify in the halo stars as its stellar debris likely occupies the inner few kiloparsecs of the Galaxy.

In view of the recent advances in our knowledge of the assembly history of the MW, the aim of this chapter is to characterise MW-like galaxies in cosmological simulations that have similar past accretion events to our own galaxy. Specifically, we use the cosmological hydrodynamics EAGLE simulation (Schaye et al., 2015; Crain et al., 2015) to identify MW-mass systems that underwent mergers analogous to *both* the LMC and GES events. Previous studies have considered MW-like galaxies with either an LMC *or* a GES event (e.g. Bignone et al., 2019; Cautun et al., 2019; Elias et al., 2020), but not both as seems

^Note, however, that it is still debated whether or not these two discoveries are describing exactly the same event (e.g. Evans, 2020; Elias et al., 2020)

appropriate for the actual MW. The "classical" view of the LMC (e.g. Cautun et al., 2019) allows for a variety of previous mergers but does not include the paucity of massive merger events experienced by the MW between the recent infall of the LMC and the ancient merger of the GES. This chapter aims to explore differences amongst galaxies that experience late (LMC), early (GES) merger events, or both. In particular, we aim to establish how unusual it is for a MW-mass galaxy to have both these events and a dearth of massive mergers in between.

The chapter is arranged as follows. In Section 2.2 we describe the simulations used for our analysis and our sample selection. In Section 2.3 we present our results; we discuss and summarise our conclusions in Section 2.4.

2.2 Simulations

We now give a brief overview of the EAGLE simulations. We also describe the selection criteria for our MW-mass galaxies, and the reasoning behind each choice.

2.2.1 EAGLE

We aim to identify MW analogues in the 100 Mpc EAGLE simulation (Schaye et al., 2015; Crain et al., 2015; McAlpine et al., 2016), which have either an LMC-mass satellite, an ancient merger similar to the GES, or both an LMC and a GES event. Further details about the EAGLE simulation are presented in Section 1.3.3.

In this chapter, infall time or accretion time is defined as the time when a galaxy crosses the R_{200} radius of the host. In practice, we take the snapshot immediately before the crossing. Finally, merger time is defined as the last snapshot at which an accreted galaxy was identified by SUBFIND, before it merges with the host or is destroyed.

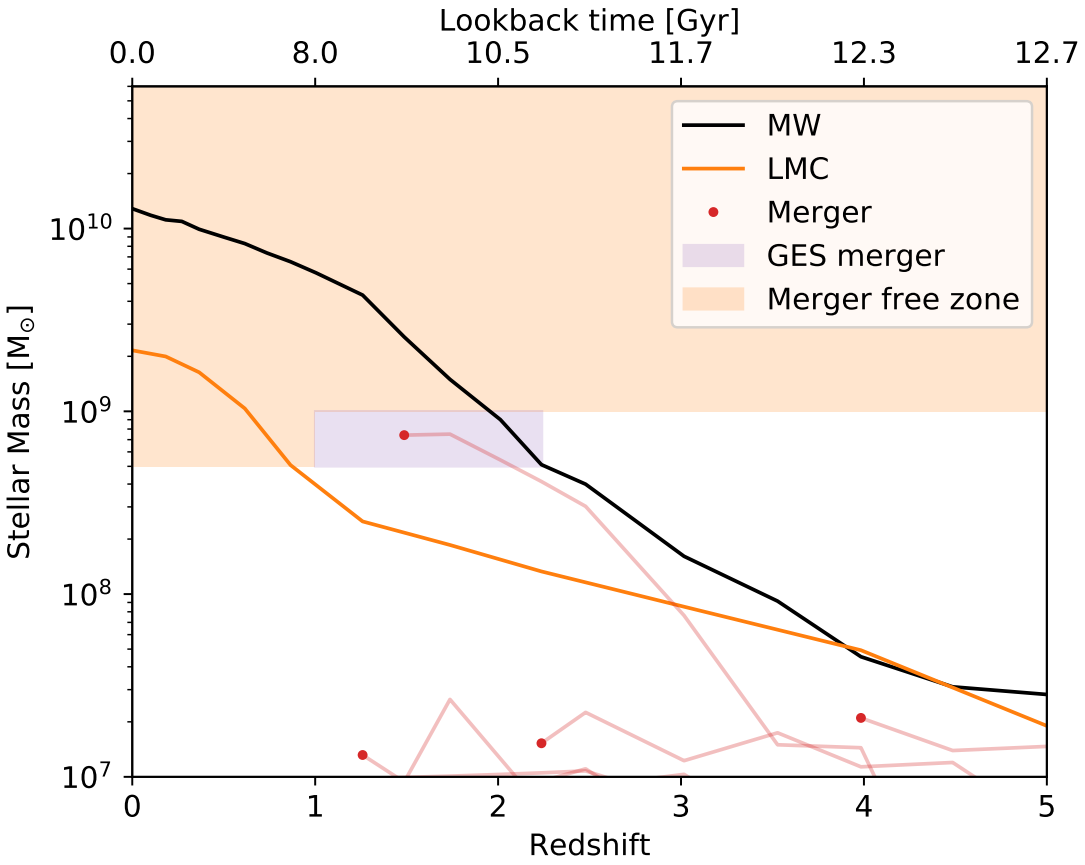

Figure 2.1

An example of mass growth and merger history of a MW-mass galaxy in EAGLE. The black and orange solid lines show the stellar mass of the main MW progenitor and its LMC satellite from $z = 5$ to $z = 0$. Light red lines correspond to all dwarf galaxies (above stellar mass of 10^7 $M_\odot$) that merged with the MW halo. Red dots mark the merger time (i.e. the latest snapshot where the progenitors were identified). The orange shaded region illustrates the area which, according to our criteria (Sec. 2.2.2), should be merger free. The purple shaded region illustrates the criteria for when a GES merger should occur.

2.2.2 Sample selection

We first identify all galaxies with a present-day dark matter halo in the mass range $(0.7 - 2) \times 10^{12} \mathrm{M}_{\odot}$ (see Callingham et al., 2019, and references therein). This sample comprises $N = 1078$ halos. We then impose further restrictions based on assembly history.

The LMC is a relatively massive satellite, $M_* = 1.5 \times 10^9\ \mathrm{M}_{\odot}$, with a small Galactocentric distance, $d_{GC} = 50$ kpc, and moves with a large tangential speed (McConnachie, 2012; Kallivayalil et al., 2013). The Galactocentric distance and velocity of the LMC indicate that it is close to the pericentre of its orbit. We do not impose any constraint on the orbit of LMC-mass satellites and only require that the stellar mass of the satellite galaxy should lie in the range $(1 - 4) \times 10^9 \mathrm{M}_{\odot}$, and the satellite be located within R_{200} of the host halo at $z = 0$. We additionally require that no other satellite more massive than the LMC exists within the R_{200} radius of the MW-mass hosts at $z = 0$. We do not impose a constraint on the infall time of the LMC-mass satellite. However, since these massive satellites survive to $z = 0$, they typically infall at late times.

The details of the GES-like event are more uncertain since it is a fairly new discovery. However, the stellar mass is likely to be in the range $(0.5 - 1) \times 10^9 \mathrm{M}_{\odot}$ and it is thought to have merged with the MW between 8 Gyr and 11 Gyr ago (Belokurov et al., 2018; Fattahi et al., 2019; Mackereth et al., 2019)[†]. We impose no orbital constraint on the GES event. Similarly to the LMC constraint, we require that there was *only one* GES-mass accretion event in this time period (with no merger with a galaxy more massive than the GES). Finally, we impose the conditions that there should be no massive accretion events with progenitor stellar mass $M_* > 0.5 \times 10^9\ \mathrm{M}_{\odot}$ in the interval between the GES merger event and the infall of the LMC, and also that there should have been no massive accretion events prior to the accretion of the GES. Our constraints do, however, allow lower mass accretion events such as Sgr and Sequoia to occur between the merger with the GES and the infall of LMC. We do not consider the accretion of a Kraken-like event since it is suspected that this

[†] Fattahi et al. (2019) find a slightly higher stellar mass for the GES progenitors in the Auriga simulations. However, the stellar masses in Auriga subhalos are slightly overestimated.

happened before the GES event. A brief summary of the selection criteria are as follows:

(i) MW analogue has $M_{200} = (0.7 - 2) \times 10^{12} M_{\odot}$.

(ii) LMC exists at $z = 0$ within R_{200}, with stellar mass $M_{*} = (1 - 4) \times 10^{9} M_{\odot}$.

(iii) GES merger event of mass $M_{*} = (0.5 - 1) \times 10^{9} M_{\odot}$ occurs at $t = 8 - 11$ Gyr.

(iv) A 'merger-free zone' (orange shaded region in Fig. 2.1) when there are no massive accretion ($M_{*} > 0.5 \times 10^{9}\, M_{\odot}$) events between the time of the merger of the GES and the infall of the LMC or prior to the merger with GES.

In order to apply these criteria, we used merger trees to follow the assembly history of the MW-mass galaxies. Fig. 2.1 shows an example of a MW-mass galaxy in EAGLE, and helps to visualise the constraints imposed by the different selection criteria. The black and orange lines show the main branch of the simulated MW galaxy and its LMC satellite respectively. The red dots represent dwarf galaxies (above stellar mass of $10^{7}\, M_{\odot}$) which have merged onto the MW main branch, the light red lines show the main branch of the merging dwarfs up until they have completely merged with the MW. The orange and purple shaded regions show the mass and redshift zones for the merger-free area, and the area in which a GES merger should occur.

Throughout this chapter, the properties of MW-mass galaxies are compared in the "categories" described below. These groupings were chosen to clarify how having either, or both of the LMC and GES would have influenced the Galaxy's evolution. These categories are:

(i) All MW-mass galaxies (MW-all).

(ii) MW-mass galaxies which have an LMC within R_{200} at $z = 0$ with no merger history constraint. This is the "classical" MW with LMC studied in many previous papers (LMC-all).

(iii) MW-mass galaxies which have an LMC within R_{200} at $z = 0$, but did not experience a GES merger event or accrete any other massive dwarfs of mass $M_* > 0.5 \times 10^9\ M_\odot$ (the 'merger free zone' shown in Fig. 2.1; LMC-o).

(iv) MW-mass galaxies which have a merger event similar to the GES, but do not have an LMC satellite at $z = 0$ and did not accrete any other massive dwarfs (as in LMC-o; GES-o).

(v) MW-mass galaxies which have both a LMC, a GES event, and a 'merger free zone' during which no object more massive than the LMC or the GES is accreted. This final group (LMC & GES) most closely describes the true MW galaxy[‡].

The number of galaxies that meet these criteria is presented in Table 2.1, along with the percentage of MW galaxies that belong in each category and their median stellar and halo masses. More details for the LMC & GES category are presented in Table 2.2. Our values for the fraction of MW-mass halos in the LMC-o or GES-o categories are significantly higher than those stated in Bignone et al. (2019) and Cautun et al. (2019). Cautun et al. (2019) found only eight MW analogues in the EAGLE simulation which had an LMC-mass satellite; however, that work applied more restrictive constraints to the sample. For example, the mass of the cold gas content and the black hole mass were also considered in the constraints. Bignone et al. (2019) found only one MW galaxy with a GES type merger event in the EAGLE simulation; however, that work also imposed constraints on the current star formation and the disc of the MW, and, importantly, required that the stellar debris from the GES event be highly anisotropic.

Our constraints are deliberately imposed to depend only on the mass and time of significant accretion events in the MW's history. Anything more restrictive would result in a very small sample size. The fraction of MW halos with 'classical' LMCs (LMC-all) is slightly higher than the observed value ($\sim 10\%$, see e.g. Liu et al. 2011; Tollerud et al. 2011) but, again, our constraints are less restrictive (e.g. no constraint on present-day position, or

[‡] Kruijssen et al. (2020) found a lower mass for the GES than used in this chapter. However, their findings for the MW assembly history are consistent with the LMC-o sample of galaxies presented here.

Table 2.1

The MW-mass galaxies included in our sample. The columns give: the name of each group, the number of galaxies in each group, the percentage of the MW-all category that are in each group, the median stellar mass, the median halo mass, the stellar mass to halo mass relation, the median absolute deviation (MAD) of the stellar and halo masses.

Group	Number of galaxies	Percentage	Median M_* ($\times 10^{10}$ M$_\odot$)	Median M_{200} ($\times 10^{12}$ M$_\odot$)	M_*/M_{200} ($\times 10^{-3}$)	MAD M_* ($\times 10^{9}$ M$_\odot$)	MAD M_{200} ($\times 10^{11}$ M$_\odot$)
MW-all	1078	-	2.03	1.04	19.5	9.03	3.48
LMC-all	169	15.7%	1.78	1.12	15.9	9.83	4.25
LMC-o	40	3.7%	1.30	0.87	14.9	7.12	2.11
GES-o	54	5.0%	1.74	0.92	18.9	5.68	1.97
LMC & GES	7	0.65%	1.44	0.80	18.0	7.13	0.53

Table 2.2

The final sample of 7 MW analogues with LMC & GES. The columns give: (a) EAGLE halo ID, corresponding to the halo ID in the top left of Fig. 2.3; (b) M_{200} of the MW halo at $z = 0$; (c) the maximum stellar mass recorded for the destroyed GES; (d) the redshift at which the GES merged; (e) maximum stellar mass of the LMC analogue; (f) redshift at which the LMC analogue crossed the R_{200} radius of the MW; and (g) the number of satellites within R_{200} of the MW analogues with stellar mass, $M_* > 10^6\,\mathrm{M}_\odot$.

EAGLE Halo ID (a)	MW M_{200} ($\times 10^{12}\,\mathrm{M}_\odot$) (b)	GES $M_{*,max}$ ($\times 10^{8}\,\mathrm{M}_\odot$) (c)	GES merger redshift (d)	LMC $M_{*,max}$ ($\times 10^{9}\,\mathrm{M}_\odot$) (e)	LMC infall redshift (f)	Number of satellites (g)
8806615	1.13	5.2	2.01	2.16	0.37	6
9293658	0.99	5.4	1.00	1.29	0.27	8
9372228	0.76	7.4	1.49	2.16	0.27	9
9626514	0.80	6.2	1.00	1.26	0.1	13
9798319	0.80	9.0	1.74	1.27	0.74	12
9968042	0.79	7.8	1.00	1.46	0.37	6
10058549	0.71	9.9	1.26	3.34	0.62	10

orbit of the LMC). The final value for the fraction of MW galaxies with both an LMC and a GES merger event, and nothing significant in between, is only 0.65% of all MWs in EAGLE – this is already an indicator that our Galaxy's assembly history is very rare.

Four representative galaxies from our final LMC & GES sample are illustrated in Fig. 2.2 and Fig. 2.3. The former shows mock *gri* face-on images of the central galaxies at $z = 0$, where face-on has been defined according to the stellar angular momentum axis (Trayford et al., 2017)[§]. The images have been retrieved from the EAGLE public database[¶]. They have been produced by post-processed ray-tracing using a version of the code SKIRT (Camps & Baes, 2015); please see Trayford et al. (2017) for more details. Fig. 2.3 shows 2D projections of the dark matter particles in a $(500\text{kpc})^3$ region around the four halos. The outer and inner circles mark the R_{200} and $0.5 \times R_{200}$ boundaries. The LMC-mass satellite is highlighted in each halo with a red circle.

2.3 Results

We now present an overview of the properties of our various MW-mass categories defined in the previous section and their assembly histories. We start by examining the stellar and halo mass distributions and the stellar mass – halo mass relation.

The halo mass distributions of our different MW-mass categories are displayed in the top panel of Fig. 2.4. The black line shows the distribution of halo masses for the MW-all sample. The mass distributions are approximately linear, with a slight bias towards lower mass halos, as expected from the power law halo mass function in ΛCDM in this mass range (Jenkins et al., 2001). The decrease in halo mass distributions at the lowest mass bins are an artefact introduced by the kernel density estimation (KDE) used for smoothing. The LMC-all sample (dashed orange line) follows the general MW-mass halo trend closely, although it is flatter and less biased towards lower masses. This classical LMC-all group

[§] Note that Trayford et al. (2017) states that the galactic plane is not always easily defined, which could explain the irregularity of the leftmost image in Fig. 2.2

[¶] `http://virgodb.dur.ac.uk:8080/Eagle/`

Figure 2.2
Composite face-on *gri* images of four representative MW-mass galaxies in our final sample (LMC & GES) from the EAGLE reference simulation. Each panel is 60×60 pkpc wide. Details of the visualisation can be found in Trayford et al. (2017). Left to right, the EAGLE halo ID's are 9293658, 9372228, 9798319 and 10058549.

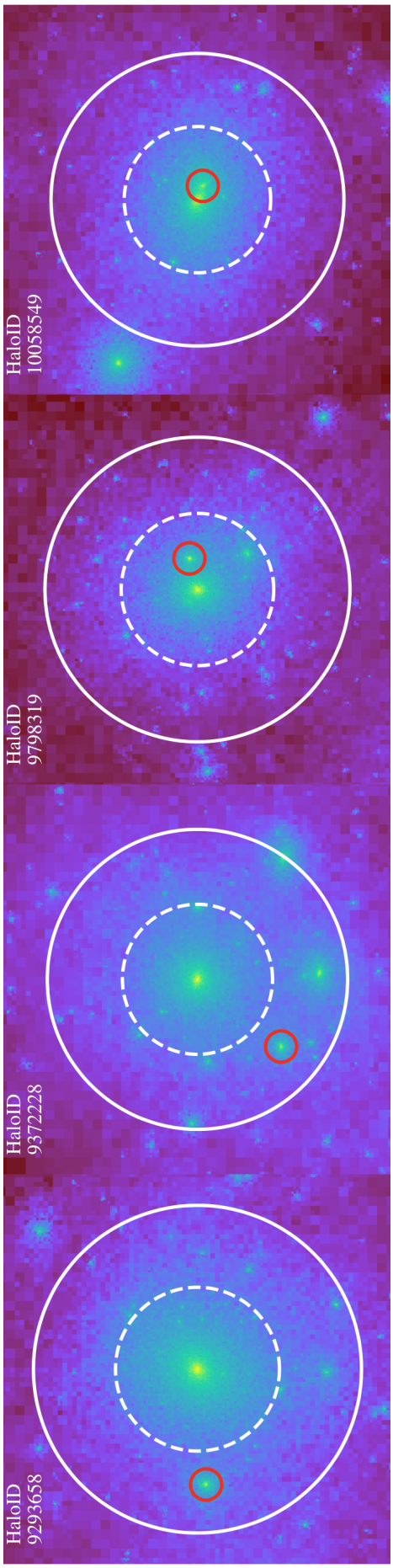

Figure 2.3
Distribution of dark matter particles for the corresponding galaxies shown in Fig. 2.2. The solid and dashed white circles represent the host R_{200} and $0.5\times R_{200}$ respectively. The smaller red circle shows the location of the LMC satellite. The EAGLE halo ID is shown in the top left-hand corner of each halo.

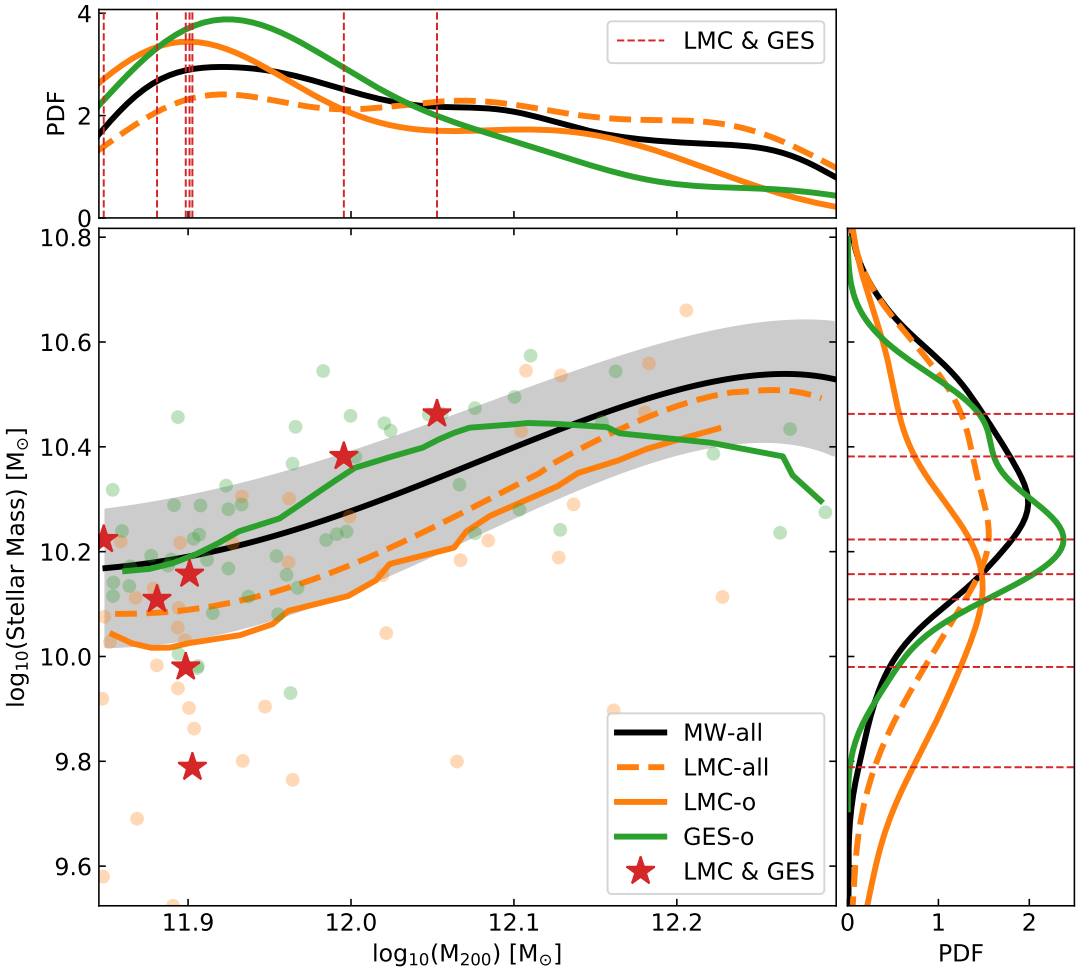

Figure 2.4

Central: stellar mass-halo mass relation at $z = 0$ for our different samples of MW-mass halos (see Sec. 2.2.2 for full details), as indicated in the legend. The lines represent the median values of the stellar mass in halo mass intervals. For the 'MW-all' sample we show the median absolute deviation (MAD) around the median as a shaded region, whereas for the other samples we show individual galaxies with the corresponding colour. The medians and the MAD were smoothed using a Savitzky-Golay filter (Savitzky & Golay, 1964). The red stars correspond to the individual galaxies in the final sample of MWs with LMC & GES. *Top:* M_{200} distribution of various MW-mass samples, smoothed with a KDE kernel. Vertical lines indicate individual galaxies in our LMC & GES sample. *Right:* similar to the top panel but showing the stellar mass distribution of MW-mass halos.

is different from the LMC-o group shown as the solid orange line, which has a more prominent peak towards lower masses.

Fig. 2.4 shows that the halo mass of the MW is shifted towards lower values for both the LMC-o and GES-o samples (medians of 0.87×10^{12} $M_\odot$ and 0.92×10^{12} $M_\odot$ respectively). This effect is further enhanced when the MW has both an LMC and a GES. The halo masses for the LMC-o and GES-o groups are biased low because they have a long quiescent period and thus, compared to the "typical" MW, have accreted less mass. The seven LMC & GES galaxies are represented individually by vertical dashed red lines. Halo mass, by definition, is all the mass within R_{200} and therefore includes the halo mass of the LMC-mass satellite.

The stellar mass-halo mass relationship is shown in the central panel of Fig. 2.4. The LMC-all and LMC-o samples appear to have a lower stellar mass compared to the total sample at any given halo mass. We, however, note that there are biases in the way halo and stellar masses are measured. The stellar mass includes the stellar particles within 30 kpc of the centre of the MW; however, the halo mass, M_{200}, includes all mass within the FoF group (i.e. including the halo of the LMC which is generally more than 30 kpc away from the centre). Therefore, the difference is not a shift down in stellar mass for MWs with an LMC but rather a shift to the right in the stellar mass-halo mass plane.

The central panel of Fig. 2.4 suggests that the GES-o category has a higher than average stellar mass for a given halo mass in the range $\log_{10}(M_{200}) = 11.9 - 12.1$. However, the stellar mass distribution shown in the right panel shows that there is a small peak at slightly higher stellar mass for the GES-o sample than the average MW peak, but the main peak for the GES-o sample is at a slightly lower stellar mass than the average. This is because this category is biased towards lower halo masses (see top panel), and thus lower, on average, stellar masses. For low halo masses ($\log_{10}(M_{200}) < 12$), the LMC & GES sample has lower than average stellar mass, but for higher halo masses ($\log_{10}(M_{200}) > 12$), it has higher than average stellar mass. However, the median relation in this mass range remains within the median absolute deviation of the MW-all category (shaded grey region). The former is due to the aforementioned reason for LMC samples; namely, the stellar mass is measured for the central galaxy but halo mass includes the mass of LMC.

The right panel of Fig. 2.4 shows the distribution of stellar masses for each category of galaxies. The LMC-o sample has a peak at lower stellar masses than the MW-all sample, reflecting the lower halo masses seen in the top panel. The stellar masses of the LMC & GES sample are distributed across the entire range of stellar masses.

2.3.1 Assembly history

Fig. 2.5 shows the evolution of stellar mass (left panel), M_{200} (middle panel), and the normalised halo mass ($M_{200}/M_{200,z=0}$; right panel) for each category of MW-mass galaxies. The thick lines show the median stellar mass and halo mass at each redshift for each sample.

The LMC-all category (dashed orange line) does not have any constraint on assembly history and is consistently lower in stellar and halo mass until the infall of its LMC-mass satellite. During infall, the LMC satellite gives rise to a sudden increase in halo mass, which leads to the LMC-all sample having the highest halo mass of all categories at $z = 0$. The LMC-o sample is consistently low in both stellar and halo mass. As in the case of the LMC-all sample, the LMC-o galaxies also show an increase in halo mass as the LMC-mass satellite is accreted by its host. However, unlike the LMC-all sample, the final halo masses are not particularly high, and, in fact, are lower on average than the MW-all sample. This difference reflects the fact that the LMC-o sample is constrained to have no other significant merger (other than the LMC), which naturally biases this sample to lower halo masses.

The GES-o group follows the MW-all sample more closely than the LMC samples. However, the stellar and halo masses of the GES-o category tend to grow more rapidly around the time of the GES merger, and this shows up as a "bump" in the central and right panels of Fig. 2.5 around $z \sim 1 - 2$. Preceding this event, the stellar and halo mass rise more slowly than the average MW sample since the MW-all sample experiences more continuous mergers than the GES-o, and therefore has a continuous influx of accreted mass.

Initially, the LMC & GES galaxies have stellar and halo masses that are lower than those of the LMC-o sample. These galaxies then follow the evolution of the LMC-o category

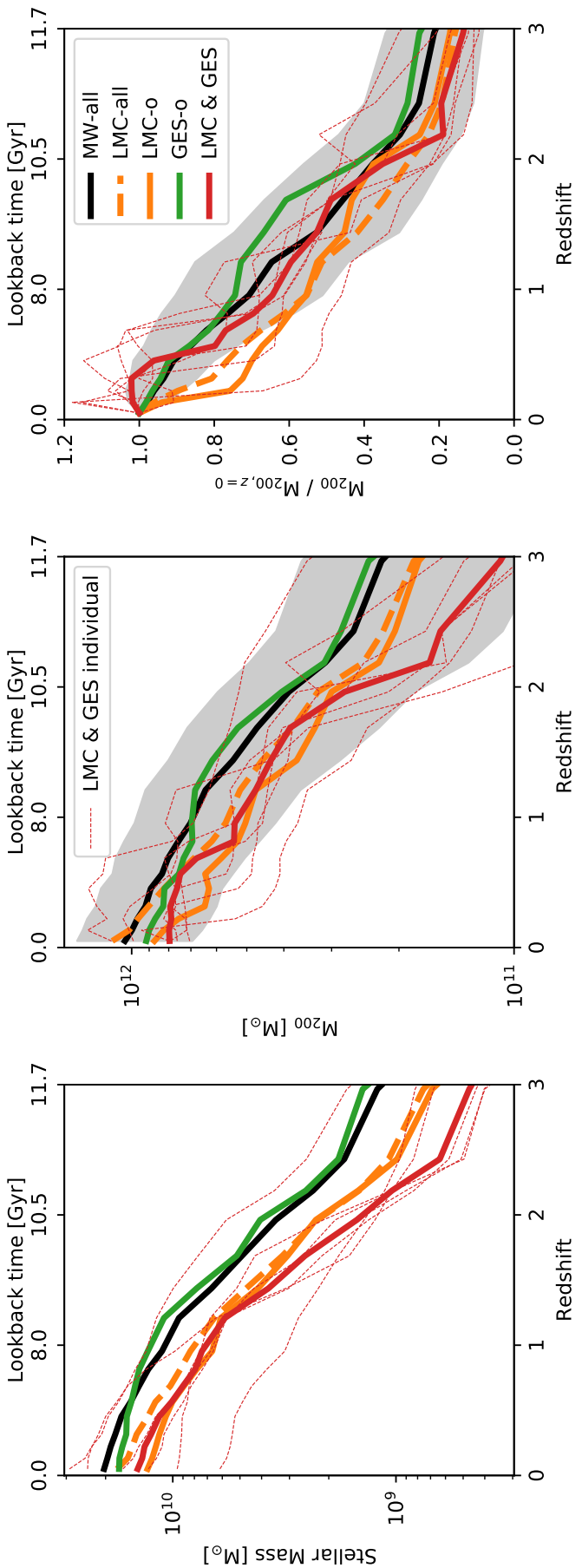

Figure 2.5
Left: median stellar mass as a function of redshift for different MW-mass samples. The colour coding and line styles are similar to those in Fig. 2.4. The shaded region represents the MAD around the median for the MW-all sample. The thin red dotted lines correspond to individual galaxies in the final LMC & GES sample. *Middle:* as the left panel, but for the halo mass, M_{200}, as a function of redshift. *Right:* as the middle panel, but for the halo masses normalised to the $z = 0$ value for each halo, as a function of redshift.

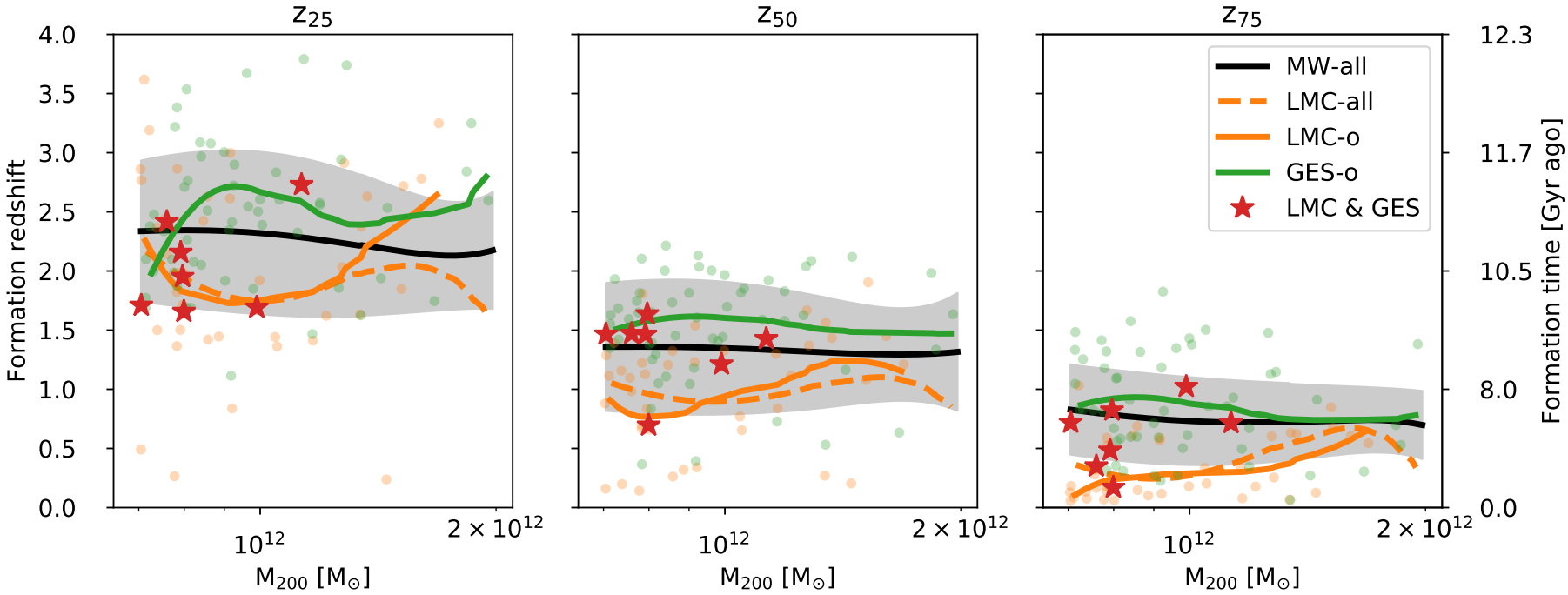

Figure 2.6

The formation redshifts of the MW-mass halos. *Left:* redshift when the halo has reached 25% of its $z = 0$ mass. *Middle:* redshift when the halo has reached 50% of its $z = 0$ mass. *Right:* redshift when the halo has reached 75% of its $z = 0$ mass. Colours, lines and symbols are similar to those of Fig. 2.4. The black line represents the median value of the redshifts for the MW-all category, and the grey shaded region represents the MAD for that category. The median lines were smoothed using a Savitzky-Golay filter.

until the merger with the GES at $z = 1 - 2$, when it also shows a bump in halo mass similar to that in the GES-o category. Some of the individual LMC & GES galaxies show a very sudden increase in halo mass (in some cases almost double in mass) because of the accretion of the LMC-mass satellite. The stellar mass growth is much smoother than the halo mass growth. There is no bump in the stellar mass corresponding to the bump in halo mass since not all stars go to the centre of the MW (i.e. within 30kpc, the aperture used to calculate the stellar mass). Evidently, the progenitors of the LMC & GES galaxies are considerably smaller than the other categories of MW-mass galaxies. The combination of the two events, the merger with the GES and the infall of the LMC, increases the halo mass of their MW galaxies enough to reach our minimum mass threshold. Hence, our results suggest that the main progenitor of the MW would have been much smaller than anticipated.

The difference in the assembly histories of our various MW categories is more apparent in the right-hand panel of Fig. 2.5, which shows the normalised halo mass as a function of redshift. There is a clear bump in the GES-o sample (green line) around the redshift of the GES merger with the MW. There is also clearly a sudden increase in halo mass of the LMC-o sample (solid orange line) at infall time of the LMC-mass satellite. Some of the LMC & GES individual galaxies (red dashed lines) go above $M_{200}/M_{200,z=0} = 1$, which is likely due to the definition of M_{200}. When a massive object such as the LMC is close to the virial radius (i.e. infalling), R_{200} is not very well defined and tends to increase in order for the mean density to drop to $200 \times \rho_{\rm crit}$. As a consequence, the mass in the boundary region also contributes to M_{200}, and this temporarily increases. After infall, LMC-mass subhalos quickly sink to the centre, and R_{200} (and thus M_{200}) goes back to 'normal'. Thus, the transient increase in M_{200} does not mean the MW-mass halos lose mass, but rather is a result of the definition of R_{200} and the accretion of massive subhalos. This feature is averaged out in the LMC-all and LMC-o samples due to the greater range of infall times for the LMC.

We use the normalised halo mass assembly to define halo formation redshifts, z_X, for each MW-mass galaxy as the time when the main progenitor branch of the merger tree reaches

X percent of the present-day M_{200}. Fig. 2.6 shows z_{25}, z_{50}, and z_{75} of our MW samples in the left, middle and right panels respectively.

Due to the sudden increase in halo mass resulting from the infall of the LMC-mass satellite, the formation redshifts of the LMC-all and LMC-o categories are shifted to lower values across all three panels. The z_{75} formation redshift is the most affected by this since this is roughly the infall time of the LMC-like satellites, particularly for the lower halo mass galaxies.

The GES-o sample has a consistently earlier formation redshifts across all three panels. The left panel suggests that the GES-o galaxies form 25% of their mass earlier than the other samples even before the merger with the GES. The middle panel shows that the z_{50} formation redshift occurs at roughly the same redshift as the merger with the GES, and the right panel shows that after the merger with the GES, the GES-o galaxies follow the MW-all sample more closely.

Overall, Fig. 2.6 suggests that the LMC & GES galaxies tend to have later z_{25} formation redshifts, similar to the LMC-o formation redshifts. This is expected since in that time interval the GES is only beginning to merge with the MW and so the galaxy has experienced roughly the same amount of merging as the LMC-o category. The middle panel shows that the z_{50} formation redshifts of the LMC & GES follow more closely the GES-o line, which is likely due to the merger of the GES occurring at roughly these redshifts. Finally, the right panel shows that the lower mass ($M_{200} < 10^{12}\,M_{\odot}$) LMC & GES return to follow the LMC-o lines for the z_{75} formation redshifts, likely due to the imminent infall of the LMC-like satellites. The two higher mass LMC & GES galaxies ($M_{200} > 10^{12}\,M_{\odot}$) do not follow the same trend as the lower mass galaxies at this epoch. This is likely because the accretion of the LMC-mass satellite is a proportionally larger accretion event for the lower mass LMC & GES galaxies. Figs. 2.5 and 2.6 show that the assembly history of the MW intricately follows the details of these two (GES & LMC) accretion events, and, at most redshifts, looks very different to the average MW-mass halo.

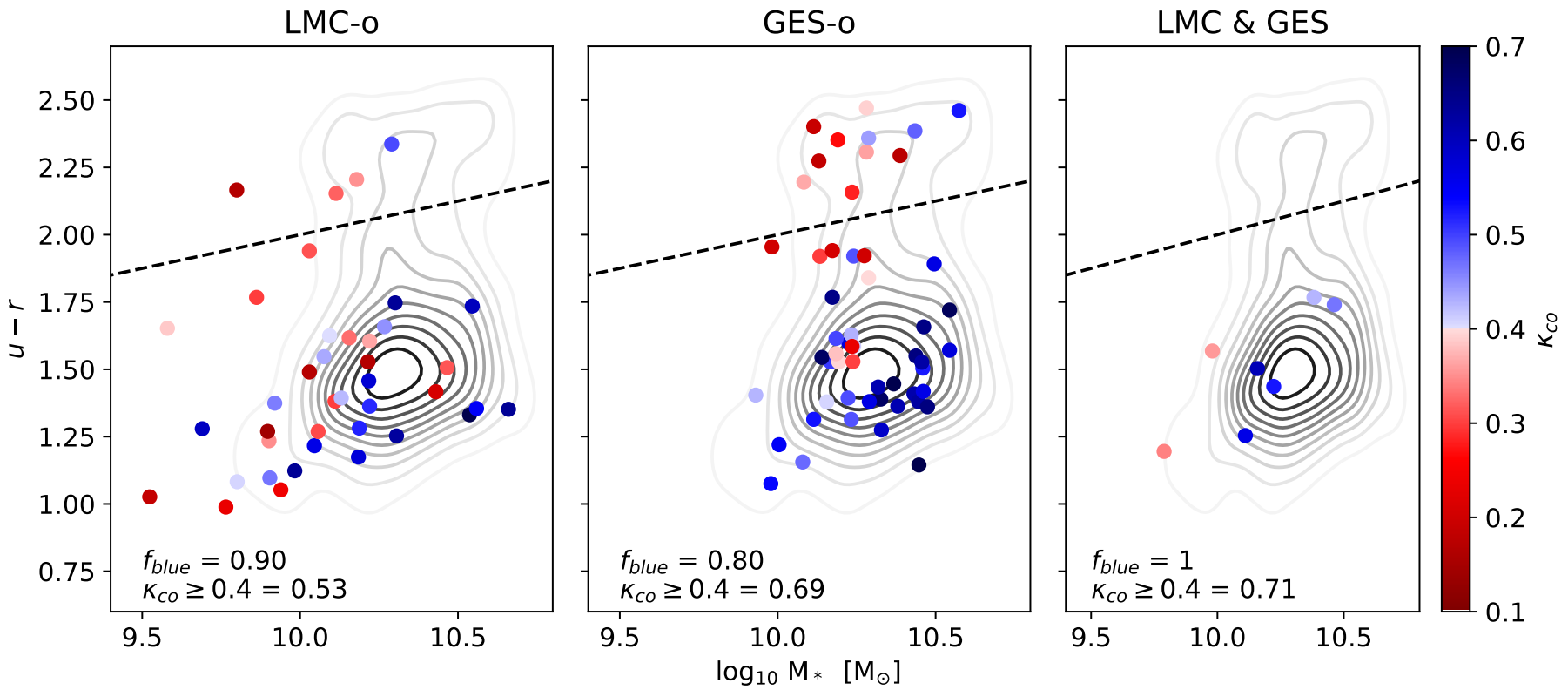

Figure 2.7

The $u - r$ colour *vs* stellar mass diagram for MW-mass galaxies. The panels correspond to the LMC-o (left), GES-o (middle) and LMC & GES (right) samples. The grey contours are repeated in all panels and show the colour-stellar mass distribution for the 'MW-all' sample. Galaxies are represented by red or blue according to a cut in their κ_{co} values at $\kappa_{co} = 0.4$, as shown by the colour bar. The dashed black line marks the separation of the red sequence from the blue cloud. The legend gives the fraction of blue galaxies (f_{blue}) and the fraction of disc galaxies ($\kappa_{co} \geq 0.4$).

2.3.2 Galaxy colour and morphology

Assembly histories are reflected in the morphology of galaxies. Our selection of samples of MW-mass galaxies with different constraints (Section 2.2.2) does not include any criteria for the MW to be a star-forming spiral galaxy rather than a red, non-star forming elliptical galaxy. In this section, we show how the assembly history affects the $z = 0$ colours of our galaxies.

To characterise the MW-mass galaxies we consider their colour and morphology. The rest-frame absolute magnitude without dust attenuation was used to estimate the colour; see Trayford et al. (2015) for details. We adopt the threshold defined by Schawinski et al. (2014) to label galaxies as blue or red (dashed line in Fig. 2.7). The fraction of blue galaxies for the MW-all sample is $f_{blue} = 0.82$.

Fig. 2.7 shows the colour-stellar mass diagram for our MW-mass halos. The grey contours, repeated in all panels, correspond to the distribution for the MW-all group which is clearly bimodal showing a red sequence and a blue cloud. Different panels correspond to the various categories of MW-mass galaxies, as labelled, with the colour of each point indicating whether they are disc (blue) or elliptical (red) galaxies. To characterise morphology we use the stellar kinematics morphological indicator introduced by Sales et al. (2012) and calculated for EAGLE galaxies by Correa et al. (2017). The fraction of disc galaxies (i.e. with $\kappa_{co} \geq 0.4$) for the MW-all sample is 0.6.

The left panel shows that the LMC-o sample contains more blue galaxies than average, with $f_{blue} = 0.9$. This is likely due to the late formation redshift discussed previously, and the restriction that there should be no significant mergers until the LMC infall. However, fewer galaxies in the LMC-o sample are disc galaxies compared to the MW-all sample. This slightly lower disc fraction is likely due to the LMC-o sample galaxies having lower stellar masses than average (see Fig. 2.4). In addition, some of the discs could have been disturbed by the infalling LMC. The middle panel shows that the GES-o sample contains a similar fraction of blue galaxies as the MW-all sample but a much higher fraction of disc galaxies. Since GES-o galaxies experience an early merger event (and hence have

an earlier formation redshift) they are more likely to become redder with time. The right panel shows that the LMC & GES galaxies are all in the blue cloud. This is consistent with the trend seen in the LMC-o sample that the later forming galaxies are more likely to be bluer. The LMC & GES sample also has the highest fraction of disc galaxies, 0.71, similar to the GES-o sample.

2.3.3 Satellite population

In this subsection we examine the satellite population of our MW samples and investigate whether the LMC & GES sample is different in this respect to the other samples. As shown in the simulations of the APOSTLE project (Sawala et al., 2016; Fattahi et al., 2016), the EAGLE model reproduces well the observed stellar mass function for dwarf galaxies, both those that are satellites orbiting in the MW and those in the field around the Local Group. Several important properties of dwarf galaxies, such as their sizes and star formation histories, are also consistent with observations (Sales, 2016; Sawala et al., 2016; Campbell et al., 2017; Digby et al., 2019; Bose et al., 2019, 2020).

The number of 'luminous' satellites as a function of halo mass for our various samples is shown in Fig. 2.8. Since EAGLE does not resolve ultra-faint dwarfs, the satellites plotted are those with stellar mass above $M_* > 1 \times 10^6 M_\odot$ that are within the virial radius of the MW-mass halos. The mass and number of satellites above this stellar mass within the M_{200} radius of our Galaxy is shown as a blue open star symbol. Here, the halo mass of the MW and its R_{200} radius are taken from Callingham et al. (2019) and the stellar masses and Galactocentric distances of the MW satellites from McConnachie (2012). The number of satellites with $M_* > 1 \times 10^6 M_\odot$ around MW-like galaxies is in agreement with other hydrodynamical simulations (e.g. Okamoto et al., 2010; Zolotov et al., 2012; Sawala et al., 2016; Wetzel et al., 2016; Simpson et al., 2018; Garrison-Kimmel et al., 2019).

Fig. 2.8 shows the well-known correlation between the number of satellites and the halo mass (Wang et al., 2012). The LMC-all and LMC-o samples have slightly higher numbers of satellites at fixed halo mass than the MW-all sample. This is probably because the

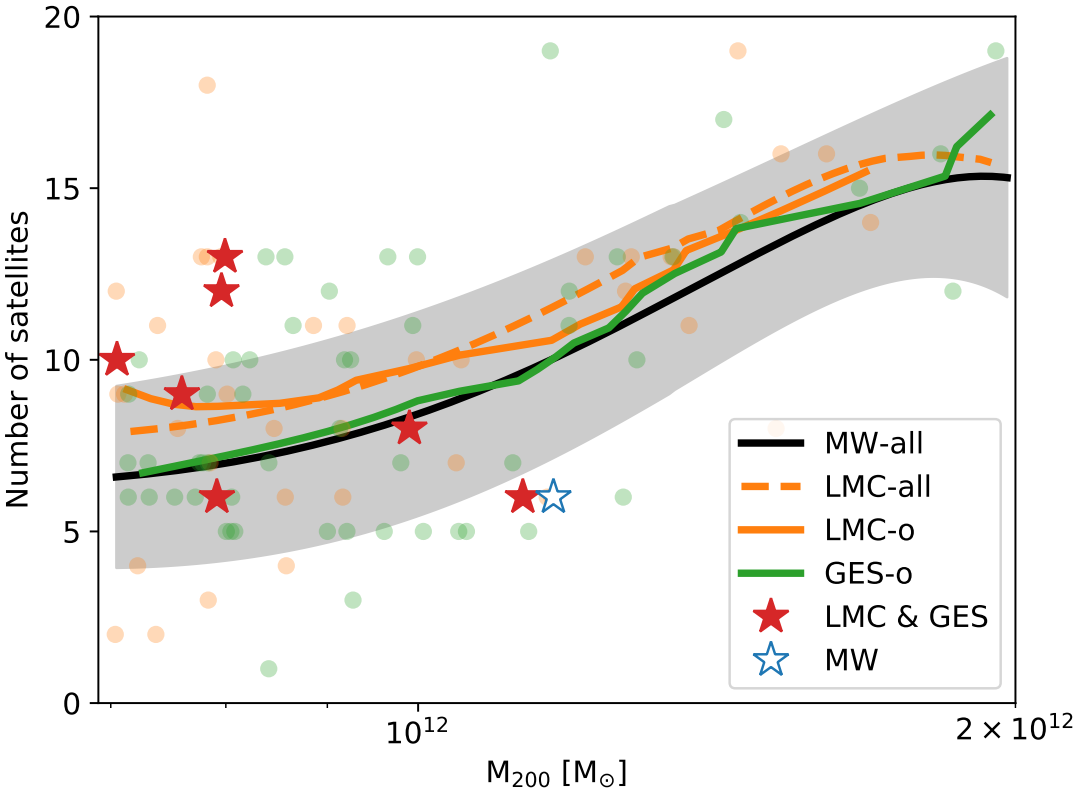

Figure 2.8

Number of satellites of stellar mass, $> 1 \times 10^6$ $M_\odot$, within the radius R_{200} for the host, as a function of host halo mass, M_{200}, for various samples of MW-mass galaxies. The colours, lines and shading are similar to those in Fig. 2.4. The blue open star shows the number of Galactic satellites with stellar mass above 10^6 $M_\odot$. R_{200} and M_{200} for the MW halo have been taken from Callingham et al. (2019).

LMC-mass dwarfs would have brought in their own satellite cohorts (Shao et al., 2019). Santos-Santos et al. (2021) showed that an LMC-like satellite is likely to have brought in approximately 2-3 satellites of its own to its MW-like host with masses greater than $M_* > 10^5\,M_\odot$, which would account for the excess satellites in the LMC-o and LMC-all categories. The GES-o sample has a very similar trend to the MW-all sample, possibly because these galaxies have a similar late-time assembly history to the MW-all galaxies (Fig. 2.5 right panel) when the bulk of the satellite population is accreted (Fattahi et al., 2020). At low halo masses, the infall of the LMC-like satellite (in LMC-all, LMC-o and LMC & GES samples) has a much larger impact as it is fractionally much larger compared to the host than for higher halo mass MW galaxies. We also examined the radial distribution of satellites and found no discernible differences between the different categories of MW-like galaxies. However, we note that we do not take "orphan" satellites into consideration, which can make a substantial difference to the radial profiles (Bose et al., 2020).

2.4 Discussion and Conclusions

We have used the EAGLE hydrodynamical simulation to assess the extent to which the two known major accretion events experienced by our Galaxy – the Gaia-Enceladus Sausage (GES) merger at early times and the more recent infall of the LMC – have shaped the properties of our galaxy. We have also tested whether these events make the MW stand out amongst galaxies of similar mass.

We identified 1078 MW-mass halos in the mass range $M_{200} = (0.7 - 2) \times 10^{12}\,M_\odot$ and subdivided this sample into three: *(i)* galaxies with an LMC-mass satellite within their virial radius at $z = 0$ (LMC-all sample); *(ii)* galaxies with an LMC as in *(i)*, but which did not experience a GES merger event or accrete any other more massive dwarfs than that in the past 8 Gyrs (LMC-o sample); *(iii)* galaxies that experienced a merger between $z = 1 - 2$ similar to the GES but no further large mergers (GES-o sample); and *(iv)* galaxies that experienced both a GES merger and the accretion of an LMC-mass satellite but no other

significant mergers in between these two (LMC & GES sample). Only 7 galaxies fall in the last category; their assembly histories bear the closest resemblance to the assembly history of the MW, as far as it is currently known. Our main conclusions are as follows:

- In agreement with earlier work, we find that the presence of an LMC-mass satellite orbiting a MW-mass galaxy is relatively uncommon: only 15.7% of galaxies fall in our LMC-all category. However, once the constraint is imposed that there should have been no massive mergers in the past 8 Gyr, the frequency is reduced to 3.7% (LMC-o). The number of MW-mass galaxies with a GES event between $z = 1 - 2$ (GES-o) amounts to 5% of the total sample. These fractions are slightly higher than in other studies (e.g. Cautun et al., 2019; Bignone et al., 2019) because of different ways of identifying the LMCs and GES in simulations.

- The assembly history of the MW is rare in the ΛCDM model: only 0.65% of MW-mass EAGLE galaxies have both an early GES merger and a late LMC infall and no significant mergers in between. This sample most closely resembles the assembly history of the Milky Way.

- The existence of an LMC or a GES event selects halos towards the lower end of the mass range we considered. Requiring both events further lowers the halo mass. The bias towards lower halo masses for these samples is due to a long period of quiescence during which the halos did not accrete as much mass as a "typical" MW galaxy.

- At a fixed halo mass, galaxies with an LMC (with or without the restriction on past mergers) have lower than average stellar mass. This bias is partly a matter of definition since the stellar mass of the galaxy is measured within 30 kpc, well inside the position of a typical LMC, whereas the mass of the halo is measured out to R_{200}.

- Halos destined to accrete an LMC have lower than average mass at early times but "catch up" at late times once the LMC has been accreted. The GES-o sample closely follows the accretion history of the MW-all sample until the merger with the GES

around $z = 2$. The halo mass grows more rapidly during the GES event ($z \sim 1 - 2$); after that the increase in halo mass is slower. Halos in the LMC & GES sample have much lower initial masses but they experience large increases in mass at the time of the merger with the GES and the later infall of the LMC. As a result, the formation redshift of the LMC & GES halos (defined as the time when 50% of the final halo mass was in place) ends up being typical of halos of that mass.

- Although no constraints on the morphology, colour or star formation rate of the final galaxy were applied in the sample selection, the LMC & GES galaxies all fall in the "blue cloud" in the colour-stellar mass diagram. This is a reflection of the long period without massive mergers required for this sample. Using a kinematical diagnostic of galaxy morphology (the fraction of the kinetic energy invested in rotation), the LMC & GES galaxies are predominantly disc galaxies: whereas 60% of the MW-all sample are discs according to this definition, 70% of the LMC & GES sample are discs.

- Galaxies with an LMC have more satellites than galaxies without one, including those with a GES event. The excess is due to the additional satellite population brought into the MW halo by the LMC.

Our simulations indicate that the build-up of both the stellar and dark matter mass in the Milky Way were strongly influenced by the GES merger and the accretion of the LMC. We therefore expect the progenitors of the MW, perhaps accessible to observational study with forthcoming telescopes such as JWST, to be atypical of galaxies of similar mass today.

The main limitation of this work is the relatively small volume sampled by the EAGLE simulation: there are only 7 galaxies in the EAGLE volume that satisfy the main constraints we imposed for the assembly history to resemble that of the MW, namely an early GES merger, a late LMC infall and a quiescent phase in between. A larger simulation is required to understand in more detail the atypical properties of the assembly history of the MW.

CHAPTER 3

Observing EAGLE galaxies with JWST: predictions for Milky Way progenitors and their building blocks

---

3.1 Introduction

The *James Webb Space Telescope* (*JWST*) was designed to search for faint galaxies at the highest redshifts. Its primary imager, the Near InfraRed Camera (*JWST*/NIRCam), will cover wavelengths in the range $0.6 - 5\mu m$ and is expected to observe some of the earliest stars and galaxies (Beichman et al., 2012). These observations may reveal the early stages of galaxy formation and provide an important test of the Λ cold dark matter (ΛCDM) model of the universe, which predicts that galaxies are assembled hierarchically starting from small, faint fragments that form at high redshift.

Theoretical predictions are vital for the interpretation of the upcoming observations. Cosmological hydrodynamical simulations and semi-analytic modelling are the tools commonly employed for making such predictions (e.g. Tacchella et al., 2018; Cowley et al., 2018; Yung et al., 2019; Vogelsberger et al., 2020). For example Cowley et al.

(2018) and Yung et al. (2019) used semi-analytic modelling to predict galaxy luminosity functions for *JWST*/NIRCam passbands at various redshifts. Similarly, Vogelsberger et al. (2020) used the IllustrisTNG hydrodynamical simulations for the same purpose and provided tailored predictions for two *JWST* surveys: the *JWST* Advanced Deep Extragalactic Survey (JADES) and the Cosmic Evolution Early Release Science Survey (CEERS). Hydrodynamical simulations like this have the advantage that they can resolve the spatial distribution of gas in galaxies allowing the effects of dust to be calculated in post-processing. Several estimates already exist of the bright end of the luminosity function (e.g. Oesch et al., 2014; Finkelstein et al., 2015; Bouwens et al., 2015, 2021); *JWST* will extend these measurements to much fainter magnitudes.

As the best studied galaxy in the Universe, the Milky Way (MW) holds a special place in studies of galaxy formation and evolution. Recent advances, largely driven by data from the *Gaia* satellite (Gaia Collaboration et al., 2018), have painted a much more detailed picture of its assembly history than we had even a few years ago. In particular, a major accretion event, in which a large dwarf galaxy merged into the main progenitor was recently discovered, the 'Gaia-Enceladus' (Helmi et al., 2018) or 'Gaia Sausage' Belokurov et al. (2018) (hereafter GES; for more details about the GES discovery, see section 1.4.3). Another large accretion event that has been known for a long time is that of the Large Magellanic Cloud (LMC), now known to be a very massive satellite, with about 10 percent of the MWs mass (e.g Peñarrubia et al., 2016; Erkal et al., 2019). A massive accretion such as the LMC has been shown to be important when interpreting the satellite population of the MW and their orbital properties (Patel et al., 2017a,b). There are several other suggested merger events present in the MW's history, these events tend to be either lower in stellar mass or at higher redshifts and are not very well characterised (e.g. Kruijssen et al., 2020; Forbes, 2020; Naidu et al., 2020, 2021; Horta et al., 2021).

In this work we analyse MW analogues identified in the EAGLE cosmological hydrodynamics simulations (Schaye et al., 2015; Crain et al., 2015). Our goal is to make predictions for the properties of their progenitors that are, in principle, accessible to the *JWST*. We will consider the progenitors of average MW-like haloes (defined at $z = 0$), as well as those of

MW-analogues constrained by their accretion history. In Chapter 2 (Evans et al., 2020) we found that these analogues have lower mass at early times compared to average MW-like haloes, selected at $z = 0$. We also investigate the properties of the progenitors of the LMC and GES analogues.

This chapter is organised as follows. The simulations and details of our definitions of MW, LMC and GES analogues are discussed in Section 3.2. Our calculation of galaxy luminosities in the *JWST*/NIRCam passbands and the dust model we adopt are described in Section 3.3, where we also present predictions for properties of the overall galaxy population, such as the luminosity function at various redshifts. Results for the MW, LMC and GES progenitors are presented in Section 3.4. This chapter ends with a discussion of our main results and our conclusions in Section 3.5.

3.2 EAGLE simulations

Details of the EAGLE simulation are presented in Section 1.3.3. Specifics for this chapter are described below.

Unless otherwise stated, we use the fiducial EAGLE run which has a periodic cubic volume of $(100\text{Mpc})^3$ and was run with the 'REFERENCE' parameters (REF-L0100N1504 in the nomenclature of Schaye et al., 2015). The initial mass for gas and matter particles are 9.6×10^6 $\text{M}_\odot$ and 1.81×10^6 $\text{M}_\odot$, respectively.

For convergence checks at the low mass, we use an EAGLE run with 8× better mass resolution, but in a smaller volume, $(50\text{Mpc})^3$, which has been simulated with the 'RECAL' parameters (Recal-L0050N1504) run from the Exploring Neutral Gas in EAGLE (ENGinE) simulations (Sykes et al. in prep), this simulation has the same resolution as the L025N0752 run in Schaye et al. (2015). We do not use the latter due to the small size of the box and much fewer number of galaxies. This simulation has been run only up to $z = 2$ due to computational costs. For simplicity we refer to these runs as 'EAGLE-Ref' and 'EAGLE-Recal', hereafter.

The stellar mass (M_*) of galaxies adopted in this work is calculated by summing the masses of bound star particles within 30kpc of the centre of galaxies. A 30kpc radius is appropriate for MW-mass galaxies at redshift $z = 0$, since the majority of the stars are within this radius. At higher redshifts, where galaxies are smaller, this boundary will include all of the particles in the galaxy. Unless mentioned otherwise, we include galaxies with stellar mass above $10^7\,M_\odot$, corresponding to $N \sim 5$ and 44 star particles in the EAGLE-Ref and EAGLE-Recal runs, respectively. The stellar masses of EAGLE-Ref galaxies have been shown to converge down to $N \sim 5$ particles in Sawala et al. (2016).

3.2.1 Analogue definitions

In this work we make use of many different galaxy "groups", and thus provide clear definitions below. We define a MW-like galaxy as any galaxy in EAGLE-Ref with halo mass in the range $M_{200} = (0.7 - 2) \times 10^{12}\,M_\odot$ (see Callingham et al., 2019, and references therein). 'LMC-like' group includes satellites, located inside R_{200}* of any MW-like galaxy at $z = 0$, and have stellar masses in the range $M_* = (1 - 4) \times 10^9\,M_\odot$. 'GES-like' galaxies are any galaxies which have a stellar mass of $M_* = (0.5 - 1) \times 10^9\,M_\odot$ when they merge with a MW-like galaxy between redshift $z = 1$ and 2 (8-10 Gyr ago). Note that we do not place any constraints on having a Local Group environment, which could affect the formation epoch of our haloes (Santistevan et al., 2020).

Our 'MW analogues' are MW-like galaxies with additional constraints on their accretion history, following Chapter 2 (Evans et al., 2020):

- one LMC-like satellite present at $z = 0$ with no other more massive satellites
- one GES-like merger event with no more massive mergers within the same time-frame
- finally, we require that these systems have a 'merger free zone' when there is an absence of massive mergers ($M_* > 0.5 \times 10^9\,M_\odot$) between redshifts $z = 0$ and $z = 2$.

*The spherical radius with mean enclosed density 200 times the critical density of the universe

Table 3.1
The number of galaxies in each of the galaxy groups studied in this work and their median $z = 0$ and $z = 2$ stellar masses.

Group	Number	Median $M_{*,z=0}$ $[\times 10^9\,M_\odot]$	Median $M_{*,z=2}$ $[\times 10^8\,M_\odot]$
MW-like	1078	20.3	23.8
LMC-like	169	1.89	1.96
GES-like	234	–	6.40
MW-analogue	7	14.4	10.4
LMC-analogue	7	1.29	2.10
GES-analogue	7	–	4.79

The definition of LMC satellites and GES mergers are deliberately broad in the hope of having better statistics. Table 3.1 gives the number of galaxies in each of the groups used throughout this chapter and their median stellar masses at redshifts $z = 0$ and $z = 2$. More specific properties of the MW analogue systems are presented in Chapter 2.

3.3 Galaxy luminosities and colours

In this section we describe how we calculate the dust-free magnitudes of the simulated galaxies for *JWST*/NIRCam passbands, as well as the absolute rest-frame UV. We also describe the model adopted throughout this work to account for dust attenuation.

3.3.1 Dust-free magnitudes

We use the initial mass function (IMF), age and metallicity of simulated star particles, combined with publicly available stellar libraries to retrieve their spectral energy distributions (SEDs). We use the Flexible Stellar Population Synthesis (FSPS) code (Conroy et al., 2009; Conroy & Gunn, 2010) with the MESA Isochrones & Stellar Tracks (MIST, Paxton et al., 2011, 2013, 2015; Choi et al., 2016; Dotter, 2016) and MILES stellar library (Sanchez-Blazquez et al., 2006). The IMF adopted in the simulations is Chabrier

(Chabrier, 2003) with an initial mass range of $0.1 - 100\,M_{\odot}$. The stellar isochrones cover the following range of age and metallicity: $-2.5 \leq [Fe/H] \leq 0.5$ with 12 intervals, and $5 \leq \log(age/yrs) \leq 10.3$ with 107 equally spaced points (these intervals were predetermined by FSPS). We identify the isochrone with the nearest metallicity and age to the stellar particles. If any of the star particles lie outside the age-metallicity grid of isochrones, they are also assigned to the nearest isochrone^.

The magnitudes in various passbands are retrieved by applying the response of each filter to the SED, which is done automatically by FSPS. For galaxies at higher redshifts ($z > 0$), the SED is redshifted before applying the filter. The total magnitude of each galaxy is calculated by adding the flux of all bound star particles within $r < 30$kpc.

3.3.2 Dust model

We compute the dust attenuation for each star particle in the simulated galaxies using a semi-empirical approach, following a modified version of 'model B' in Vogelsberger et al. (2020). The only modification accounts for the fact that the gas component in the EAGLE simulation is represented by SPH particles, rather than Arepo's Voronoi mesh cells in IllustrisTNG (for more details about IllustrisTNG, and the differences with EAGLE, see section 1.3.3). We smooth the gas particles over a cubic grid, as detailed below. There are two different components to the dust model: resolved dust from the ISM, and unresolved dust from stellar birth clouds

Resolved dust

The resolved dust attenuation is caused by cold ($< 10^4$K) or star-forming gas in the interstellar medium (ISM) along the line-of-sight. Unless otherwise stated, the line of sight direction for each galaxy is random. We use the smoothing lengths of gas particles to smooth the density using the original EAGLE kernel, over a cubic grid with 1 kpc

^We have checked that only a small fraction (3%) of star particles fall outside this grid at $z = 4$. Hence they would have negligible effect on the overall luminosity of each galaxy.

spacing. We then carry out the following calculations (for more detailed information see Vogelsberger et al., 2020, section 3.2.2) to obtain the attenuation for each star particle,

$$\tau_V^{\rm res} = \tau_{\rm dust}(z)\left(\frac{Z_g}{Z_\odot}\right)^{\gamma}\left(\frac{N_H}{N_{H,0}}\right) \tag{3.3.1}$$

where N_H is the hydrogen column density along the line of sight 'in front' of the star particle, $\tau_{\rm dust}(z)$ is the redshift dependent scale factor for the optical depth which scales as the average dust-to-metal ratio (for a more detailed discussion about $\tau_{\rm dust}(z)$, see Appendix A), $\gamma = 1$ and $N_{H,0} = 2.1 \times 10^{21}$cm. The V-band optical depth, τ_V, values are then converted into the V-band dust attenuation using the following relation,

$$A_V^{\rm res} = -2.5\log_{10}\left(\frac{1 - e^{-\tau_V^{\rm res}}}{\tau_V^{\rm res}}\right). \tag{3.3.2}$$

Since the optical depth and dust attenuation are both specific to the V-band, they need to be converted to the optical depth and dust attenuation for the passbands we are interested in (*JWST*/NIRCam and absolute rest-frame UV). To convert from V-band attenuation to attenuation for a given wavelength, λ, we adopt the Calzetti et al. (2000) relation (modified by Kriek & Conroy, 2013, to include the UV bump) for local starburst galaxies such that:

$$A^{\rm res}(\lambda) = \frac{A_V^{\rm res}}{4.05}[k'(\lambda) + D(\lambda)]\left(\frac{\lambda}{\lambda_V}\right)^{\delta} \tag{3.3.3}$$

where $k'(\lambda)$ is the normalised attenuation curve for A_V:

$$k'(\lambda) = 4.05 + 2.659\begin{cases}\left(-1.857 + \frac{1.040\mu m}{\lambda}\right), \\ \text{for } 0.63\mu m < \lambda < 2.20\mu m \\ \left(-2.156 + \frac{1.509\mu m}{\lambda} - \frac{0.198\mu m^2}{\lambda^2} + \frac{0.011\mu m^3}{\lambda^3}\right), \\ \text{for } 0.12\mu m < \lambda \leq 0.63\mu m\end{cases} \tag{3.3.4}$$

and $D(\lambda)$ parameterises the UV bump which is given by:

$$D(\lambda) = \frac{E_b(\lambda\Delta\lambda)^2}{(\lambda^2 - \lambda_0^2)^2 + (\lambda\Delta\lambda)^2} \tag{3.3.5}$$

where $\lambda_0 = 217.5$ nm and $\Delta\lambda = 35$ nm are the central wavelength and full width half maximum (FWHM) of the UV bump respectively (Seaton, 1979; Noll et al., 2009). The shape of the attenuation curve is purely characterised by δ as shown by the relation between E_b and δ found by Kriek & Conroy (2013):

$$E_b = (0.85 \pm 0.09) - (1.9 \pm 0.4)\delta \tag{3.3.6}$$

we assume $\delta = 0$ in order to apply no correction to the attenuation curve other than the addition of the UV bump as in Vogelsberger et al. (2020). The overall correction for the magnitude for the resolved dust component, in any given filter, is therefore:

$$M^{\text{dust}} = M^{\text{dust-free}} + A^{\text{res}}(\lambda). \tag{3.3.7}$$

Unresolved dust

The unresolved dust component of the model accounts for the stellar birth clouds around young stars which are not resolved in EAGLE. We include this component by assuming that all star particles in a given galaxy will have the same dust attenuation from their birth clouds[†]. The birth cloud V-band optical depth is given by:

$$\tau_V^{\text{unres}} = \begin{cases} 2\langle\tau_V^{\text{res}}\rangle, & \text{for } t' \leq t_{\text{disp}} \\ 0, & \text{for } t' > t_{\text{disp}} \end{cases} \tag{3.3.8}$$

where $\langle\tau_V^{\text{res}}\rangle$ is the average V-band optical depth of the whole galaxy (computed using Eqn. 3.3.1) and $t_{\text{disp}} = 10$ Myr is the dispersion time for the stellar birth cloud. Hence, if a star particle is younger than the dispersal time of the stellar birth cloud then all star particles satisfying this criteria will have the same additional optical depth value. Again, the optical depth needs to be converted to the attenuation, here we assume a simple uniform dust

[†] Since we are only interested in the dust attenuation for galaxies as a whole, dust attenuation values for individual star particles are not as important.

screen such that the solution for the radiative transfer equation takes the following form:

$$\begin{aligned} A_V^{\rm unres} &= -2.5\log(e^{-\tau_V^{\rm unres}}) \\ &= 1.086\,\tau_V^{\rm unres}. \end{aligned} \tag{3.3.9}$$

The dust attenuation at other wavelengths is estimated using a simple power law relation from Charlot & Fall (2000) for unresolved dust:

$$A^{\rm unres}(\lambda) = A_V^{\rm unres}\left(\frac{\lambda}{\lambda_V}\right)^{-0.7}. \tag{3.3.10}$$

Combining the resolved and unresolved dust then gives the total magnitude correction, in any filter, such that:

$$M^{\rm dust} = M^{\rm dust\text{-}free} + A^{\rm res}(\lambda) + A^{\rm unres}(\lambda). \tag{3.3.11}$$

We show the high redshift M_{UV}-stellar mass relation of simulated galaxies from the EAGLE-Ref run in the left column of Fig. 3.1 after applying dust attenuation, and compare them with the results of Vogelsberger et al. (2020) from IllustrisTNG, as well as observations from Song et al. (2016). Song et al. (2016) analysed data from the *Hubble Space Telescope* which included $\sim$ 7000 galaxies selected using photometric redshifts in the range $z = 3.5 - 8.5$; further details may be found in Song et al. (2016, and references therein). Grey points are individual galaxies and the orange curve with error bars shows the median stellar mass and the $[16^{th} - 84^{th}]$ percentiles at fixed magnitude. We only show results for redshifts z =4, 6 and 8, for which data from Song et al. (2016) are available. Our results are in excellent agreement with those of Vogelsberger et al. (2020, model 'C') which is a more comprehensive and computationally expensive dust model using the radiative transfer method SKIRT (Baes et al., 2011; Camps et al., 2013; Saftly et al., 2014; Camps & Baes, 2015). SKIRT tracks the dust scattering and absorption randomly selected photon packets until they eventually arrive at a "detector". This process yields integrated fluxes specific to each simulated galaxy. Subsequently, Vogelsberger et al. (2020) computed the rest-frame magnitudes for various wavelength bands by convolving the fluxes with the corresponding SEDPY transmission functions. A brief description of their methods are as follows:

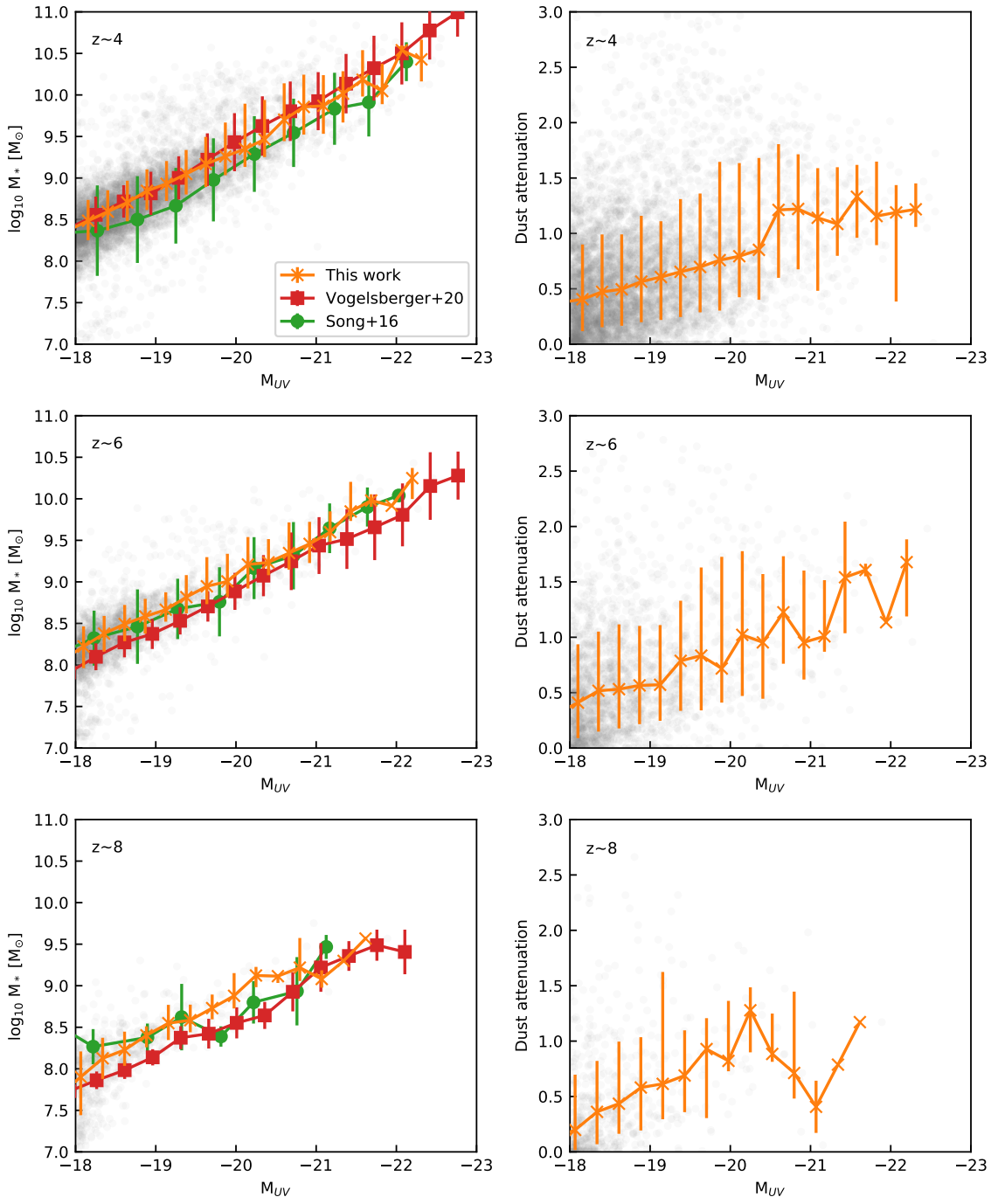

Figure 3.1

Left column: Stellar mass versus dust-corrected rest-frame UV magnitude at redshifts $z = 4, 6, 8$, with grey scatter points corresponding to individual galaxies from EAGLE-Ref and the orange line showing median and $[16^{th} - 84^{th}]$ percentile at a fixed $M_{\rm UV}$. The green connected circles and red connected squares show the results from the full radiative dust model in Vogelsberger et al. (2020), and observations from Song et al. (2016), respectively. *Right column*: Dust attenuation as a function of magnitude at redshifts $z = 4, 6, 8$, for galaxies in EAGLE-Ref. Our analytic dust model produces comparable results to SKIRT and observations.

- Produce stellar SEDs from the TNG stellar particles using FSPS.
- Construct a wavelength grid for the emitted photons.
- Provide SKIRT with the smoothing length values for the stellar particles in a given galaxy.
- Provide SKIRT with the gas density and metallicity of each of the Voroni gas cells in the simulation for dust calculations.
- Calculate the galaxy magnitude by placing a "detector" 1 Mpc away.

Our dust model uses additional information from the particles in the simulation (unlike simple empirical models) and shows quantitatively similar results to the full radiative dust model (SKIRT). This is very reassuring that they show such excellent agreement. EAGLE galaxies are also consistent with observational data within the scatter. The right column of Fig. 3.1 shows the dust attenuation as a function of M_{UV} for redshifts z =4, 6 and 8, indicating that our dust attenuation increases by approximately $\sim$ 1 mag as M_{UV} magnitude changes from -18 to -22, this result is consistent with Yung et al. (2019). This is due to brighter (more massive) galaxies having a larger amount of (cold) gas. We also compared our dust-corrected magnitudes with those of Trayford et al. (2015) who calculated the dust-free and dust-corrected SDSS apparent magnitudes for EAGLE-Ref galaxies using SKIRT (SKIRT was run on EAGLE using a similar method as described above for IllustrisTNG) at $z = 0.1$. Our results are consistent with theirs in the mass range $M_* > 1 \times 10^9\,M_\odot$.

3.3.3 Luminosity functions

Luminosity functions give the comoving number density of galaxies at a given luminosity; they are typically represented by a Schechter function (Schechter, 1976) with the following form in magnitude space,

$$\phi(m) = \frac{0.4\ln(10)\phi^*}{10^{0.4(m-m^*)(\alpha^*+1)}}\exp(-10^{-0.4(m-m^*)}), \tag{3.3.12}$$

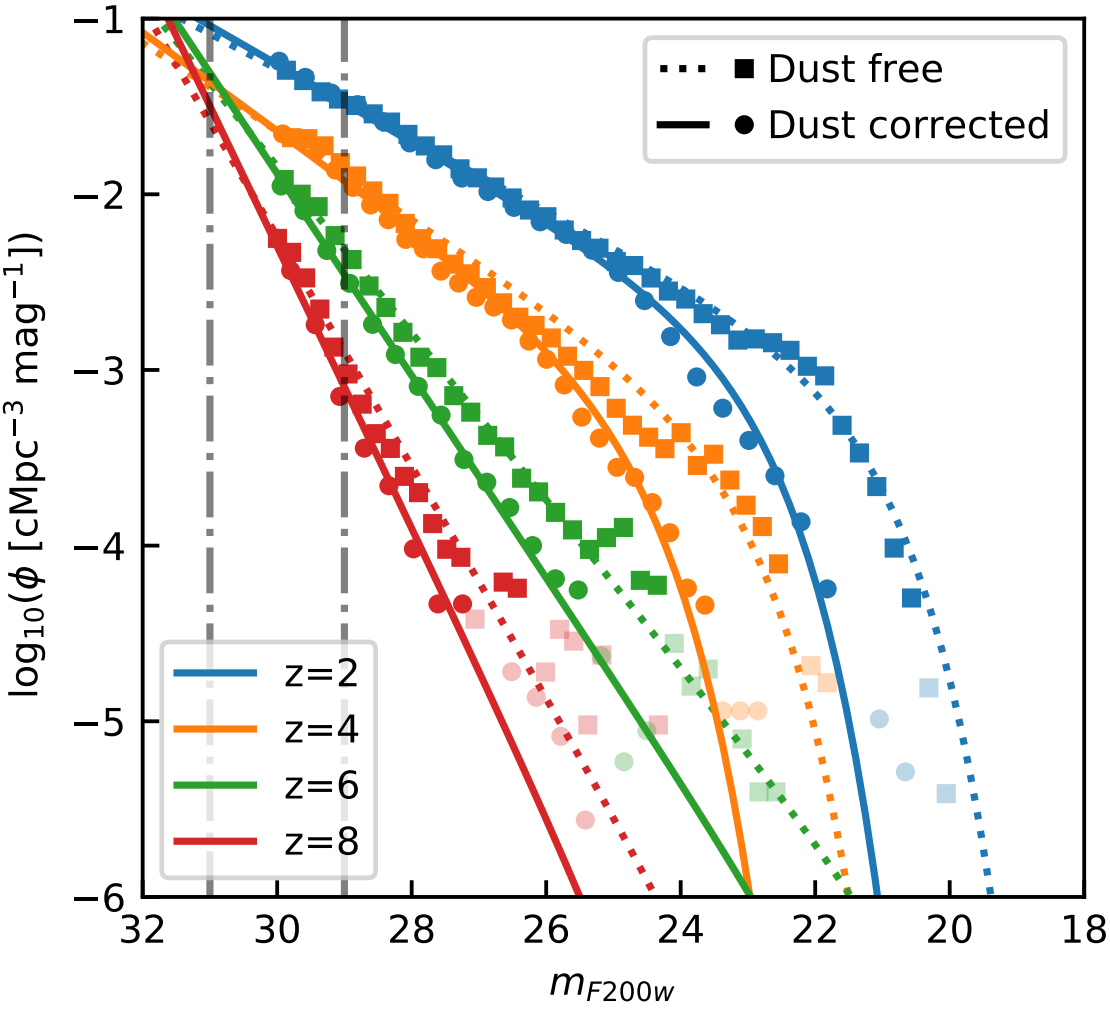

Figure 3.2

Luminosity functions of galaxies in the EAGLE-Ref simulation at different redshifts in the *JWST*/NIRCam F200W passband. The dust-free and dust-corrected luminosity functions are shown as square and circular points, respectively, with their corresponding Schechter fits as dotted and solid lines. Different redshifts are highlighted with different colours, as shown in the legend. Open faded symbols at the brighter end highlight bins with fewer than 10 galaxies per bin. The vertical dashed-dotted lines at limiting magnitudes of $m_{\rm lim} = 29$ and 31 mag correspond to the faintest magnitudes that are observable with exposure times of $T_{\rm exp} = 10^4$s and 10^5s, respectively.

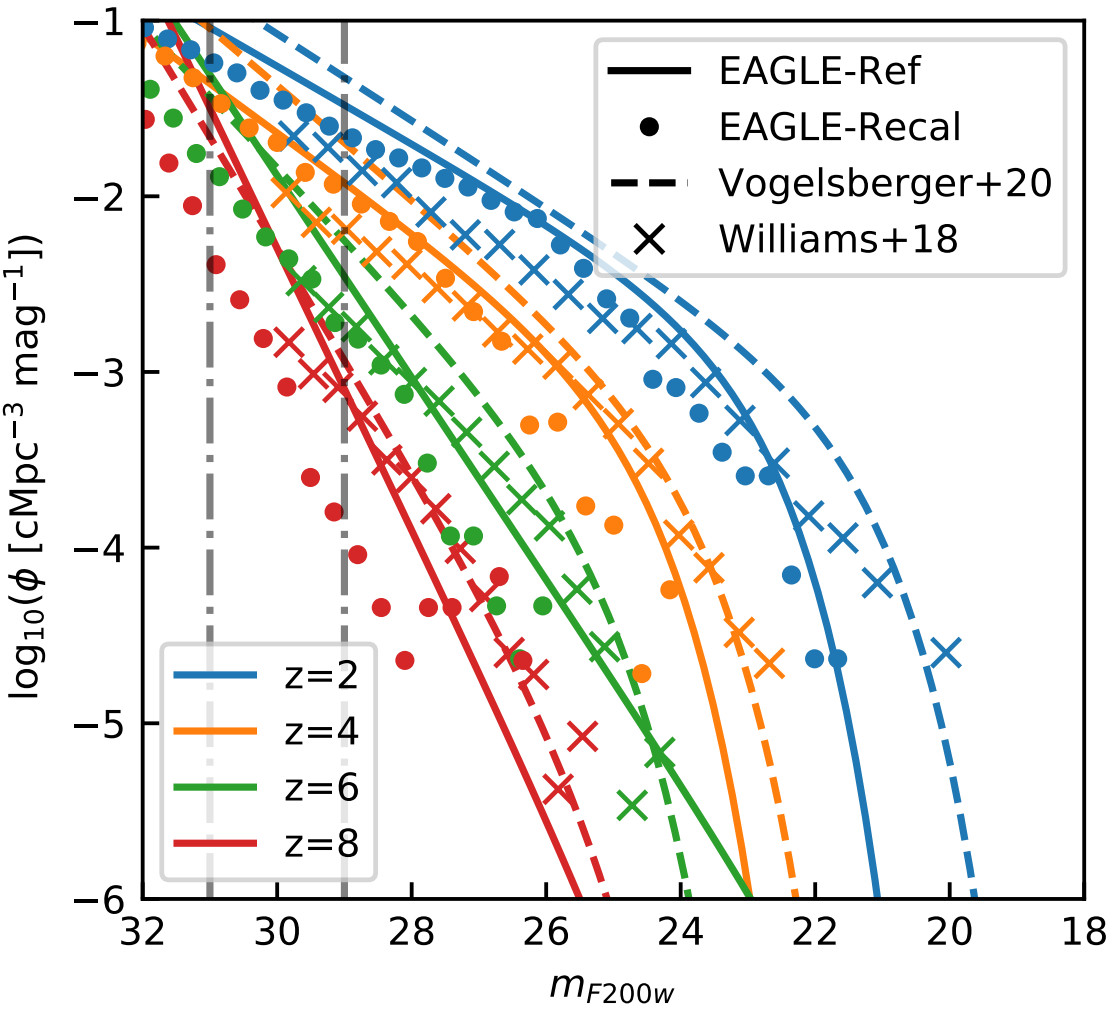

Figure 3.3

Dust-corrected luminosity functions for the *JWST*/NIRCam F200W passband for redshifts $z = 2,\ 4,\ 6,\ 8$. Solid lines correspond to the Schechter fits for EAGLE-Ref luminosity functions (same as Fig. 3.2), whereas circles of the same colour show the higher resolution EAGLE-Recal luminosity functions. For comparison, the dashed lines represent the luminosity functions from the Illustris-TNG simulations, computed using radiative transfer dust model and presented in Vogelsberger et al. (2020). Crosses show the luminosity functions derived from the JAGUAR mock catalogue for *JWST* (Williams et al., 2018). The vertical dashed-dotted lines are the same as in Fig. 3.2.

Table 3.2
The best-fit Schechter parameters for the *JWST* F200W passband at redshifts $z = 2, 4, 6, 8$.

Redshift	ϕ^* [cMpc^{-3} mag^{-1}]	m* [mag]	α^*
2	0.0018	23.09	-1.55
4	0.00091	24.83	-1.70
6	1×10^{-7}	21.03	-2.44
8	1×10^{-7}	24.06	-2.99

where ϕ^* is the normalisation, M* is the transition magnitude, and α^* is the faint-end slope parameter.

Fig. 3.2 shows the comoving luminosity function of the simulated galaxies before and after dust correction, and the corresponding Schechter fits in the *JWST* F200W passband. The best-fit parameters for the Schechter function were calculated using a χ^2 method for magnitudes brighter than 30, with Poisson uncertainties (the best-fit parameters for the *JWST* F200W passband are presented in Table 3.2).

Fig. 3.2 shows that including dust affects the bright end of the luminosity function more than the faint end. This is expected according to the right column of Fig. 3.1. Moreover, Fig. 3.2 shows that the dust has a larger impact at lower redshifts. This is expected since the average metallicity of galaxies is higher at lower redshifts due to past star formation.

Fig. 3.3 shows the dust-corrected luminosity function of the EAGLE galaxies at two resolution levels, alongside the results of Illustris-TNG (Vogelsberger et al., 2020). The solid line corresponds to a Schechter fit to galaxies in the EAGLE-Ref simulation (repeated from Fig. 3.2); points show the higher resolution results from EAGLE-Recal. Small differences between the luminosity functions, EAGLE-Ref and EAGLE-Recal, are expected, as the two models have slightly different parameters (see, Schaye et al., 2015, for comparison of stellar mass functions at $z = 0$). Our results, however, indicate that the low mass end slope of our Schechter fit is not significantly affected by the lower resolution of the EAGLE-Ref run for redshifts $z < 4$. At higher redshifts, $z = 6, 8$, the differences between EAGLE-Ref

and EAGLE-Recal become larger but these differences are still consistent within Poisson uncertainties (see e.g. Fig. 3.4). The increasing difference between EAGLE-Ref and EAGLE-Recal is due to the slight differences in the parameters of subgrid models (see Schaye et al., 2015, for more information).

The dashed lines in Fig. 3.3 show the outcome of model C, a full radiative transfer dust approximation using SKIRT presented by Vogelsberger et al. (2020). Despite the good agreement of the $\mathrm{M}_* - M_{\mathrm{UV}}$ relation between our results and those of Vogelsberger et al. (2020), especially at $z < 5$, shown in Fig. 3.1, there are notable differences in the luminosity functions. This implies that the difference is mainly coming from the differences in the stellar mass functions, or equivalently stellar mass-halo mass relations, between the two sets of simulations. The largest difference is seen at the brighter end and at lower redshift, so it is likely due to the differences in AGN models and feedback. We note that Vogelsberger et al. (2020) used a combination of IllustrisTNG volumes; the largest one (TNG-300) is $\approx 30\times$ larger than the EAGLE-Ref volume and therefore better samples the bright end of the luminosity function. We show bins with fewer than 10 galaxies as faint points in Fig. 3.2. The crosses in Fig. 3.3 show the luminosity functions derived from JADES Extragalactic Ultra-deep Artificial Realization (JAGUAR; Williams et al., 2018). The foundations of the JAGUAR mock catalogue were constructed using observations from Tomczak et al. (2014) and extrapolated to match the UV luminosity functions in Oesch et al. (2013); Bouwens et al. (2015, 2016); Calvi et al. (2016); Stefanon et al. (2017); Oesch et al. (2018). The luminosity functions from JAGUAR agree well with our results, however, the luminosity functions are flatter throughout. Thus, the EAGLE simulations might underestimate the number of bright galaxies and overestimate the number of faint galaxies which could be observed with *JWST*/NIRCam. The flattening of the faint end slope in the Williams et al. (2018) data is more pronounced at higher redshifts. This could be a result of the increasing difference in α^* values in the Schechter functions. Our α^* is consistent with Bouwens et al. (2015) at $z = 4$ who estimate the slope for the UV luminosity function to be -1.67 ± 0.05; however, at redshift $z \sim 8$ their slope is at least $\Delta\alpha^* \sim 0.9$ flatter.

3.3.4 Number of galaxies in *JWST*/NIRCam field-of-view

Our predictions for the luminosity function of galaxies can be used to estimate the number of galaxies observable within a *JWST*/NIRCam field-of-view (FoV). We need to integrate the Schechter fits, as in Eqn. 3.3.13, above the observable magnitude limit:

$$\begin{aligned}\phi_{\rm cum}(< m_{\rm lim}) &= \int_{L_{\rm lim}}^{\infty} \phi(L) dL \\ &= \phi^* \Gamma_{\rm inc}(\alpha^* + 1, 10^{-0.4(m_{\rm lim} - m_*)}),\end{aligned} \tag{3.3.13}$$

where α^*, ϕ^* and m^* are the parameters of the Schechter function, and $\Gamma_{\rm inc}(a, z) = \int_z^{\infty} t^{a-1} e^{-t} dt$ is the upper incomplete gamma function; $m_{\rm lim}$ represents the magnitude limit which depends on the exposure time and signal-to-noise ratio (SNR). The limiting magnitudes used correspond to exposure times of $T = 10^4$s and $T = 10^5$s with $SNR = 10$ and 5 respectively; these result in $m_{\rm lim} = 29, 31$. $m_{\rm lim}$ ~29 corresponds to the expected limiting magnitude for the JADES-M survey.

Finally, the following relation can be used to compute the expected number of galaxies per unit redshift in the *JWST*/NIRCam FoV:

$$\frac{{\rm d}N_{\rm exp}}{{\rm d}z} = \phi_{\rm cum}(< m_{\rm lim}) \frac{{\rm d}V_{\rm com}}{{\rm d}\Omega {\rm d}z}(z) \Delta\Omega, \tag{3.3.14}$$

where ${\rm d}V_{\rm com}/{\rm d}\Omega{\rm d}z$ is the differential comoving volume element described in Eqn. 3.3.15 and $\Delta\Omega$ is the solid angle produced by the *JWST*/NIRCam FoV (2.2×2.2 arcmin).

$$\frac{{\rm d}V_{\rm com}}{{\rm d}\Omega {\rm d}z}(z) = \frac{c(1+z)^2 d_A(z)^2}{H_0 E(z)} \tag{3.3.15}$$

where d_A is the angular diameter distance and $H(z) = H_0 E(z)$ is the Hubble parameter at redshift z.

Fig. 3.4 shows our predictions for the observable number of galaxies per unit redshift in the *JWST*/NIRCam FoV for magnitude limits of $m_{\rm lim} = 29$ and 31 (corresponding to the detection limits for exposure times of $T = 10^4$s and $T = 10^5$s, and $SNR = 10$ and 5 respectively). The error bars represent the Poisson error on each value.

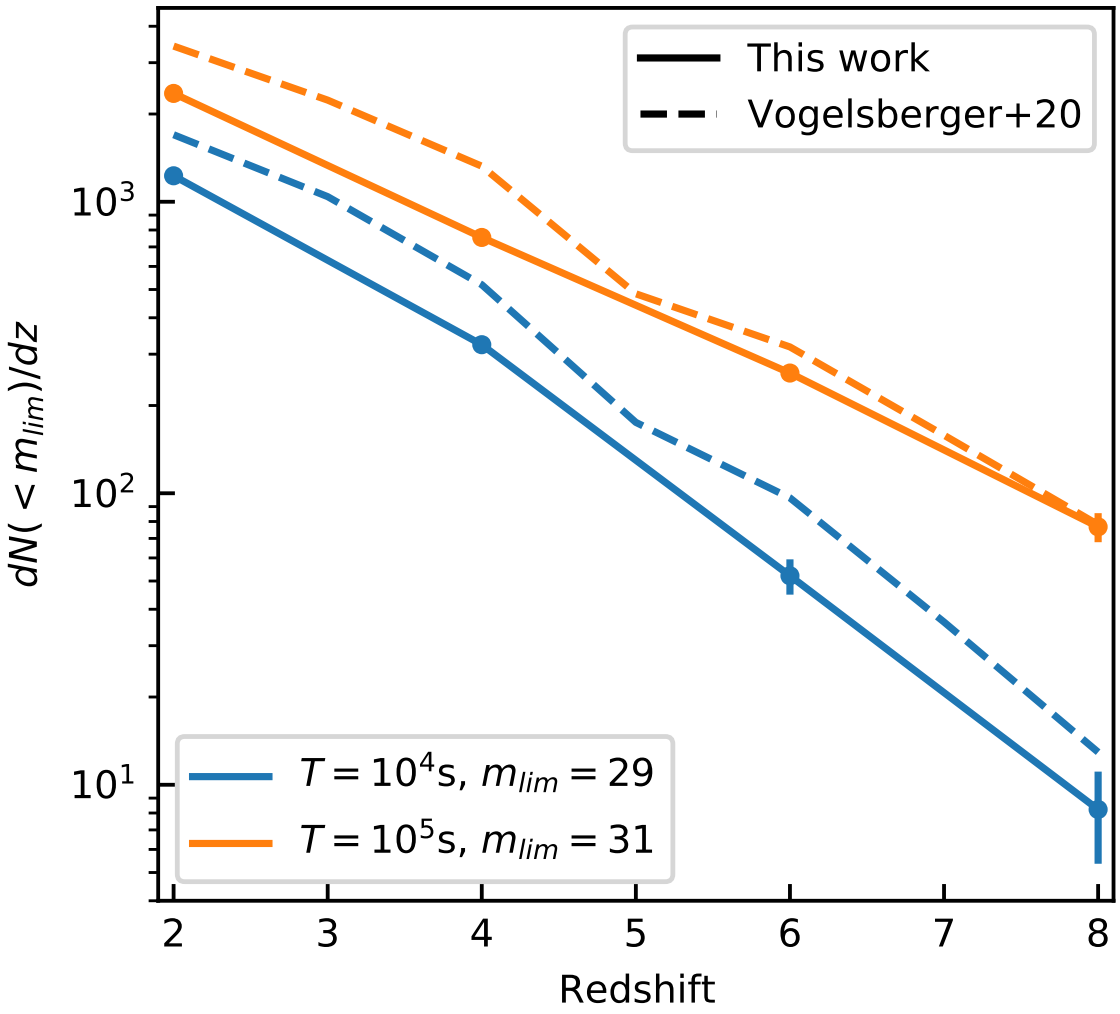

Figure 3.4

The expected number of galaxies as a function of redshift, in a *JWST*/NIRCam FoV (2.2×2.2 arcmin) that are above the detection limit with exposure times of $T = 10^4$s and $T = 10^5$s, and $SNR = 10$ and 5 respectively. These exposure times translate to limiting magnitude of $m_{\rm lim} = 29$ and 31, respectively. The solid and dashed lines correspond to our EAGLE-Ref results, and those of Vogelsberger et al. (2020), respectively. Error bars show the Poisson error on each value.

Fig. 3.4 indicates that our expected number of galaxies is lower than those predicted in Vogelsberger et al. (2020), by roughly $N = 500(1000)$ at $z = 2$ for the $T = 10^4$s ($T = 10^5$s) exposure time. This is due to the systematically higher offset in the luminosity function of Vogelsberger et al. (2020) compared to EAGLE at all magnitudes at $z = 2$, as seen in Fig. 3.3. The same statement is true at redshift $z = 4$; however, this differs for the luminosity functions at redshifts $z = 6 - 8$ primarily between magnitudes 29 and 31 (vertical dashed dotted lines), thus only affecting our expected number of galaxies for an exposure time of $T = 10^5$s (shown in orange; corresponding to limiting magnitude of 31). Our expected number of galaxies for $T = 10^5$s becomes much closer to the predictions of Vogelsberger et al. (2020) at high redshift which are only lower by $N \sim 60(1)$ at $z = 6$ ($z = 8$). We note that these differences are mainly driven by the faint end since the number of galaxies is dominated by galaxies in this regime. We also found that our predicted numbers of galaxies are consistent with Cowley et al. (2018), who used semi-analytic modelling techniques.

3.4 Progenitors of MW, LMC and GES

In this section, we focus on progenitors of MW analogues that could be observed by *JWST*. All the magnitudes and colours shown in this section include dust attenuation. Our definition of MW-, LMC- and GES-like galaxies, as well as MW analogues, are summarised in section 3.2.1.

Fig. 3.5 shows the evolution of dust-corrected F200W apparent magnitude as a function of redshift for the MW-like, LMC-like and GES-like galaxies. Points are coloured according to their stellar mass as shown in the colour bar, and the lines show the median magnitudes at any given redshift. At lower redshifts $z < 2$, we show the magnitudes of progenitors, calculated directly from the EAGLE-Ref run. At $z > 2$, where stellar masses become smaller and resolution effects become important, we correct the magnitudes statistically using the stellar mass of the progenitors and the higher resolution EAGLE-Recal run. Details can be found in Appendix B. We apply the correction only at $z > 2$ and for progenitors with $M_* < 10^8\,\mathrm{M}_\odot$, which is where our calculated magnitudes show a large

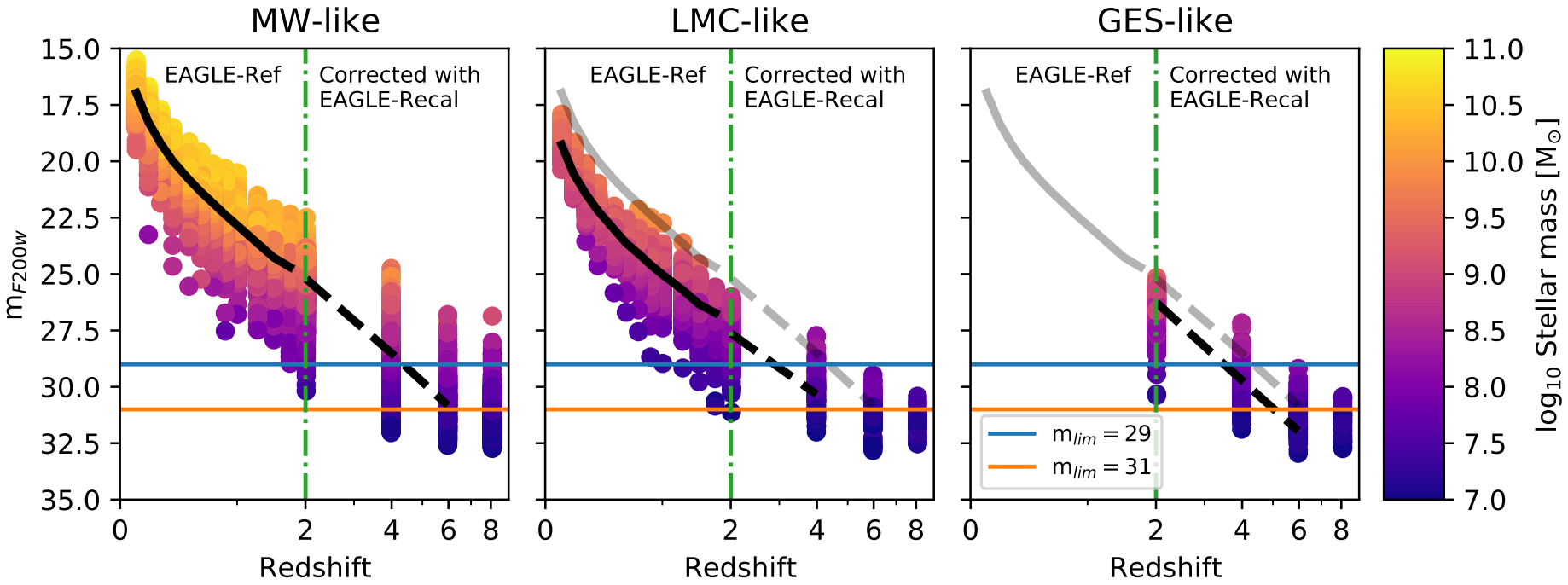

Figure 3.5

The apparent magnitude in the F200W passband as a function of redshift for progenitors of MW-like galaxies (*left*), the LMC-like satellites (*middle*) and GES-like galaxies (*right*) selected from the EAGLE-ref simulations. The points in each panel are coloured by the stellar mass, in logarithmic scale, of the galaxies as shown in the colour bar. Points to the left of the vertical dash-dotted line ($z = 2$) are magnitudes computed directly from EAGLE-Ref outputs, whereas magnitudes to the right of the line have been corrected using the $M_* - m_{\mathrm{F200W}}$ relation of the higher resolution EAGLE-Recal simulation (see Appendix B for details). The solid black lines in each panel show the median apparent magnitude at each redshift up until the boundary at $z = 2$, beyond which it turns into dashed indicating the transition to corrected magnitudes. The median line for the MW-like galaxies is repeated, as grey, in the middle and right panel for reference. The two horizontal lines in blue and orange show the magnitude limits for exposure times of 10^4s and 10^5s respectively with a $SNR = 10$ and 5, respectively.

scatter at fixed stellar mass in the EAGLE-Ref run, due to the limited resolution of the simulation. The median lines turn from solid to dashed at $z > 2$ when magnitudes have been corrected, and the median line for the MW-like sample has been repeated in grey in the other two panels for reference.

As expected, the progenitors are typically fainter at earlier times, albeit with significant scatter, which increases towards higher redshift. This is particularly true for MW-like galaxies. For example, the median magnitude and the interquartile range for MW-like progenitors are $m_{\rm F200W} = 20.8 \pm 0.58$ at $z \sim 0.5$ and they change to 25.2 ± 0.84 at $z \sim 2$.

At redshifts higher than $z \sim 3$, the fainter end of the magnitudes approach a constant value of $m_{\rm F200W} \sim 33$ mag. This is not physical, and is due to the low mass progenitors not being identified by the halo-finder at early times. In these circumstances, we show the median assuming unidentified progenitors are all fainter than identified ones. We stop showing the median if more than 50 percent of the progenitors in the sample are unidentified.

The two horizontal lines shown in Fig. 3.5 indicate the same detection limit of *JWST*/NIRCam used in the previous section: exposure times of $T = 10^4$s and 10^5s, are shown as blue and orange, respectively. The median of MW-like progenitors is easily above the detection thresholds at $z < 4$. However, the large scatter causes the fainter progenitors to become undetectable from $z \sim 2$. LMC-like progenitors are on average fainter than the MW-like sample by only ~ 2 mag at most redshifts, and the two samples overlap significantly. The LMC-like sample is detectable on average to $z \sim 2.8$ for $T = 10^4$s with almost none detectable beyond $z > 4$. The redshifts when the median magnitudes reach detection thresholds are summarised in Table 3.3, for various *JWST*/NIRCam passbands. The maximum redshifts observable for the three galaxy samples are all in the F356W passband, $\sim 6, \sim 4, 5.3$ respectively. The passband with the lowest maximum redshift for the three types of galaxies is the F070W passband. F356W is likely to be the most sensitive passband because it has the best transparency whereas F070W is likely to be the worst because of the lower flux at the blue-end of the spectrum, as well as a lower transparency.

GES-like galaxies, by definition, merge with their host MW-like galaxy in the redshift range $z = 1 - 2$, and therefore no data are shown at $z < 2$ for their progenitors in the

Table 3.3
The redshifts above which average progenitors of MW-like, LMC-like & GES-like galaxies fall below the magnitude detection limit. Here we assume exposure times of 10^4s and 10^5s, with $SNR = 10$ and 5 respectively for each of the *JWST*/NIRCam photometric passbands.

	MW mass		LMC mass		GES mass	
	10^4s	10^5s	10^4s	10^5s	10^4s	10^5s
F070W	4.1	4.9	2.4	4.0	3.2	4.4
F090W	4.4	6.0	2.5	4.0	3.3	4.8
F115W	4.3	6.0	2.7	4.0	3.3	4.8
F150W	4.3	6.0	2.9	4.0	3.3	4.9
F200W	4.5	6.0	3.0	~ 4	3.5	5.0
F277W	4.5	6.0	3.0	~ 4	3.5	5.0
F356W	4.9	~ 6	3.4	~ 4	4.0	5.3
F444W	4.3	6.0	2.8	4.0	3.5	5.0

right hand panel of Fig. 3.5. Interestingly, the GES-like progenitor sample is only slightly fainter than the MW-like progenitors ($\sim$ 1.1 mag on average), and they are brighter than LMC progenitors. These results are shown in more detail for $z = 2$ in Fig. 3.6.

The first two panels of Fig. 3.6 show the magnitude (m_{F200W}) and stellar mass distributions of the MW-, LMC-, and GES-like progenitor samples at $z = 2$. We can see more clearly here that the progenitors of MW-like galaxies are, on average, brighter and more massive than progenitors of both LMC- and GES-like galaxies. In addition, GES-like galaxies are brighter than LMC-like galaxies with the medians differing by $\Delta(m) \sim 1.2$ and $\Delta(\log_{10}(M_*)) \sim 0.5$. The median magnitudes for progenitors of LMC-like galaxies at $z = 2$ are consistent with predictions made by Boylan-Kolchin et al. (2015) who estimate that the LMC would have had a dust-free absolute UV magnitude of -15.6$\pm^{0.8}_{0.6}$. Our dust free absolute M_{UV} for LMC-like galaxies at $z = 2$ is $M_{UV} \sim -15.7$. The distribution of masses and magnitudes for MW- and LMC-like progenitor galaxies have a greater spread than GES-like galaxies since the latter were constrained to have a mass between $M_* = 0.5 - 1 \times 10^9\,M_\odot$ around redshift 2 before infall. The third panel of Fig. 3.6 shows

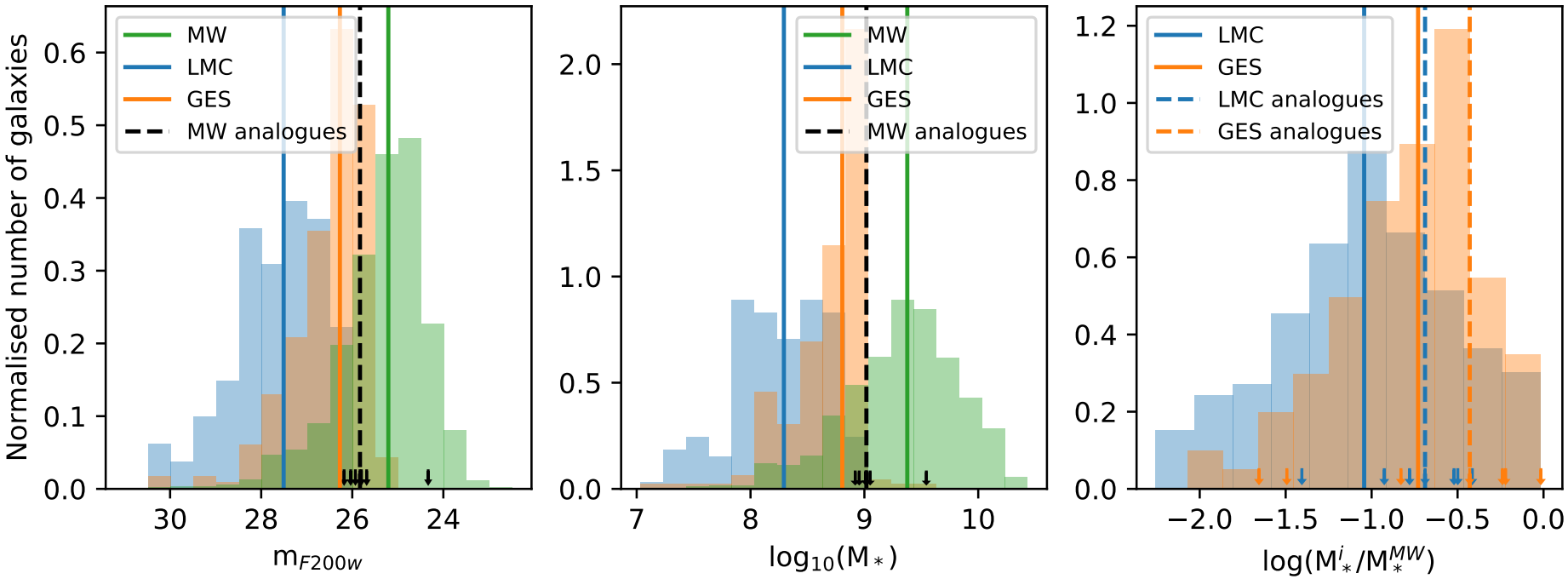

Figure 3.6

Comparison of the stellar masses and magnitudes of the progenitors of MW-, LMC-, and GES-like galaxies at $z = 2$. *Left*: magnitude distributions, in the F200W passband, for MW-, LMC- and GES-like galaxies are shown as green, blue and orange histograms, respectively. The medians of the distributions are marked with vertical solid lines of similar colour. The small black arrows along the x-axis show the magnitudes of the seven MW analogues (see text for details) and the vertical black dashed line correspond to their median. *Middle*: same as the left but for stellar mass distributions. *Right*: the stellar mass ratios of the progenitors of LMC- and GES-like galaxies relative to their MW host, shown as blue and orange histograms respectively. The solid lines of similar colour mark the median of the distributions. The small arrows along the x-axis and vertical dashed lines correspond to the LMC-like and GES-like objects associated to the seven MW analogues.

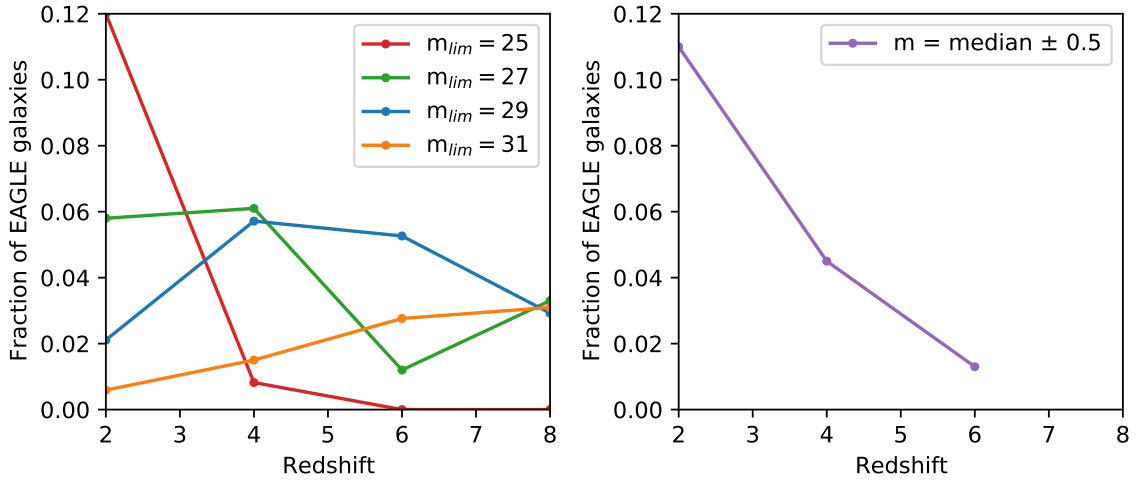

Figure 3.7

Left: the fraction of EAGLE-Ref galaxies above certain limiting magnitudes that are progenitors of MW-like galaxies, at different redshifts. The magnitude limits, in the F200W *JWST*/NIRCam passband, are shown in the legend: $m_{\rm lim} = 25, 27, 29, 31$ corresponding to red, green, blue and orange curves, respectively. **Right:** the fraction of galaxies in EAGLE-Ref that are progenitors of MW-like galaxies, and are observable and within a magnitude range corresponding to ±0.5 dex around the median apparent magnitude for F200W of Fig. 3.5, shown in purple.

the distribution of the stellar mass ratios between MW-like hosts and each of the LMC- and GES-like progenitor galaxies, all measured at $z = 2$. The ratio for GES-galaxies is higher than the ratio for LMC-galaxies by $\Delta(\log_{10}(M_*^i/M_*^{MW})) \sim 0.3$.

In all panels of Fig. 3.6, the dashed vertical lines represent the median for the MW analogue galaxies, with individual galaxies shown as small arrows along the x-axis. The left two panels suggest that the progenitors of MW analogues are more similar in magnitude and stellar mass to the progenitors of GES-like galaxies than the MW-like sample as a whole. The right panel shows that the mass ratios of LMC and GES components of the MW analogue progenitor systems are higher. This is due to the lower stellar mass of the MW analogue itself which is lower than the average MW-like galaxy at higher redshift, as shown in Chapter 2 (Evans et al., 2020).

Not only is it important to know how far back in time the MW progenitors could be observed, but also to know *how likely* is it that they will be observed. The left panel of Fig. 3.7 shows the fraction of observable ($m < m_{\rm lim}$) EAGLE-Ref galaxies that are progenitors of MW-like galaxies, as a function of redshift. We consider four limiting magnitudes (m_{F200W}),

$m_{\rm lim} = 25, 27, 29, 31$, shown in red, green, blue and orange respectively. At low redshifts we find $\sim$ 12% of galaxies brighter than $m_{F200W} = 25$ to be progenitors of MW-like galaxies. However, this percentage drops to just $\sim$ 1% when including all galaxies above $m_{F200W} = 31$. At high redshift ($z > 6$), there are no longer any galaxies massive/bright enough to have a magnitude brighter than $m_{F200W} = 25$. At $z \sim 8$, the fainter limiting magnitudes ($m_{\rm lim} = 27, 29, 31$) have the highest fraction of MW progenitors; $\sim$ 4% of galaxies are likely to be progenitors of MW-like galaxies.

These trends are readily understood. At high redshifts, galaxies are less massive and therefore fainter. Thus it is extremely unlikely to be as bright as 25 mag. The opposite is true for the faintest limiting magnitude ($m_{\rm lim} = 31$) which shows an increase in the fraction with redshift. Due to the steep mass function the abundances of faint galaxies, at $z = 2$, is large and the fraction that are MW progenitors is consequently low; by redshift $z = 8$ those low mass galaxies have dropped below this limiting magnitude and the MW progenitors become more prominent.

The fractions of galaxies in each bin shown in the left panel of Fig. 3.7 vary considerably with redshift. In the right panel of Fig. 3.7 we use a fixed magnitude range around the median of MW-like progenitors (shown in the left panel of Fig. 3.5). These ranges correspond to $\pm$0.5 dex around the median magnitude for MW-like progenitors at each redshift, shown in purple. The magnitude range in this panel has its highest fraction ($\sim$ 11%) at redshift $z = 2$ and its lowest ($\sim$ 1%) at redshift $z = 6$. The fractions in this panel end at redshift $z = 6$ since beyond this time more than 50 percent of the progenitors are unidentified (as in Fig. 3.5). At high redshifts ($z = 6$) it is clear that there are many galaxies with a similar magnitude as the MW-like progenitors that do not become MW-like galaxies by the present. The key difference between these galaxies and the progenitors of MW-like galaxies is simply that they either merge with their host galaxy (similar to a GES type merger event) or become satellites (similar to the LMC).

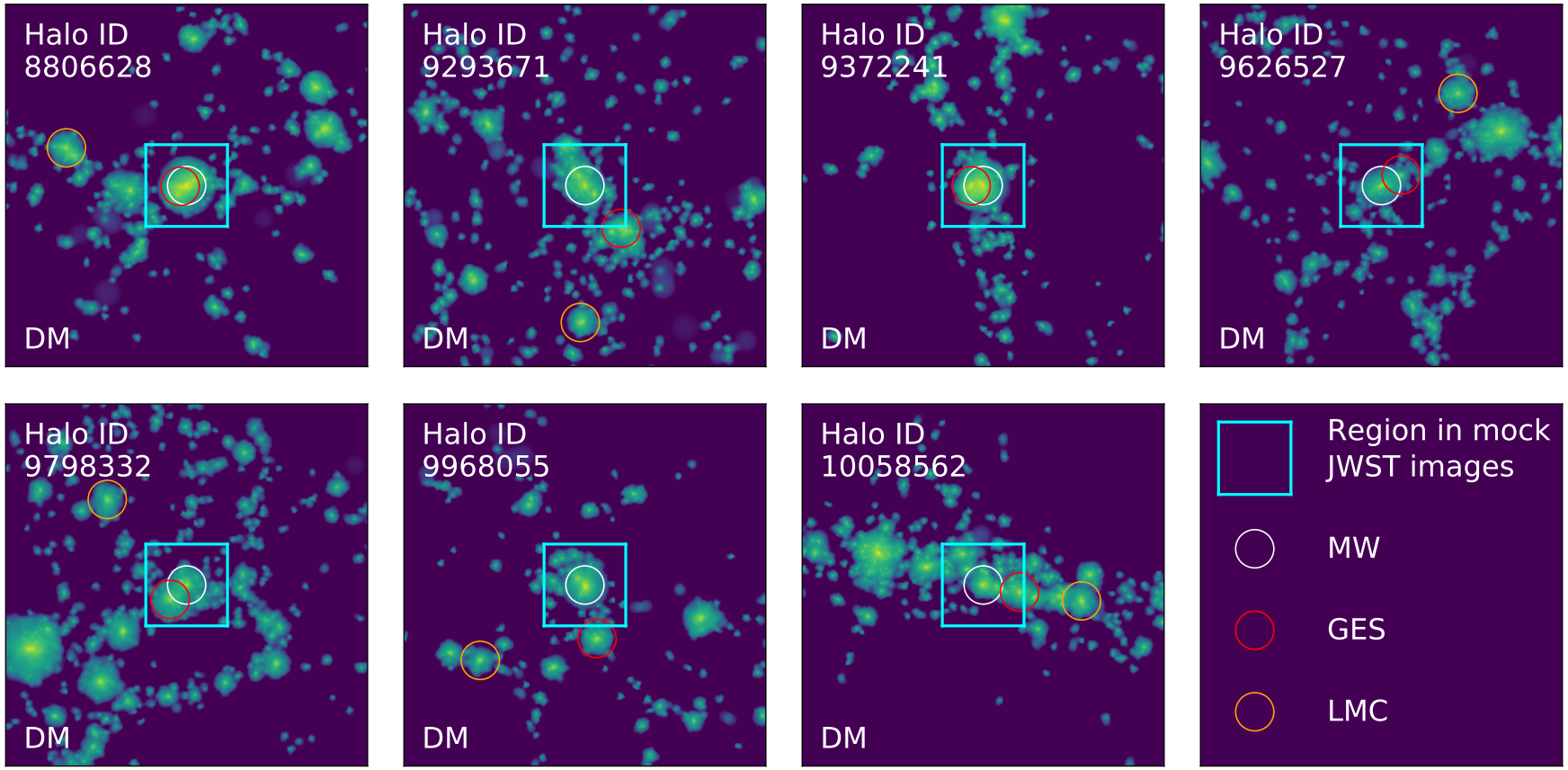

Figure 3.8

Dark matter distribution around seven MW analogues with a GES and LMC (see text for details), shown at redshift $z = 2$. Each panel shows a random projection of particles within a radius of 0.8 Mpc centred on the main progenitor of the MW analogue, which is marked with a white circle. Red and orange circles represent the positions of the centre of the GES and LMC progenitors, respectively. Image panels have side length of ∼1.13 Mpc, the size of the *JWST*/NIRCam FoV (2.2 × 2.2 arcmin) at $z = 2$. The cyan square in each panel indicates the region size for the mock images in Fig. 3.10. Smoothed particle images were made using PY-SPHVIEWER (Benitez-Llambay, 2015).

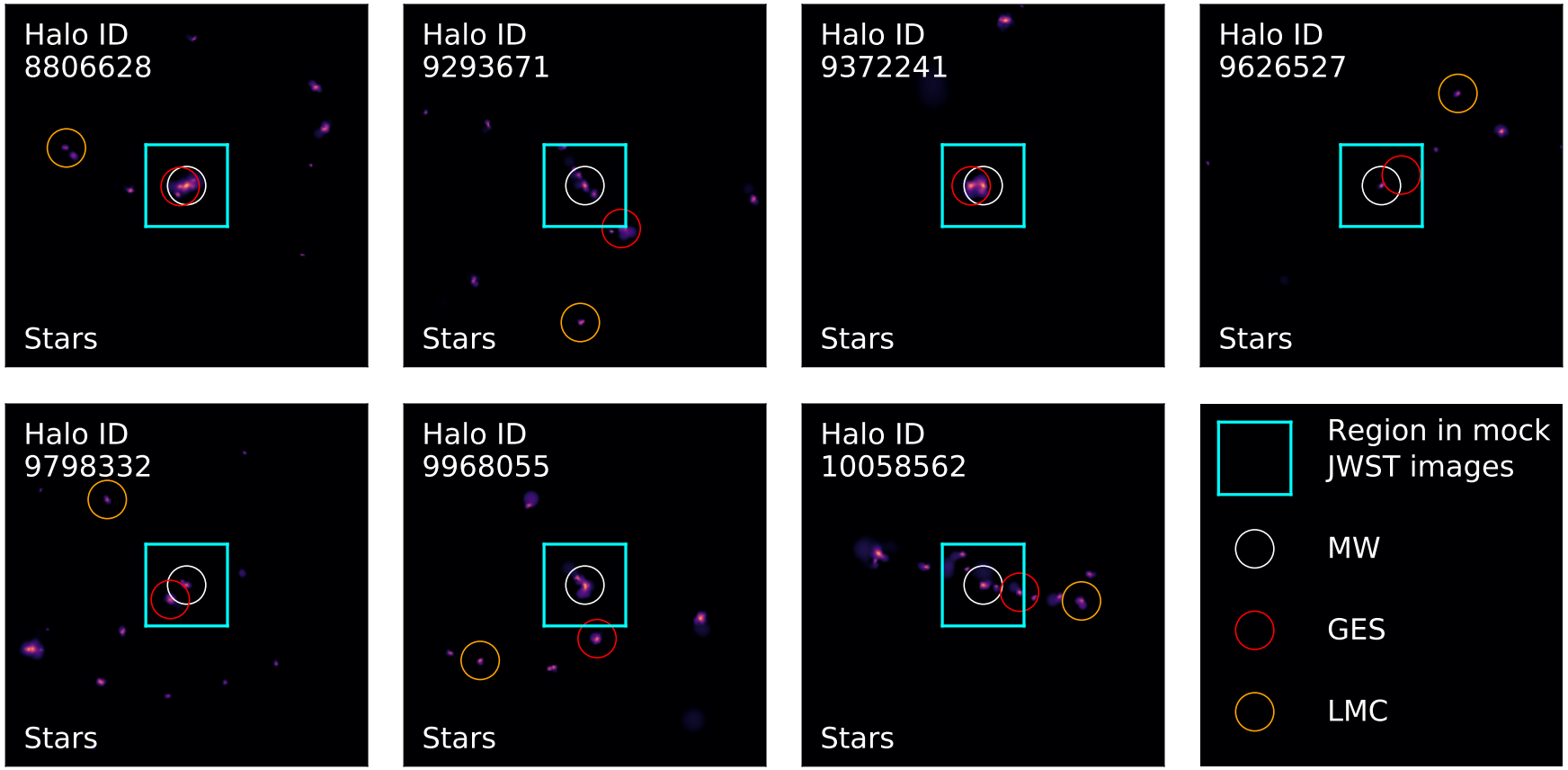

Figure 3.9
Same as Fig. 3.8 but for star particles in the same region.

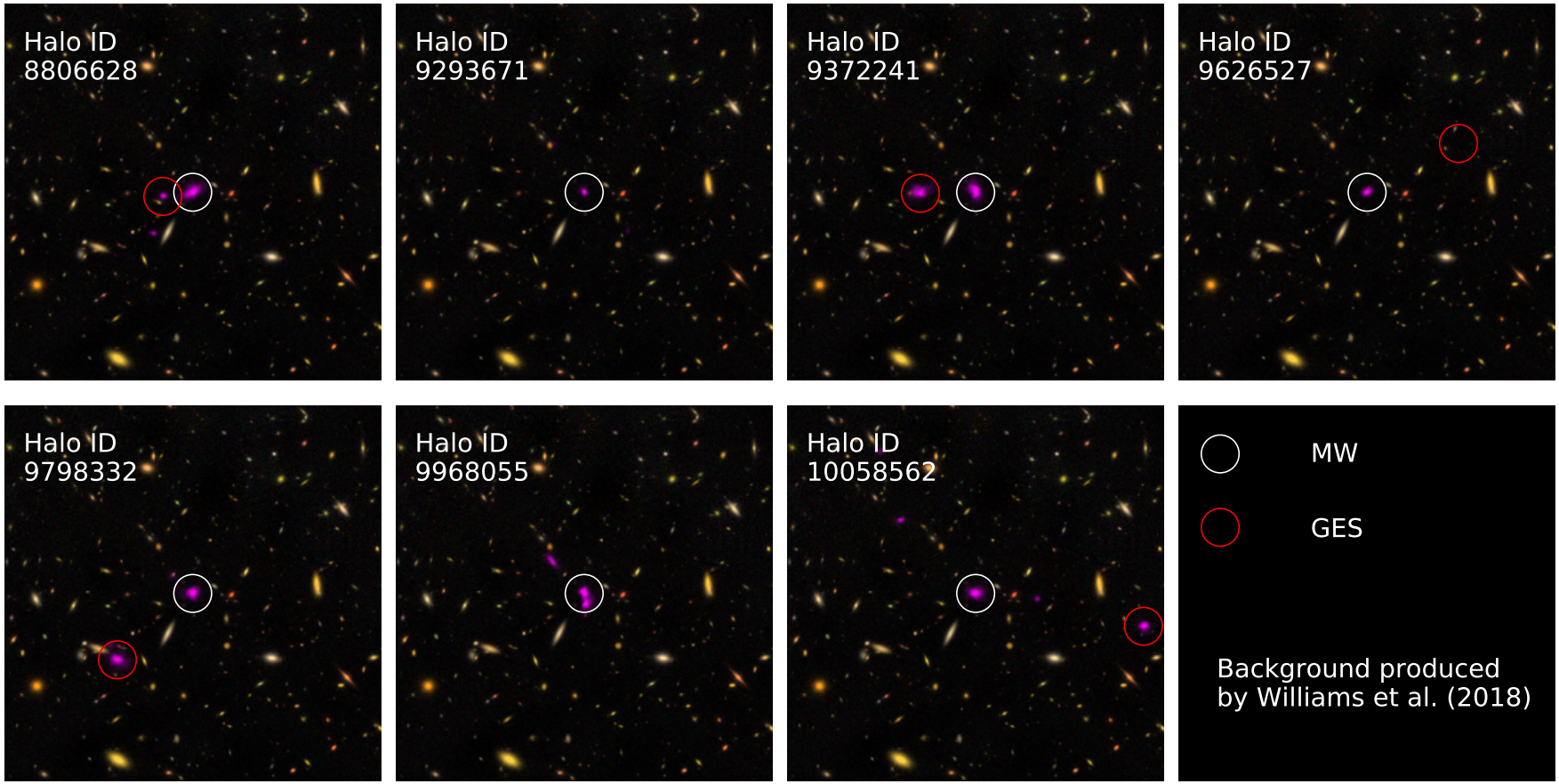

Figure 3.10

Mock *JWST* images of MW analogue systems, each panel shows a 30 arcsec × 30 arcsec FoV. Stars in the MW analogue systems are shown in pink to emphasise their particle locations, this is not representative of their observed colour. The background of these images were produced by Williams et al. (2018) to illustrate the *JWST* view of the GOODS-S field. The MW and GES galaxies are highlighted using white and red circles, respectively.

3.4.1 MW progenitors with realistic accretion histories

In this section we focus on the small sample of seven MW analogues with the additional constraints on the accretion history, namely having a GES-like merger and a LMC satellite. See Section 3.2 and Chapter 2 for details. The dark matter and star particles around these MW analogues at $z = 2$ are shown in Figs. 3.8 and 3.9, respectively. The main progenitor of the MW-like object is positioned at the centre of each image and is marked with a white circle. LMC and GES progenitors are also marked with orange and red circles, respectively. Each panel has a side length of ∼1.13 Mpc which corresponds to the size of the FoV of *JWST*/NIRCam (2.2 × 2.2 arcmin) at redshift $z = 2$[‡]. These two figures were made using PY-SPHVIEWER (Benitez-Llambay, 2015), with 64 of the nearest neighbours used for calculating the SPH smoothing length.

GES progenitors are close to the MW progenitors at this redshift. This is expected as they are constrained to merge with the main progenitor at $z = 1 - 2$. Interestingly, all of LMC progenitors are well within the *JWST*/NIRCam FoV size. We will elaborate on the distance of LMC and GES progenitors at various redshifts below.

The cyan squares in Fig. 3.8 and 3.9 mark the regions of these systems that have been illustrated in the mock *JWST* images shown in Fig. 3.10. These have been produced using a background mock image for *JWST*/NIRCam of the GOODS-S field (from Williams et al., 2018) on to which the images of our MW-analogues have been overlaid. Due to the small, faint nature of our simulated galaxies, they have been assigned a pink colour for easy identification in the image. *These colours are not illustrative of real life observations.* This figure shows that without redshift information and potentially other constraints, identifying the progenitors of the MW and its building blocks amongst all the foreground and background galaxies will be very difficult.

To further investigate the proximity of the LMC and GES progenitors to the MW progenitor at various redshift, their angular and physical separations are shown in Fig. 3.11. The left panel shows the median and $[16^{th} - 84^{th}]$ percentile of the angular separation between

[‡]Note these are not light cones, rather particles at a fixed redshift (fixed snapshot) of the simulation.

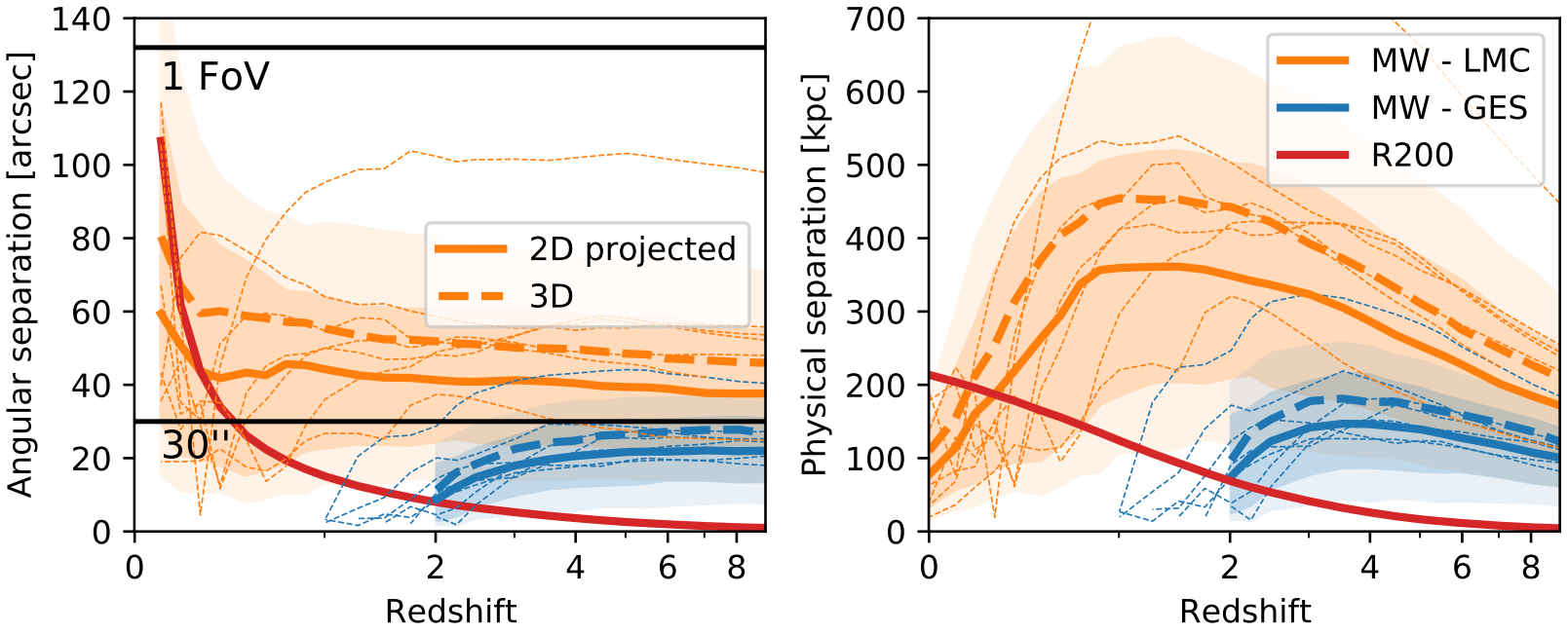

Figure 3.11

Left: Angular separation of LMC-like (orange) and GES-like galaxies (blue) from their host, i.e. the progenitors of MW-like galaxies, as a function of redshift. The thick solid lines and the shaded regions of corresponding colour represent the median, $[16^{th} - 84^{th}]$ and $[5^{th} - 95^{th}]$ percentile ranges of projected separations for the LMC-like and GES-like groups, whereas the thick dashed lines show the median 3D separations for these groups. Thin dashed lines correspond to 3D separations for the MW analogues group (and their LMC- and GES-like accretions). Since GES is defined as merging between redshifts $z = 1 - 2$, the separations are only shown until redshift $z = 2$. Both the LMC- and GES-like galaxies fit within the same *JWST* FoV as their host, i.e. separation < 2.2 arcmin. *Right*: Similar to the left panel but for (proper) physical separation. The red lines in both panels show the median R_{200} of MW-like galaxies as a function of redshift. The projected separations are based on the average along three orthogonal axes.

progenitors of the MW- and LMC-like galaxies, as well as of the MW- and GES-like ones. Angular separations are based on the average of three orthogonal projections. We additionally include individual lines for the subsample of 7 MW analogues (and the corresponding LMC and GES) where we show the maximum separation (i.e. 3D distance).

The left panel in Fig. 3.11 shows that both the LMC and GES progenitors fall within the *JWST*/NIRCam FoV (120 arcsec) at all times, with GES progenitors being invariably closer to the MW than the LMC progenitors. Individual galaxies are shown as fine dashed lines for the seven MW analogues. Note that one of the LMC satellites is much further away so is not visible in the "Halo ID 9372241" panel in Fig. 3.8. The separations between MW- and GES-like progenitor galaxies end at redshifts $z = 2$ since this is where some GES galaxies start to merge with their host galaxies and the median is no longer representative of the whole sample. The angular resolution limit of *JWST*/NIRCam of 0.07 arcsec (at 2 microns) indicates that all GES progenitors can be resolved from their MW progenitor companion.

The right panel of Fig. 3.11 is similar to the left panel but shows the physical separation. The turnaround time and infall time of the objects are easier to see here. The R_{200} evolution of a MW analogue is shown with a red curve in both panels for reference. LMC-like satellites have a recent infall time, $z \sim 0.3$, consistent with previous works (e.g. Boylan-Kolchin et al., 2011a; Rocha et al., 2012). Such massive satellites are affected by dynamical friction to a large degree and they merge quickly with the host; hence those surviving at redshift at $z = 0$ must have fallen recently (e.g Fattahi et al., 2020). The turnaround redshift and radius of the LMC sample are on average $z \sim 1.5$ and $r = 360 \pm 160$kpc, respectively. GES analogues have a smaller turnaround radius ($r = 150 \pm 60$kpc) and earlier accretion times ($z \sim 3.5$), compared to LMC progenitors. This is expected since GES are constrained to merge with the MW progenitors by $z = 1$.

Combining the results from Fig. 3.5 and Table 3.3, we conclude that MW-like progenitor galaxies should be observable up until $z \sim 6$ in most *JWST*/NIRCam passbands, with associated LMC- and GES-like galaxies observable until redshifts $z \gtrsim 4$ and 5.3 respectively. At these times the LMC- and GES-like galaxies will most likely be within the

JWST/NIRCam FoV.

Combining the results from the previous sections we can also make predictions for the number of MW analogues with LMC & GES that would be observable at high redshifts ($z = 8$). Using the results in Fig. 3.7 (with a limiting magnitude of $m_{lim} = 29$; shown in blue) along with the results from Chapter 2 that 0.65% of MW-like galaxies would have an LMC-like satellite and GES-like merger, 0.02% of galaxies in any given FoV should be a MW analogue with a realistic accretion history. Therefore, on average, we would need to have 50 JWST/NIRCam exposures to image one MW analogue (or the equivalent of ~ 240 arcmin^2).

3.4.1.1 Colour-magnitude diagrams

We now consider whether or not progenitors of the MW, LMC and GES are distinguishable from other galaxies at the same redshift. We turn to the colour-magnitude diagrams (CMDs) for another layer of information. Fig. 3.12 shows the CMD for the progenitor in the F115W vs. F115W-F200W plane at $z = 2$. These passbands were chosen at random since at $z = 2$ there was minimal differences between CMDs.

We show all MW-like galaxies, and the individual components of the seven MW analogues (MW, LMC and GES) in various panels in Fig. 3.12 from top left to lower right, respectively. The background shows a grey-scale density distribution for the overall colour-magnitude distribution of the total population of galaxies in the EAGLE-Recal run which has higher resolution. At fainter magnitudes we see individual 'ridges' that are likely caused by resolution effects. Similarly to the approach used for Fig. 3.5, we do not use the magnitudes (and colours) directly from the EAGLE-Ref run for our target galaxies, especially because the LMC and GES progenitors at high redshifts have relatively low stellar mass. Instead, we highlight with red contours the location where galaxies with similar stellar masses to our target galaxies lie on the CMD.

The top left panel of Fig. 3.12 shows that the progenitors of MW-like galaxies are among the brightest galaxies at $z = 2$ with magnitudes brighter than $m_{\mathrm{F115W}} \sim 26$. However, MW

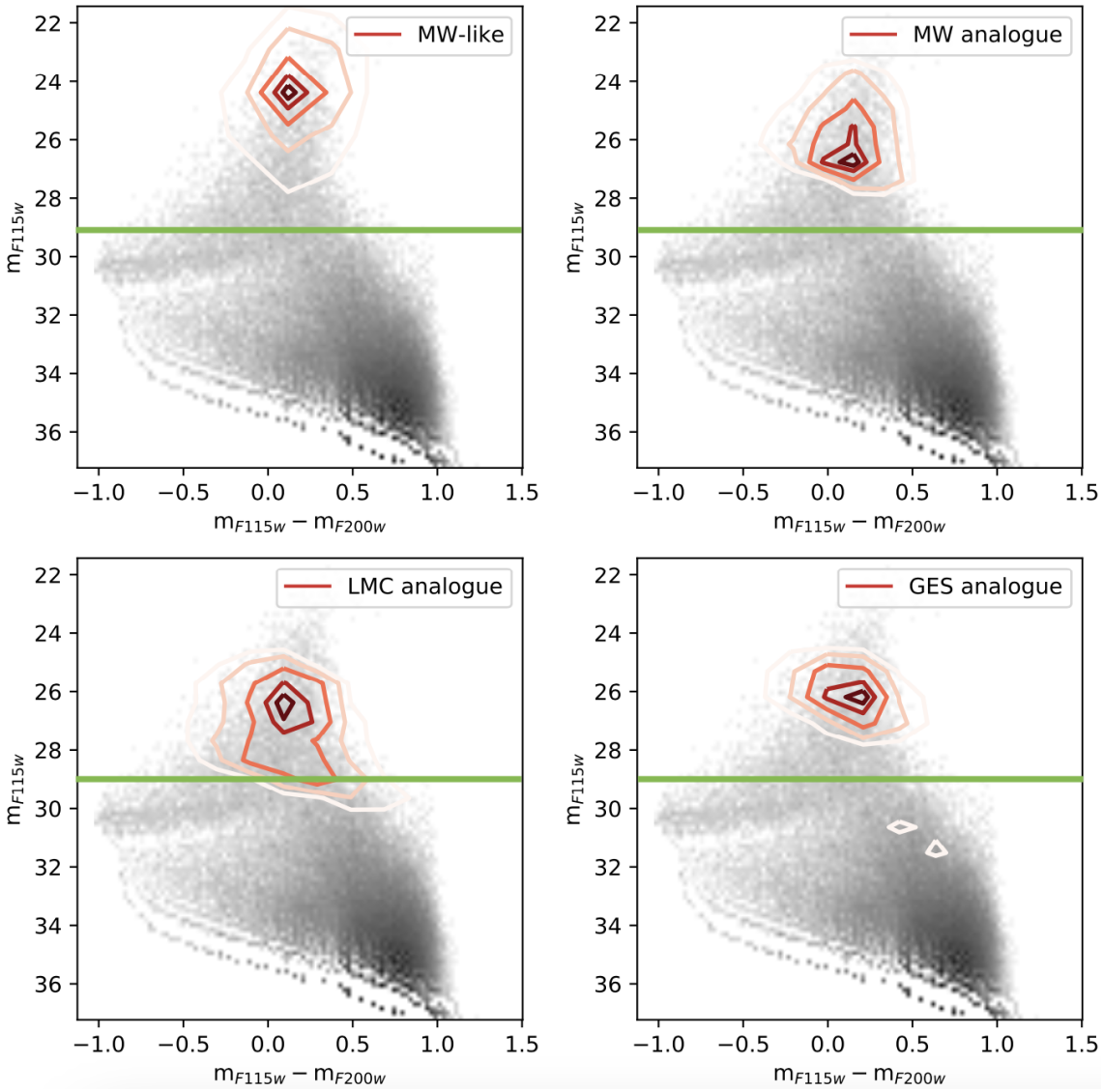

Figure 3.12

The CMDs for galaxies in the F115W and F200W passbands at redshift $z = 2$. The grey-scale background shows the colour-magnitude distribution for all galaxies in EAGLE-Recal; the red contours represent the area of the colour-magnitude diagram that 10, 25, 50, 75 and 90 percent of the progenitors of MW-like, MW analogues and their LMC and GES components would be contained in the upper left to lower right panels, respectively. The mass distribution of MW-like galaxies is quite broad, which causes a large spread in magnitudes. The green horizontal line represents the limiting magnitude for $T = 10^4$s exposure time and $SNR = 10$.

analogues (top-right panel) lie at the lower magnitude ranges for all MW-like galaxies. This is consistent with the stellar mass evolution shown in Chapter 2 (Fig. 2.5) where MW analogues have a much lower mass than typical MW-like galaxies. The MW, LMC and GES analogues all lie within a similar space in the colour-magnitude diagram, with a greater range in colour space than magnitude space. They tend to have magnitudes around 26 and colour between -0.5 and 0.5, in these passbands.

We include a similar figure but for CMDs at redshift $z = 4, 6$ and 8 in Appendix B.0.1. In summary, the results discussed above hold at those redshifts too. We note that at $z = 6$ and 8, some combination of colours in *JWST*/NIRCam passbands will not yield useful CMDs, as some passbands are in the Lyman-break, as shown in Appendix B.0.2. More precisely, F070W at $z = 6$ is bluer than the Lyman-break, and both F070W and F090W are bluer by $z = 8$.

3.5 Discussion and Conclusions

We provide predictions for *JWST* using cosmological hydrodynamical simulations from the EAGLE project Schaye et al. (2015). We have calculated dust-free magnitudes in *JWST*/NIRCam bands for all galaxies, and then applied a simple-analytic dust correction using the ISM column density and temperature along the line-of-sight (based a modified version of Dust Model B from Vogelsberger et al., 2020). The dust-corrected magnitudes were used to produce comoving galaxy luminosity functions at redshifts $z = 2 - 8$ along with the estimated number of galaxies in a *JWST*/NIRCam FoV across the same redshift range. In the second half of this chapter we focused on MW analogues and the main accreted objects onto them, namely LMC- and GES-like objects, as identified in Chapter 2 (Evans et al., 2020), to see how far back in time their progenitors might be observable, and if it might be possible to identify them in a *JWST*/NIRCam FoV. Our main conclusions are as follows:

- We compare our results with those from Vogelsberger et al. (2020) which is based on Illustris-TNG, and a more sophisticated treatment of dust attenuation using radiative

transfer code, SKIRT. We find excellent agreement between the two results when comparing M_* vs. dust-corrected magnitudes ($M_{\rm UV}$).

- Our luminosity functions are in overall agreement with those from Vogelsberger et al. (2020). Considering the previous point, the differences in the luminosity functions are likely caused by differences in the stellar mass functions of EAGLE and Illustris-TNG (see section 1.3.3 for a comparison), resulting from their different subgrid galaxy formation models. Our luminosity functions are also in good agreement with those produced from the JAGUAR mock catalogue for *JWST*(Williams et al., 2018), however, the JAGUAR luminosity functions are flatter at the bright end and hence our results may underestimate the number of bright galaxies observable with *JWST*/NIRCam.

- The best-fit parameters for the Schechter functions were used to predict the expected number counts of galaxies at each redshift. We expect a maximum of $\sim$ 2400 galaxies at redshift $z = 2$ and $\sim$ 80 at redshift $z = 8$ for an exposure time of 10^5s ($SNR = 5$). These numbers reduce to $\sim$ 1300 and $\sim$ 8 at those two redshifts, respectively, for exposure time of 10^4s ($SNR = 10$). These predictions are overall lower than the average numbers from Vogelsberger et al. (2020). This discrepancy does not affect the MW progenitor results because MW progenitor galaxies are among the fainter galaxy population. It would, however, affect the numbers predicted in a field of view, especially at redshift 8 since at this redshift, the counts are no longer dominated by the faint end for the 10^4s exposure. We found that our predicted numbers of galaxies are consistent with Cowley et al. (2018), who used the semi-analytic model of galaxy formation, Galform.

- Assuming an exposure time of 10^5s and $SNR = 5$, a MW-like progenitor galaxy would be observable with *JWST* up to redshift $z \sim 6$, whereas progenitors of LMC- and GES-like galaxies would be observable out to redshifts $z \sim 4$ and 5.3, respectively. The optimal passband is F356W and the least sensitive is F070W. In the F356W passband, *JWST* should be able to observe galaxies on average out to

$\Delta z = 1$ more than in the F070W passband. These limits reflect the fact the these passbands have the best and worst transparency respectively.

- The progenitors of the individual components of the MW analogue systems (MW, LMC, GES galaxies) have very similar stellar masses and magnitudes at high redshifts, with GES analogues being on average slightly more massive than the LMC analogues. The main difference in their fate lies in whether they become a host galaxy, satellite galaxy or if they merge with their host galaxy.

- The median magnitudes of progenitors of LMC-like galaxies at $z = 2$ is consistent with predictions made by Boylan-Kolchin et al. (2015) who estimate that the LMC would have had a dust-free absolute UV magnitude of -15.6$\pm^{0.8}_{0.6}$. Our dust free absolute M_{UV} for LMC-like galaxies at $z = 2$ is $M_{UV} \sim -15.7$.

- Our results suggest that the progenitors of the LMC- and GES-like galaxies always lie within 60 and 30 arcsec, respectively, of MW progenitors at all times and therefore will fit within one FoV of *JWST*/NIRCam.

- The CMDs of the progenitors of MW analogues also suggest that the three components (MW, LMC, GES) should lie in a similar colour-magnitude range. Galaxies of similar mass to the MW-, LMC- and GES-like galaxies in the MW analogue systems have a wide range of colours but a narrow range in magnitude.

In summary, our simulations indicate that it should be possible to observe progenitors of MW analogues using *JWST* and also observe the progenitors of their LMC-like satellites and GES-like companions at early times. Up until the redshift at which they are observable (typically $z = 4$), the three galaxies should all fall within the same FoV. At redshift $z = 2$ galaxies with similar mass and $m_{\mathrm{F115W}} \sim 26$ could be analogues to the MW/GES merger. This is an exciting opportunity to link the high redshift universe to our galaxy today.

In closing, we remark that our study can be extended and refined with future generations of simulations, which will provide larger volumes and/or finer resolution. The EAGLE-Ref simulations span 100Mpc^3 but, there are only 7 MW-analogues in this volume. Larger

simulations will allow for better statistics and hence firmer conclusions can be made for MW analogue galaxies. With better statistics we could also investigate MW-like systems within the Local Group environment (and hence provide comparisons with work such as Boylan-Kolchin et al., 2016; Santistevan et al., 2020). Finally, higher resolution simulations would allow us to calculate the surface brightness and size of low mass galaxies (which would allow for comparisons with work such as Patej & Loeb, 2015).

CHAPTER 4

Effect of environment on merger rates: cold vs warm dark matter

4.1 Introduction

The Λ cold dark matter (ΛCDM) model of the universe predicts that halos form and evolve through a sequence of hierarchical mergers (White & Rees, 1978; Davis et al., 1985). Mergers are often divided into two categories: minor and major. During a minor merger, a smaller satellite halo merges with a more massive host halo, while for a major merger, two similarly sized halos merge together. The boundary between a minor and major merger is typically a total mass ratio of 3:1 (e.g., Cole et al., 2000).

Minor and major mergers can have very different effects on the host halo. Minor mergers are a relatively common occurrence in the universe, and they can have a significant impact on the evolution of galaxies. Minor mergers contribute both stars and gas to their progenitor galaxy, leading to various effects such as thickening the galactic disc (Quinn et al., 1993; Velazquez & White, 1999; Brook et al., 2004; Bournaud et al., 2005; Kazantzidis et al., 2008; Villalobos & Helmi, 2008; Read et al., 2008; Purcell et al., 2009; Moster et al., 2010) and creating a diffuse stellar halo (Murante et al., 2004; Bullock & Johnston, 2005;

Bell et al., 2008; Murante et al., 2010). Recent work by Bustamante et al. (2018) found that minor mergers can also dilute the metallicity of galaxies. Major mergers cause more dramatic changes to a galaxy. For example, a major merger between two spiral galaxies could result in the creation of an elliptical galaxy (e.g., Toomre & Toomre, 1972; Toomre, 1977; Negroponte & White, 1983; Hernquist, 1992; Naab & Burkert, 2003; Cox et al., 2006). Major mergers can trigger star formation (e.g., Larson & Tinsley, 1978; Kennicutt et al., 1987; Barnes & Hernquist, 1991; Mihos & Hernquist, 1994; Barton Gillespie et al., 2003; Cox et al., 2008) and also prompt new activity in Active Galactic Nuclei (e.g., Sanders et al., 1988; Hernquist, 1989; Springel et al., 2005a; Hopkins et al., 2006; Johansson et al., 2009; Younger et al., 2009; Debuhr et al., 2010, 2011).

Previous theoretical studies of merger rates have made use of large-volume cosmological simulations based on ΛCDM. Fakhouri & Ma (2008) and Fakhouri et al. (2010) studied the merger and growth rates of Friends-of-Friends halos in the Millennium and Millennium-II simulations, respectively, which are cosmological simulations with box sizes of 500 Mpc/h and 100 Mpc/h (Springel et al., 2005b; Boylan-Kolchin et al., 2009). The goal of these studies was to quantify merger rates over a wide mass range. The authors found a universal merger rate of dark matter halos in the mass range $M = 10^{10} - 10^{15}\,\mathrm{M}_{\odot}$. Fakhouri & Ma (2009) investigated the effects of environment on the merger rates of halos in the Millennium simulation. They found that the number of mergers increases with halo mass and that the merger rate is higher for halos in denser environments. Hester & Tasitsiomi (2010) also used the Millennium simulations to investigate the rates of major mergers of subhalos in different environments, where the environment was considered in terms of the density of nearby subhalos in spherical shells. They found that for galaxy-mass dark matter halos, the merger rate decreases with increasing environment density. Gottlöber et al. (2001) showed, in high-resolution N-body simulations, that in cluster environments, galaxies undergo three times fewer major mergers in their lifetime compared to isolated galaxies. They also demonstrated that the merger rates increase with halo mass and that the merger rates of galaxies decrease with increasing environment density. These latter two studies (Hester & Tasitsiomi, 2010; Gottlöber et al., 2001) do not agree with the results

of Fakhouri & Ma (2008) and Fakhouri et al. (2010) due to their different definitions of a merger and of halo environment. Fakhouri & Ma (2008) and Fakhouri et al. (2010) study the mergers of FoF halos whereas Hester & Tasitsiomi (2010) and Gottlöber et al. (2001) study the mergers of individual subhalos. Halo environment in Fakhouri & Ma (2008) and Fakhouri et al. (2010) define environment using the particle densities whereas Hester & Tasitsiomi (2010) defines environment using the density of nearby subhalos.

The nature (or properties) of dark matter could have major implications for galaxy merger rates and properties. Merger rates are strongly related to the hierarchical nature of structure formation.Warm dark matter (WDM) aims to replicate the observed large-scale structure, as correctly predicted by cold dark matter (CDM), while also accounting for the small-scale properties where CDM fails. WDM particles, being warmer than CDM particles, possess higher thermal velocities. Consequently, these particles would stream through the early universe's initial perturbations, hindering the formation of smaller halos and leading to a cut-off in the matter power spectrum on relevant scales (e.g., Dodelson & Widrow, 1994; Bode et al., 2001; Zentner & Bullock, 2003; Benson et al., 2013). N-body simulations reveal significantly lower number counts of halos below $\sim 10^9\,M_\odot$ in WDM (e.g., Colín et al., 2000; Schneider et al., 2012; Lovell et al., 2014; Bose et al., 2016; Wang et al., 2017; Lovell et al., 2021). Therefore, the nature of dark matter can have significant consequences for the merger rates at low mass-scales.

Studying dwarf galaxies could provide one of the greatest insights into the nature of dark matter. Dwarf galaxies, are small, faint, and metal-poor, and are thus relatively difficult to study. Traditionally, mergers were considered less significant for dwarf galaxies as their growth was expected to be primarily driven by smooth accretion (Genel et al., 2010). However, recent observations are revealing evidence of mergers in dwarf galaxies, with studies detecting possible stellar halos around several of them, including Tucana II (Chiti et al., 2021), Ursa Minor (Sestito et al., 2023), Coma Berenices, Ursa Major I, and Boötes I (Waller et al., 2023), see also Longeard et al. (2022). Using N-body simulations, Deason et al. (2022) investigated the stellar halos of dwarf galaxies and found that dwarf galaxies experience more mergers in a CDM model of the universe than in WDM. While the impact

of WDM on dwarf galaxies is evident, the effect of the environment on their evolution remains unknown.

Understanding the merger rates of dwarf galaxies in both CDM and WDM paradigms is a promising way to constrain the nature of dark matter. In this chapter, we will investigate the merger rates of halos in the COCO simulation as a function of environment using both CDM and WDM. Our objective is to identify the most suitable environment for targeted observations of dwarf galaxies in upcoming surveys, aiming to further constrain the nature of dark matter. This chapter is structured as follows: in Section 4.2, we describe the COCO simulations and our environment definitions; in Section 4.3, we present our findings; and in Section 4.4, we provide our conclusions. Additionally, in Section 4.5, we outline the future work planned before submission to MNRAS.

4.2 Methods

In this section, we will discuss the details of the COCO simulations, our halo selection criteria, how we will be defining halo mergers, and, finally, our methods for defining the environment of halos.

4.2.1 Copernicus Complexio

We analyse the low mass halos in the *Copernicus Complexio* (COCO) suite of N-body simulations (Bose et al., 2016; Hellwing et al., 2016). COCO is a high-resolution dark matter-only zoom-in simulation, which was run using GADGET-3 (Springel, 2005)[§] from $z = 127$ to $z = 0$. The high-resolution region of COCO is roughly $(\sim 40\ \mathrm{Mpc})^3$ and has two versions. There is a CDM and WDM (with rest mass 3.3 keV) version of COCO, where each particle has mass $m_p = 1.6 \times 10^5\ \mathrm{M}_\odot$. The WDM model was compatible with the Lyman-α constraints (Viel et al., 2013), although it was the warmest particle allowed for the constraints at that time. The WDM model was also compatible with the coldest sterile

[§]The high resolution region is selected from the low resolution parent box Copernicus Complexio Low-Resolution simulation, COLOR (see Table 1 in Hellwing et al., 2016, for more details).

neutrino model for a dark matter particle (Lovell et al., 2016). Since these simulations were run in 2016, the constraints on the WDM particles have changed. The more recent constraints suggest that the WDM particle, in both a thermal relic model and a sterile neutrino model, should be colder. WDM masses lighter than 4.4 keV ruled out by Dekker et al. (2022) for a thermal WDM candidate. Dekker et al. (2022) also provide a lower limit on sterile neutrino mass of $m > 12$ keV. We will refer to the simulations as COCO-COLD and COCO-WARM. COCO assumes a cosmology derived from WMAP-7 (Komatsu et al., 2011), where the parameters are: $\Omega_m = 0.272$, $\Omega_\Lambda = 0.728$, $\Omega_b = 0.04455$, and $h = 0.704$, where $h = H_0/100$ km s^{-1}Mpc^{-1}, $n_s = 0.967$, and $\sigma_8 = 0.81$.

To identify the dark matter halos, the Friends-of-Friends (FoF) algorithm (Davis et al., 1985) was used with a linking length of 20 percent of the mean interparticle separation. The substructure and subhalos within the FoF halos were found using the SUBFIND algorithm (Springel, 2005). A minimum of 20 bound particles is required to identify a subhalo, which corresponds to a subhalo mass of $3.2 \times 10^6\,\mathrm{M}_\odot$. The masses of halos, M_{200}, are defined as the total mass of particles contained within a radius r_{200}, where r_{200} is the radius within which the mean density of the halo is 200 times the critical density of the Universe.

4.2.2 Halo selection

In this chapter, we focus on central halos in COCO with peak mass (peak mass is the maximum mass of a halo measured along the main branch of its merger tree, using this value instead of the current $z = 0$ mass allows us to include halos that have recently lost mass due to tidal stripping) in the following mass bins: $M_{\mathrm{peak}} = 10^9 - 10^{9.5}\,\mathrm{M}_\odot$, $M_{\mathrm{peak}} = 10^{9.5} - 10^{10}\,\mathrm{M}_\odot$, $M_{\mathrm{peak}} = 10^{10} - 10^{10.5}\,\mathrm{M}_\odot$, $M_{\mathrm{peak}} = 10^{10.5} - 10^{11}\,\mathrm{M}_\odot$ and $M_{\mathrm{peak}} = 10^{11} - 10^{12}\,\mathrm{M}_\odot$.

Table 4.1 shows the total number of halos in each category for COCO-COLD and COCO-WARM, as well as their basic properties. The table includes the number of selected halos and the median peak mass at $z = 0$ for each group. To more effectively compare our results with

Table 4.1
The number of subhalos in each of the mass ranges studied in this work along with their median peak mass for COCO-COLD and COCO-WARM.

Simulation	Mass range [$M_\odot$]	Number	Median M_{peak} [$M_\odot$]
COCO-COLD	10^9 – $10^{9.5}$	25025	1.54×10^9
	$10^{9.5}$ – 10^{10}	8704	4.84×10^9
	10^{10} – $10^{10.5}$	2907	1.54×10^{10}
	$10^{10.5}$ – 10^{11}	1068	4.86×10^{10}
	10^{11} – 10^{12}	464	1.81×10^{11}
COCO-WARM	10^9 – $10^{9.5}$	19513	1.59×10^9
	$10^{9.5}$ – 10^{10}	8037	4.90×10^9
	10^{10} – $10^{10.5}$	2950	1.54×10^{10}
	$10^{10.5}$ – 10^{11}	1091	4.86×10^{10}
	10^{11} – 10^{12}	484	1.76×10^{11}

previous studies, we increased the range for the highest mass bin to be double the width of the other bins. This was necessary because there are not many massive dark matter halos in the simulations due to its volume. We did not extend down to lower mass halos since we are interested in halo mergers. At higher redshifts, these halos would fall below the resolution limits of the simulations. It is possible to resolve minor mergers for the lowest mass bin back to redshift $z \sim 7$.

4.2.3 Merger definitions

The definition we use for mergers throughout this chapter is based on the subhalo merger trees. The merger trees are based on the Dhalo definition used in Jiang et al. (2014). This merger tree technique avoids "temporary mergers" due to any tenuous bridges of particles in the exteriors of halos. A merger occurs when the SUBFIND algorithm can no longer detect the merging halo and it is destroyed. However, the merger mass ratio is defined at a different time. For every merger identified by the merger trees, the halos are tracked back to the time when it was part of a different Dhalo to identify the time when it was most

recently a separate object i.e., before the merger process started, and their mass ratio is defined at this time. This method for identifying the merger ratio avoids the tidal stripping of the satellite and the accretion of the central, providing a more accurate ratio of the halo masses.

The merger mass ratio is given by $\zeta = M_{\rm halo}^{\rm Satellite,\ infall}/M_{\rm halo}^{\rm Central}$, where the central and satellite masses are defined as above. The mass ratio for major mergers is $\zeta > 0.3$, as is commonly used in the literature. The mass ratio for the minor mergers is $0.05 < \zeta \leq 0.3$. We have a lower bound on the mass ratio for minor mergers to limit the effects of resolution on our results.

4.2.4 Environment

In this chapter, we use two techniques to define the environment density of a halo in the coco simulation at redshift $z = 0$. These techniques probe different scales of environment, from global large scale structure to more local environments.

The first method uses the NEXUS cosmic web finder (Cautun et al., 2013), which is an improved version of the MultiScale Morphology Filter (Aragón-Calvo et al., 2007). NEXUS identifies the environment of halos and separates them into four categories: voids, walls, filaments, and clusters. NEXUS has been run on coco's parent simulation, COLOR, where coco sits at the centre. We use the same NEXUS output for the results shown in CDM and WDM, as the large-scale cosmic structure should be consistent between the dark matter models. A more detailed study of the environmental effect on halos from the NEXUS output for coco can be found in Hellwing et al. (2021). The background of Fig. 4.1 shows an example of the NEXUS output for coco. The different environments are shown as a colour scale from dark blue to yellow, where dark blue represents the void regions and yellow represents the cluster regions. The locations of the low mass halos ($M_{\rm peak} = 10^9 - 10^{10}\,{\rm M}_\odot$) in this slice are shown as pink points, and the massive halos ($M_{\rm peak} > 10^{12}\,{\rm M}_\odot$) are shown as purple stars. As expected, the locations of the halos tend to follow the cosmic web defined by NEXUS.

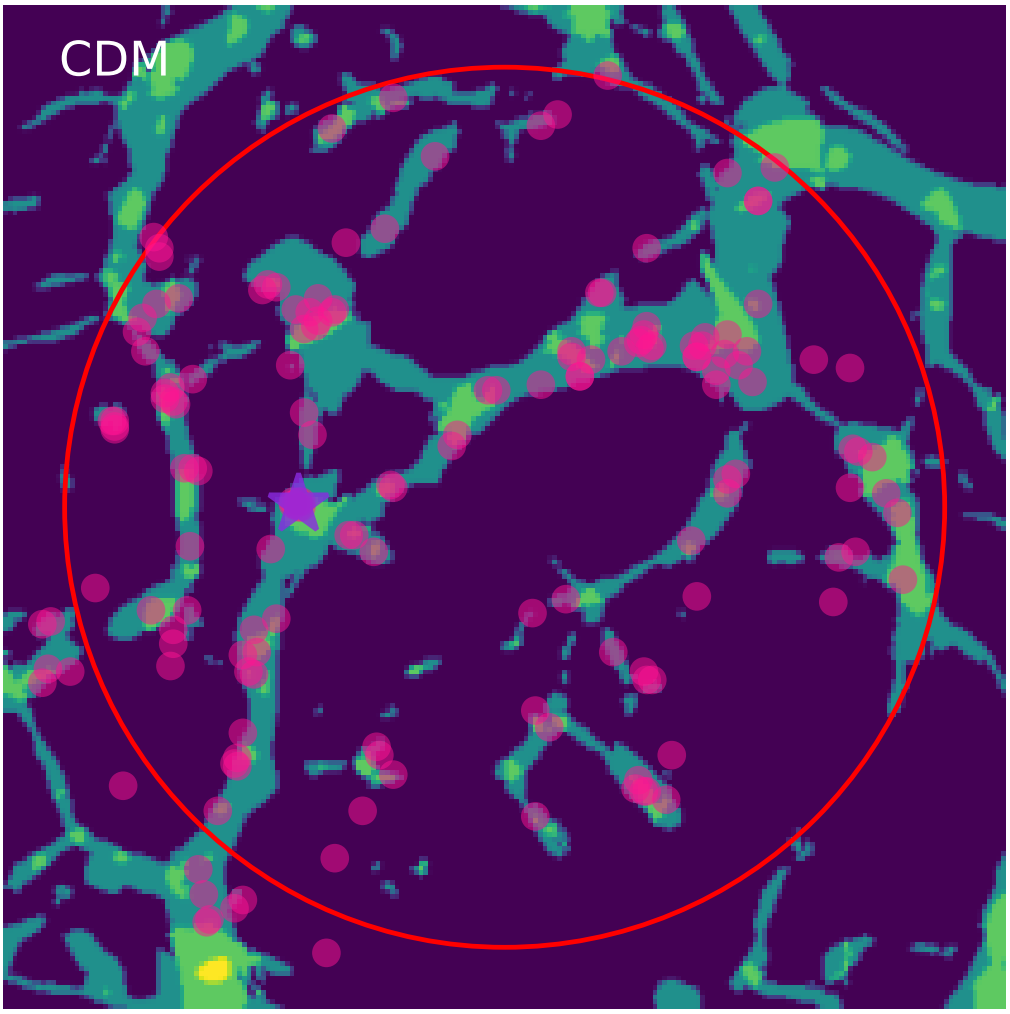

Figure 4.1
A central slice of coco showing the different NEXUS environments in the background (with a slice thickness of 0.11 Mpc). The background colours show void, wall, filament, and clusters on a colour scale from dark blue to yellow. Pink points represent the locations of dwarf halos (in the mass range $10^9 - 10^{10}\,M_\odot$). The purple star shows the location of a roughly Milky Way-sized halo in the simulation. The red circle shows the approximate area of the coco simulation.

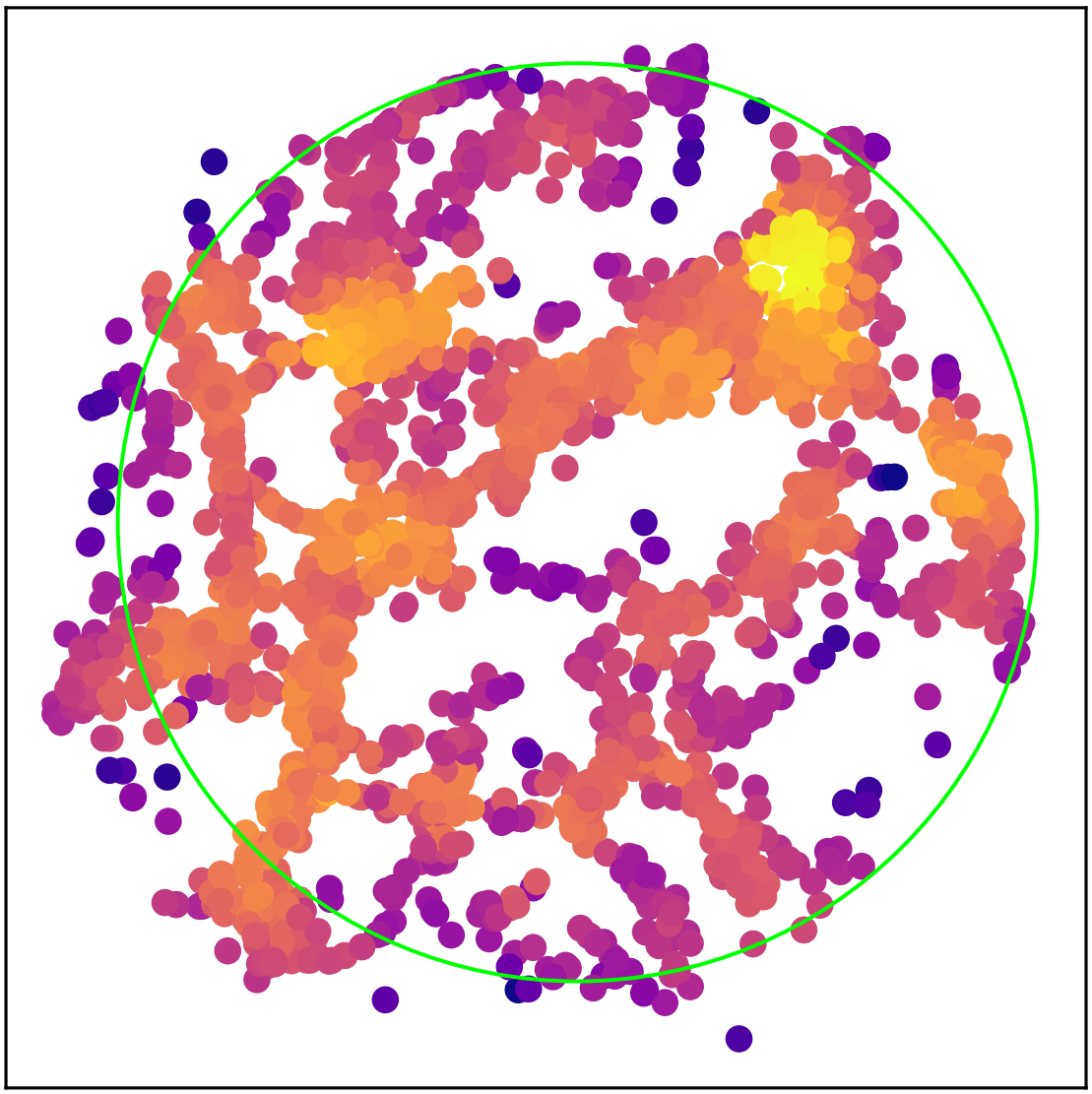

Figure 4.2
A central region of coco showing the environment according to the subhalo counts (with a slice thickness of 2 Mpc). The points show the positions of the halos coloured according to how many subhalos reside within a spherical shell with inner and outer radii of 0.2 Mpc and 2 Mpc, respectively (see Section 4.2.4 for more details). The points are coloured from lowest density (dark purple) to highest density (yellow). The lime circle shows the approximate area of the coco simulation.

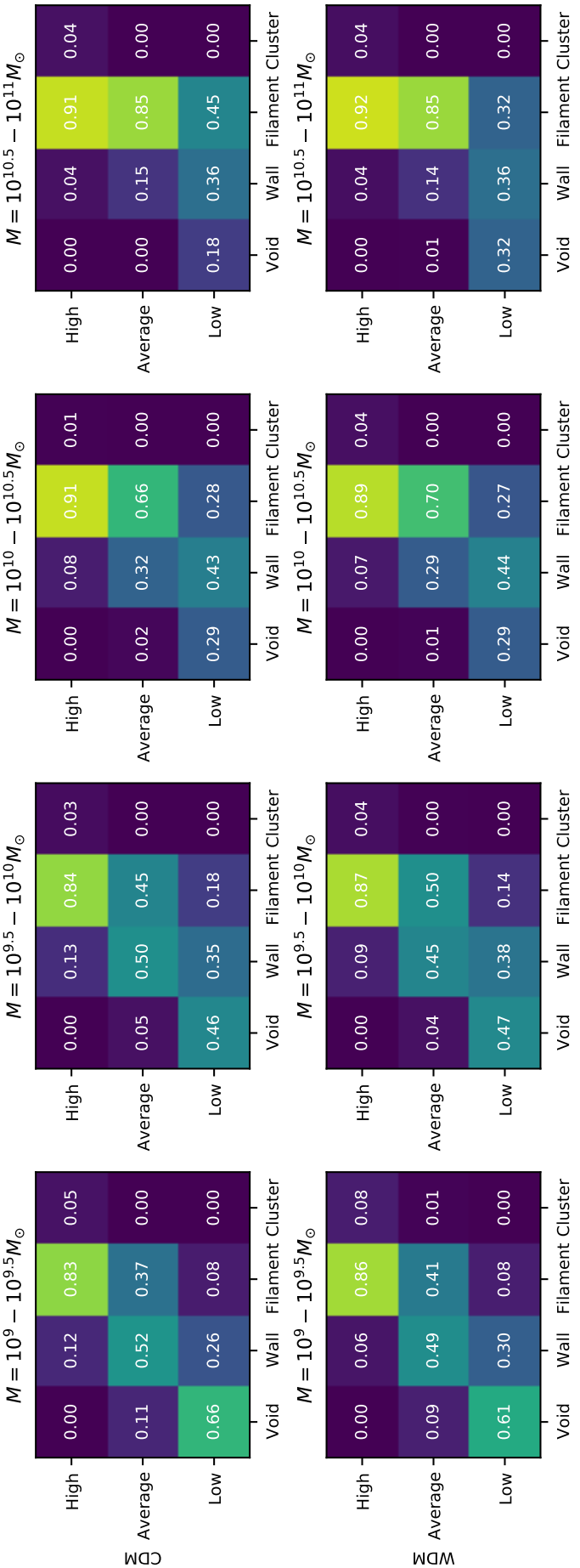

Figure 4.3
Upper: CDM environment comparison: Halo masses increase from left to right as shown above each panel. Each grid cell is coloured according to the fraction of halos in a low, average, or high local environment density that reside in each of the large-scale environment categories (Void, Wall, Filament, Cluster). The fractional values are shown in each grid cell. Lower: WDM environment comparison.

The second method for defining the environment is based on the number of nearby subhalos. A tree-based algorithm, KDTree (a Scipy Python class based on the algorithm presented in Maneewongvatana & Mount, 1999), is used to find the number of subhalos within a spherical shell with inner and outer radii of 0.2 Mpc and 2 Mpc, respectively, with mass greater than $10^9\,M_\odot$ (to avoid the cut-off in the matter power spectrum in WDM). These radii were chosen to roughly probe the local environment on the scale of the Local Group. We combine the subhalo count for all COCO-COLD subhalos into a single distribution, ensuring that the environment densities are the same across all mass bins. The distribution of subhalo counts within the spherical shell is used to define the low, average, and high-density environments based on percentiles. The environment density categories are defined as follows: a high-density environment is one where the subhalo counts are above the 95th percentile of the subhalo counts, an average-density environment is one where there are between the 40th and 60th percentiles, and a low-density environment is one where there are less than the 5th percentile. The same density cuts are used in CDM and WDM to ensure comparability. Fig. 4.2 shows the locations of subhalos in a central slice of COCO-COLD, and the subhalos are coloured according to the subhalo counts using a colour scale from dark purple (low subhalo counts) to yellow (high subhalo counts). The low and high-density environments are consistent between the environment definitions, as shown in Fig. 4.1.

4.2.4.1 Comparing environment definitions

Due to using different methods for defining environments on local and large scales, halos may reside in completely opposing environment densities in different scales. Here, we compare the local and large scale environments for the COCO halos.

The environment comparisons for CDM are shown in Fig. 4.3. Each panel of Fig. 4.3 shows the fraction of halos in a local environment category that are in any large-scale environment category. For example, the fraction of halos in a low-density local environment that reside in a void is shown in the bottom-left grid cell of each panel. The colours of each grid cell correspond to this fraction, and the value is also shown in each grid cell. In the left

panel of Fig. 4.3 ($M = 10^9 - 10^{9.5}\,\mathrm{M}_\odot$), there is a clear trend between the local-scale environment and the large-scale environment. The low-density local environment is most likely to be in a void region, the average-density environment is split almost equally between wall and filament, and the high-density environment is typically in the filament category. These diagonal trends are present across all masses. However, as halo mass increases, the large-scale environment density tends to increase for any given local-scale density. For example, in the highest mass panel, low-density halos are most likely to reside in a filament rather than a void, as in the lowest halo mass panel.

The lower panel of Fig. 4.3 shows the same environment comparison but for WDM. In WDM, the trends are the same as in CDM, however, there is a slight shift towards higher density categories for the large scale environments in the lower halo mass panels. In WDM, 8% of high local density halos are in the cluster category for large scale environment, whereas in CDM there is only 5%. The low percentage of high local density halos in clusters is likely due to the rarity of clusters in COCO, even the 95th percentile will not always probe these regions.

The spread in large scale environment for each local scale environment shows that halos in a low density local scale environment will not necessarily reside in a void environment. Therefore, the large and local scale environments will potentially have differing effects on the mergers of low mass halos.

4.3 Results

In this section, we first establish the differences between the number of mergers experienced by the whole population of halos in CDM and WDM. We also study how the merger rates differ when separated into different environments. Finally, we study *when* halos in different environments have experienced their mergers.

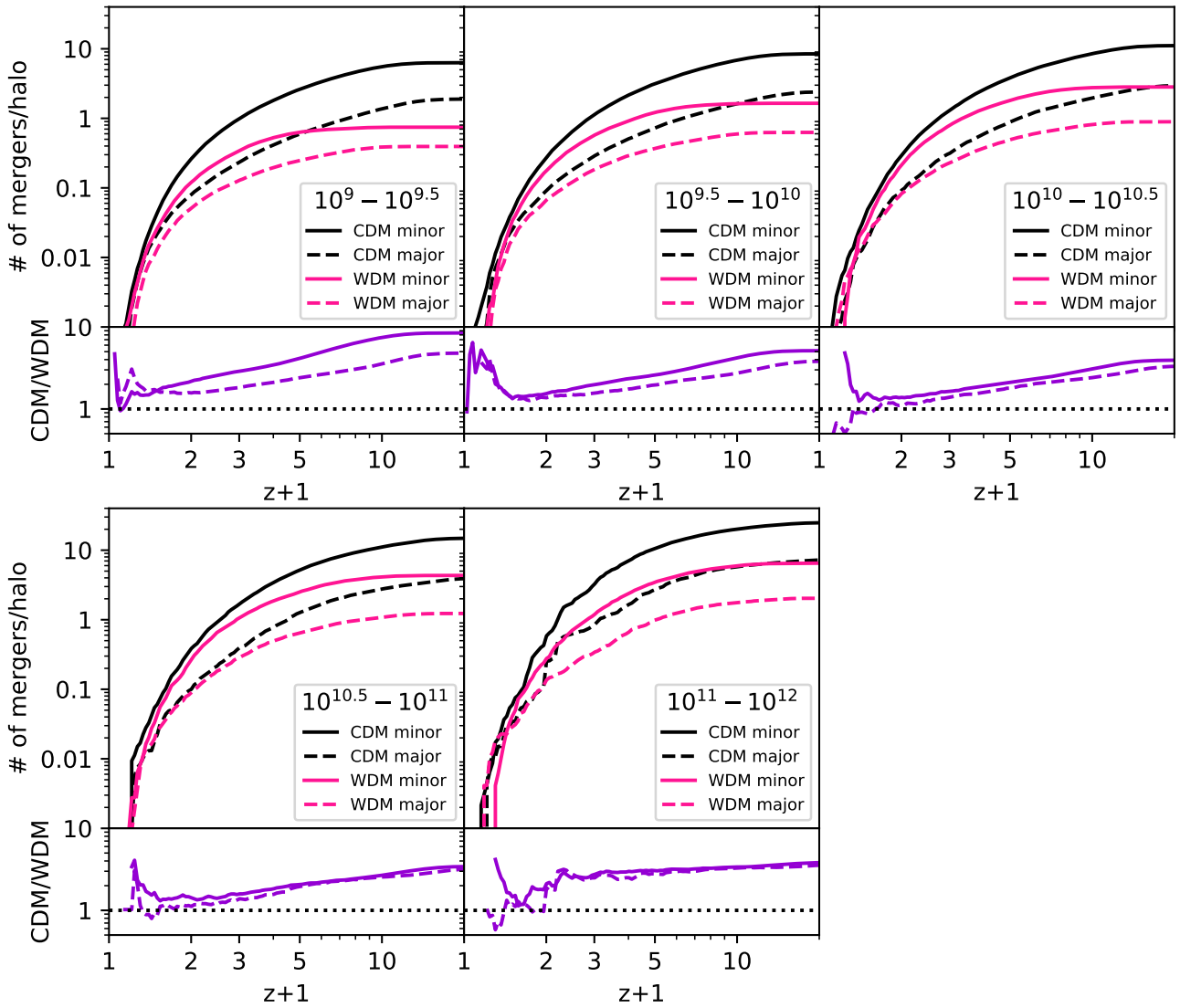

Figure 4.4

Comparing the merger rates of halos in COCO-COLD and COCO-WARM, solid lines show the minor mergers, dashed lines show the major mergers. Black represents COCO-COLD, and pink represents COCO-WARM. Each panel represents a different mass bin, and the peak mass range for each panel is shown in the legend. The lower inset of each panel shows the ratio between the cold and warm dark matter, while the dotted lines in the lower inset indicates where the 1:1 ratio lies.

4.3.1 Number of mergers

4.3.1.1 CDM vs WDM

It is important to first establish the difference between the number of mergers halos experience in cold vs warm dark matter. Fig. 4.4 shows a comparison of the cumulative number of mergers per halo in increasing mass bins between COCO-COLD (black) and COCO-WARM (pink). The lower inset of each panel shows the ratio between CDM and WDM in purple. Minor mergers are shown as solid lines, and major mergers are shown as dashed lines (the definitions of major and minor mergers can be found in section 4.2.3). Each panel shows a different mass bin, increasing from upper to lower panels from left to right, as indicated by the legend of each panel.

Fig. 4.4 reveals that more mergers (both major and minor) occur in CDM than in WDM across all masses. It is well known that these differences exist at lower masses. However, even the assembly history of higher mass halos is affected by the warm dark matter model adopted in this work. For example, the $M = 10^{11} - 10^{12}\,\mathrm{M}_{\odot}$ mass bin roughly corresponds to a Large Magellanic Cloud (LMC)- or MW-sized halo, and there are clear differences between the number of mergers experienced in the two dark matter models. These halos experience roughly ~ 2.5 times more major mergers in their lifetime in a CDM cosmology, and the differences are particularly apparent at early times. Mergers at early times have been shown to affect the formation of the thin and thick discs of Milky Way-mass galaxies. Therefore, the differences at early times between the dark matter models could have very drastic effects on the morphology of MW or LMC-like galaxies in the present epoch. These differences in early mergers could also have a significant impact on the stellar halo and other galaxy properties.

Fig. 4.4 also reveals a flattening of the cumulative number of mergers per halo at higher redshifts for the lower mass bins (most noticeable in the $M = 10^{9} - 10^{9.5}\,\mathrm{M}_{\odot}$ to $M = 10^{10} - 10^{10.5}\,\mathrm{M}_{\odot}$ mass bins) in both CDM and WDM. The causes of the flattening differ between CDM and WDM. In CDM, the curve flattens due to resolution effects. At high

redshifts, halos are much smaller, and the low-mass halos corresponding to the minor mergers begin to fall below the resolution limits of the simulation. Consequently, the total number of minor mergers in these mass bins is likely underestimated. However, in WDM, the curve flattens at earlier times due to the halo formation differences specific to WDM coming into effect. The mass cut-off for WDM used in COCO-WARM starts to decline for halos with a mass of approximately $\sim 1 \times 10^9\,\mathrm{M}_\odot$. The resolution effects are also present in WDM, however, the cut-off of the mass spectrum occurs at a much higher mass (and hence more recent redshift) and therefore dominates the observed flattening.

The lower inset of each panel reveals that the ratio between the cumulative number of mergers in CDM and WDM is highest for minor mergers in the lowest mass bin, reaching approximately 8.5 times more mergers in CDM. In contrast, the ratio between CDM and WDM for major mergers in the highest mass bin is the lowest, at around 2.5 times more mergers (roughly LMC-sized halos). The higher mass bins demonstrate that at low redshifts, the cumulative number of mergers a halo experiences is roughly the same in CDM and WDM until approximately redshift $z = 1$. Beyond $z = 1$, the number of mergers starts to deviate significantly. Minor mergers are slightly more influenced by the dark matter model at higher masses, while minor and major mergers exhibit similar trends above $10^{10}\,\mathrm{M}_\odot$.

4.3.1.2 NEXUS

Not only is the nature of dark matter important when looking at the mergers of dark matter halos, their environment can also play a key role in how many mergers a halo experiences in its lifetime. Fig. 4.5 shows the cumulative number of mergers per halo as a function of time with halos separated by their environment as defined by the NEXUS algorithm (see Section 4.2.4 for more details). The upper row of Fig. 4.5 shows the results for COCO-COLD and the lower row shows the results for COCO-WARM. Mass bins increase from left to right, here (and from now on) we only show mass bins up to $M = 10^{11}\,\mathrm{M}_\odot$ since the number of halos in the $M = 10^{11} - 10^{12}\,\mathrm{M}_\odot$ mass bin were too low to separate further by environment.

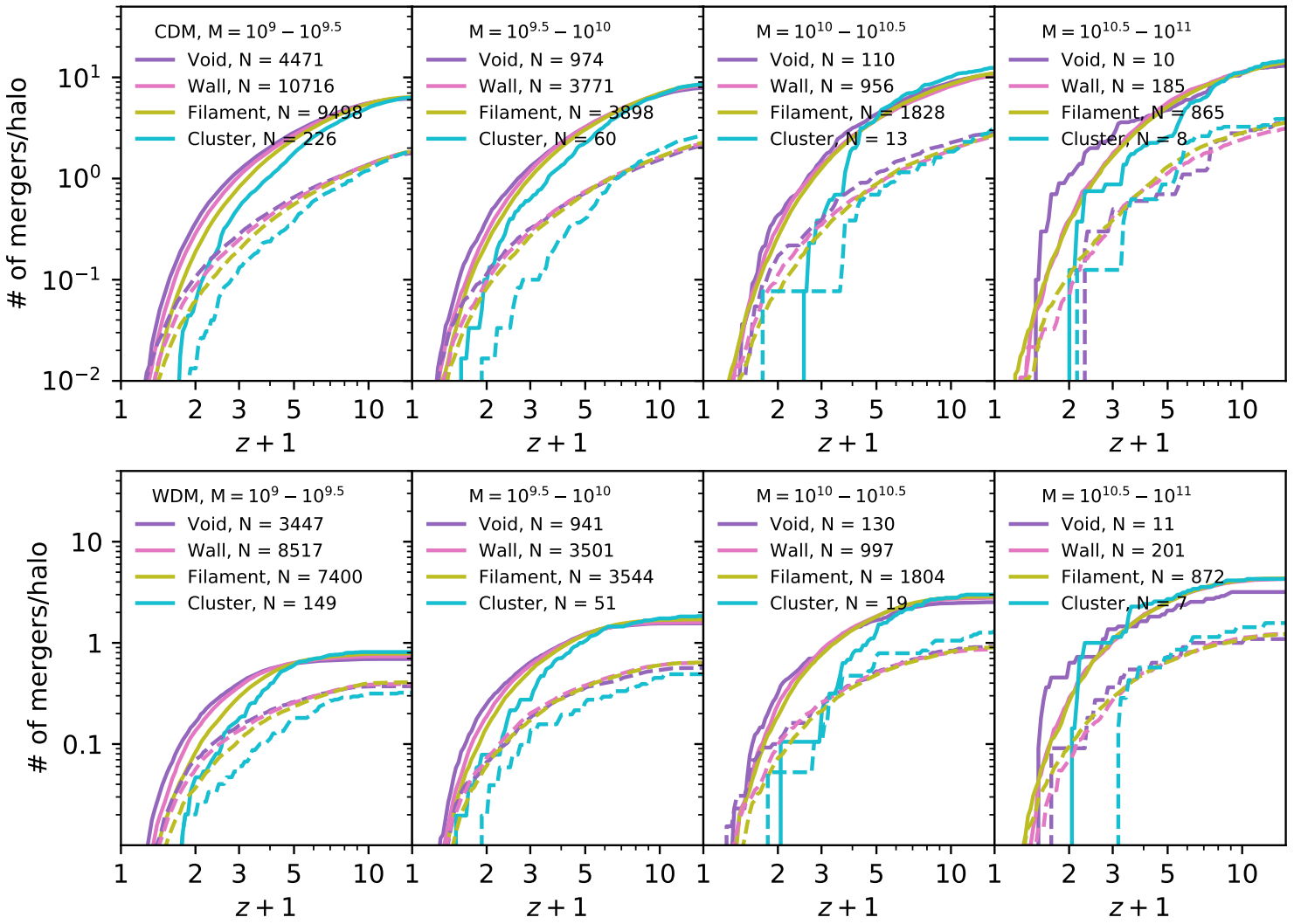

Figure 4.5

The cumulative number of mergers per halo as a function of time is shown for halos in CDM (upper) and WDM (lower) in different mass bins, increasing from left to right. Major and minor mergers are represented by solid and dashed lines, respectively. The coloured lines correspond to different environments defined using the NEXUS algorithm, where each halo is assigned a flag indicating whether it belongs to a void, wall, filament, or cluster. These environments are denoted by purple, pink, lime, and cyan, respectively. The legend of each panel indicates the number of halos in each environment.

The upper row of Fig. 4.5 (COCO-COLD) shows the cumulative number of mergers per halo separated into void, wall, filament, and cluster environments, represented by purple, pink, lime, and cyan lines, respectively. The legend of each panel indicates the number of halos in each environment. Solid lines represent minor mergers, while dashed lines represent major mergers. In the upper left panel, corresponding to the lowest mass bin ($M = 10^9 - 10^{9.5}\,\mathrm{M}_\odot$), halos in this mass range, regardless of their environment, are expected to experience an average of 6 minor mergers and 2 major mergers during their lifetimes in CDM. Both minor and major mergers show similar trends with environment, with the total number of mergers reaching a similar value in any environment category. However, there is a spread between environments at low redshifts, suggesting that halos in voids are more likely to have had recent mergers compared to halos in clusters. These trends persist across all mass bins, but the differences become more pronounced at higher masses. It is important to note that the differences observed for the void and cluster environments may be influenced by low number statistics, as indicated in the legend (number of halos).

The lower row of Fig. 4.5 (COCO-WARM) depicts the same information as the upper row, but with void, wall, filament, and cluster environments shown in purple, pink, lime, and cyan, respectively. Halos in the lowest mass bin exhibit significantly fewer mergers in their lifetimes, with an average of 0.8 minor mergers and 0.4 major mergers. In the lowest mass bin, it is evident that the minor mergers flatten for all environments by $z = 4$. This flattening is also observed in the other panels at progressively earlier times due to the mass cutoff in WDM. There are slight differences in the timing of mergers, with mergers in voids occurring more recently and mergers in clusters happening earlier. These trends are consistent across all mass bins; however, the higher mass bins exhibit greater disparities in the timing of mergers, particularly for halos in cluster environments, which tend to occur at earlier times.

To summarise, both in CDM and WDM, higher-mass halos experience a greater number of minor and major mergers compared to lower-mass halos. Fig. 4.5 illustrates that, in most cases, the total number of mergers remains consistent across different environments, but the timing of these mergers varies. The differences associated with the environment

are more significant in CDM than in WDM. Additionally, the environment has a more pronounced impact on major mergers compared to minor mergers. These disparities with the environment become more prominent as the halo mass increases. However, it is important to note that in the higher mass bins, there may be potential uncertainties arising from low number statistics.

4.3.1.3 Local environment

We have demonstrated how large scale environment influences the mergers experienced by dwarf halos. We now turn our attention to the impact of local environment. Fig. 4.6 shows the cumulative number of mergers per halo as a function of time, again separated by environment but this time using the subhalo counts method to probe the local environment (within $\sim$ 2 Mpc; see Section 4.2.4 for more details).

The upper row of Fig. 4.6 shows the COCO-COLD results separated into their low and high local environment density in purple and pink, respectively (the number of halos in low/high density environments is shown in the legend). The mass bins increase from left to right. In the low density environment there are typically more recent mergers than in the high density regions. These differences appear greatest at low redshifts and are present in both minor and major mergers. The total number of mergers experienced by the halos remains the same for high and low density local environments, however, when these mergers occur differs.

The lower row of Fig. 4.6 shows the COCO-WARM results for low and high local environment density in purple and pink. The left panel shows the lowest mass bin ($M = 10^9 - 10^{9.5}$ M$_\odot$). It is clear that there are differences at low redshift between the high and low local environment density, however, by redshift $z \sim 5$, the cumulative number of mergers per halo for high and low density environments is the same. The same features are also present in the second panel. The third panel shows differences across all redshifts, indicating that not only are mergers occurring at different times in high and low density local environments, but they are also having a slightly different total number of mergers. The right panel shows

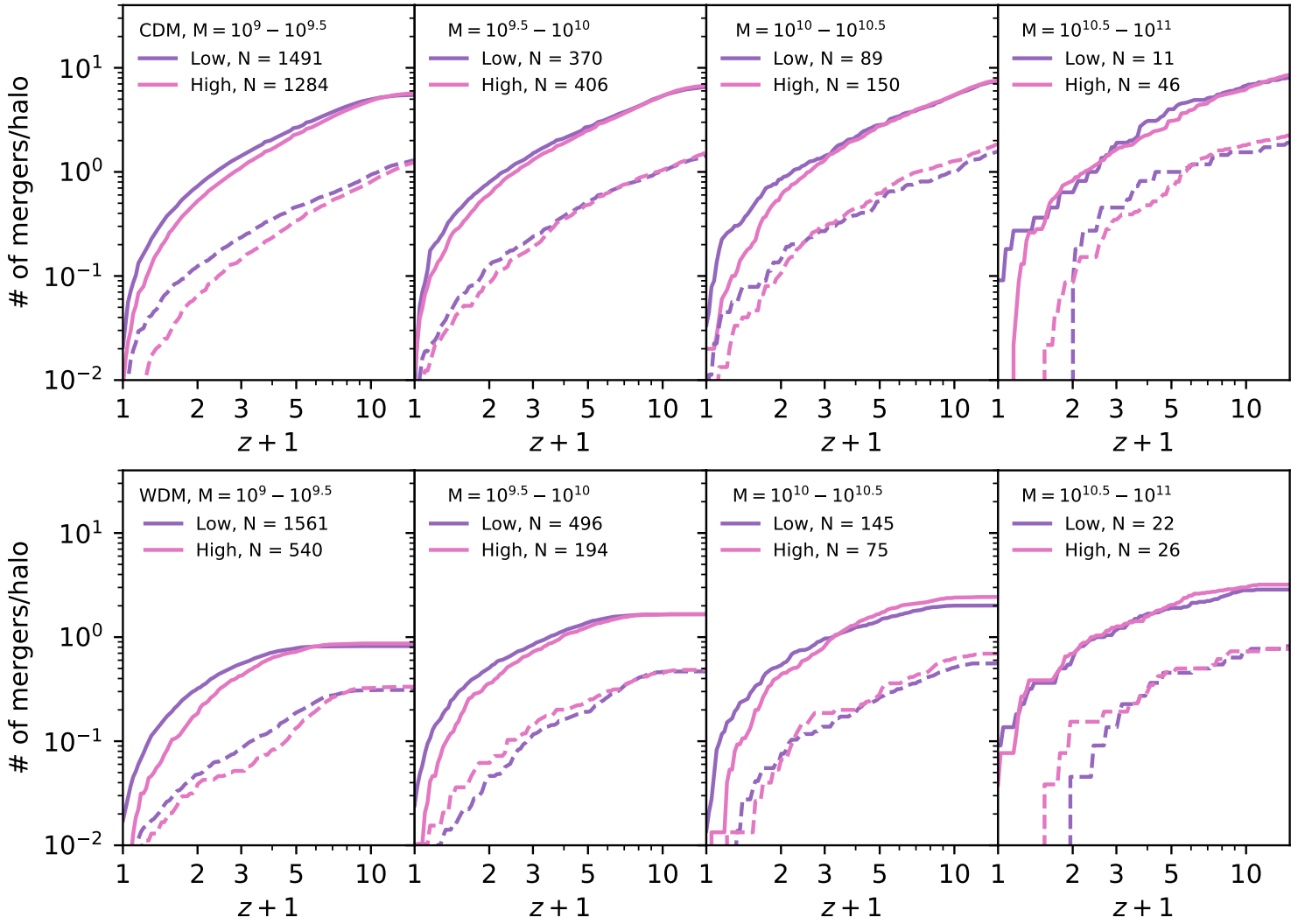

Figure 4.6

The cumulative number of mergers per halo as a function of time for halos in CDM (upper) and WDM (lower) in mass bins increasing from left to right. Each mass bin is separated into high and low density environments according to their subhalo counts, as described in Section 4.2.4. High and low densities are shown in pink and purple. The number of halos in high and low densities is shown in the legend of each panel.

the highest mass bin ($M = 10^{10.5} - 10^{11}\,\mathrm{M}_\odot$). The high and low density environments have small differences at low redshifts, but these are likely caused by the scatter given that there are very few halos in this mass bin.

Similarly to the large scale environment (NEXUS; Fig. 4.5), typically, the total number of mergers occurring in the low and high density local environments remains the same, but when these mergers occur is different. The local scale environment appears to be more important for mergers across all masses than the large scale environment.

4.3.2 Early major mergers

As shown in the previous section, a halo's environment makes more of a difference for *when* it experiences a merger rather than *how many* mergers it experiences in its lifetime. We now explore in more detail how environment affects both *early* and *late* mergers. We particularly focus on major mergers, which show more variation with environment than minor mergers. First, we establish a baseline for the fraction of halos that have experienced a major merger in their lifetime, along with the fraction of halos that have early major mergers. Fig. 4.7 shows the fraction of halos in each mass bin and NEXUS environment category that have had a major merger in their lifetimes, as well as the fraction of halos that had an early major merger (before $z = 2$). The upper and middle rows show the results for COCO-COLD and COCO-WARM, respectively, and the lower row shows the ratio between the two.

The upper row of Fig. 4.7 shows that the majority of the halos (in the mass range studied in this chapter) in COCO-COLD have had major mergers in their lifetimes (lime). For halos with a mass below $10^{10}\,\mathrm{M}_\odot$ (left 2 panels), the fraction of halos that have had major mergers is consistent across all environments. However, halos with a mass above $10^{10}\,\mathrm{M}_\odot$ show variations in their fractions of mergers between the different NEXUS environments. Note that we have to be careful with the voids and clusters at higher masses due to the low number of halos in these bins. The same trends are seen for both early mergers (before $z = 2$; cyan) and *all* mergers (lime) for all masses.

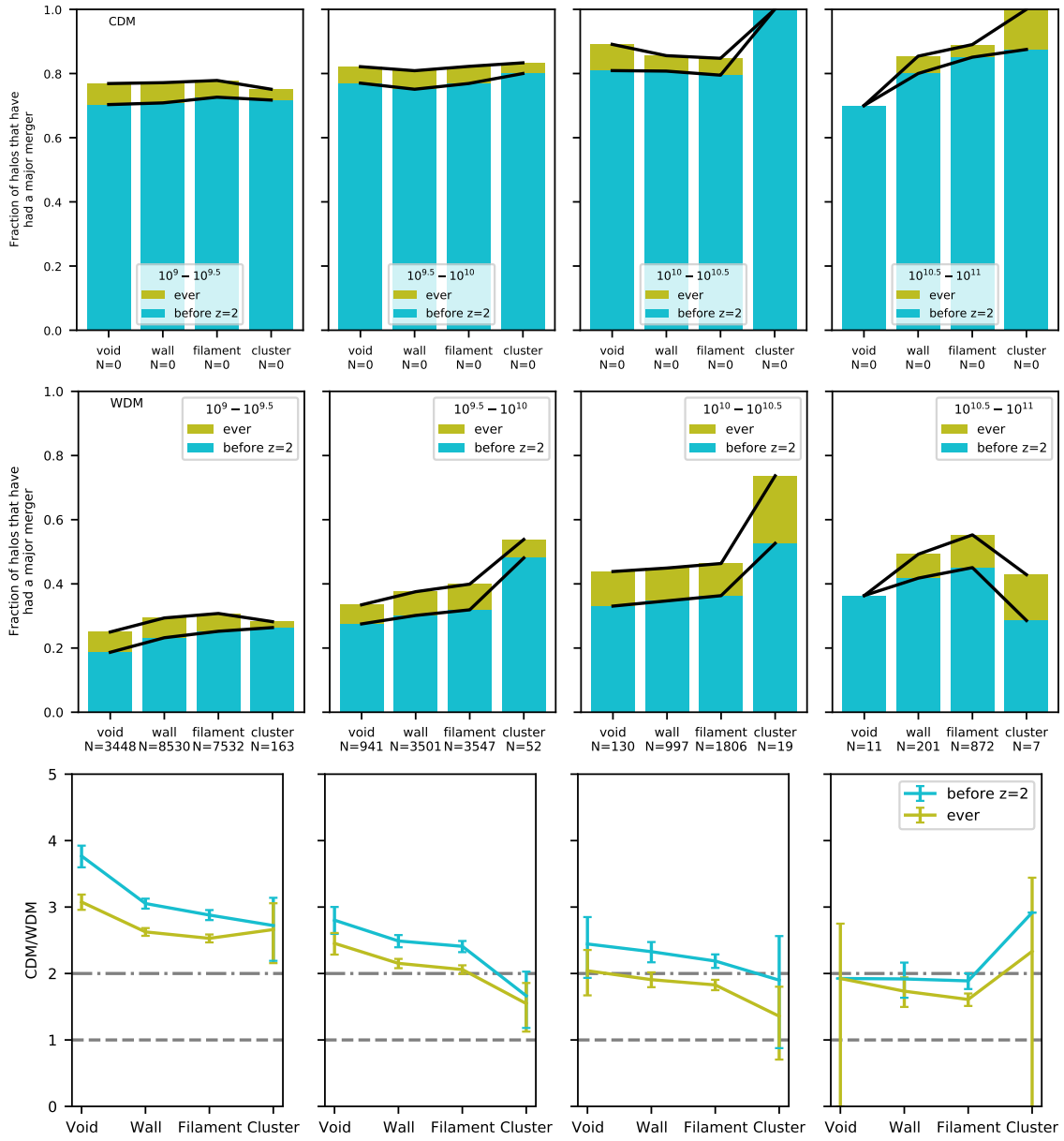

Figure 4.7

The fraction of halos that have had major mergers in their lifetimes and early mergers (before $z = 2$) separated by their NEXUS environments. Each column represents a mass bin defined at redshift $z = 0$ increasing from left to right. The upper and middle rows show the results for COCO-COLD and COCO-WARM respectively, where lime and cyan correspond to the lifetime and early mergers. Black lines connect the different environments for easier comparisons. The lower row shows the ratio between the two dark matter models, where the errorbars show the errors propagated from the Poisson noise in the bin counts from the upper and middle panels (see main text for further details).

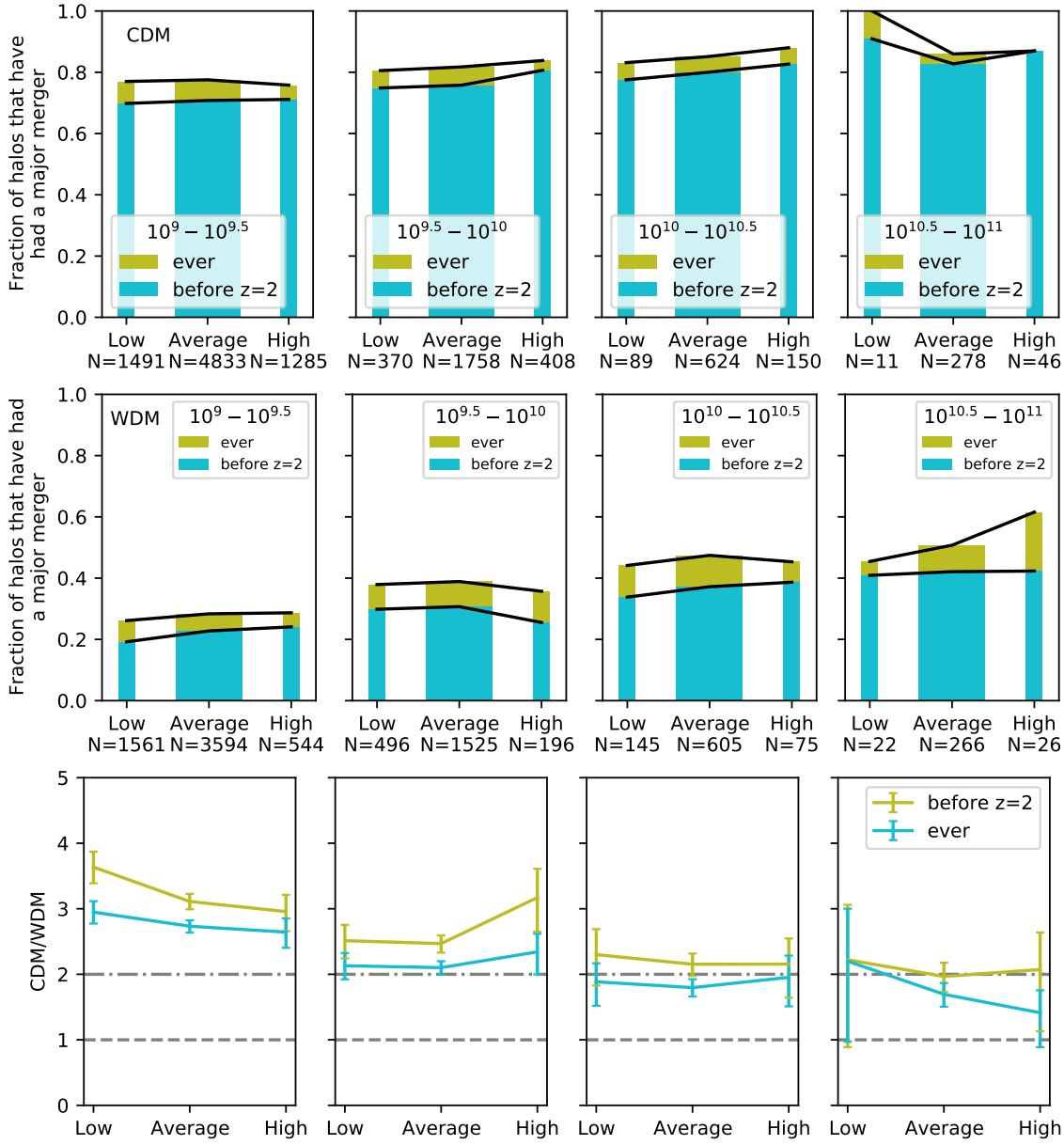

Figure 4.8

Similar to Fig. 4.7 but showing local environments instead.

Halos in COCO-WARM (middle row of Fig. 4.7) are far less likely to have experienced mergers in their lifetime (lime) or early mergers (cyan) than halos in CDM. On average, the fraction of halos in the lowest mass bin, $M = 10^9 - 10^{9.5}\,\mathrm{M}_\odot$ that have had a major merger ever is 0.28, compared with 0.77 for the same halo mass in CDM. More variation between NEXUS environments is seen at the low mass end in WDM.

The lower row of Fig. 4.7 shows the ratio between the two dark matter models. It is clear from Fig. 4.7 that halos in CDM are far more likely to experience major mergers. The biggest difference between the dark matter models can be seen in the fraction of mergers for the lowest mass halos in void environments, where we expect roughly 4 times as many halos to have experienced mergers before $z = 2$ in CDM. Typically, halos are over twice as likely to have major mergers in CDM than in WDM across all environments.

Fig. 4.8 shows the same as Fig. 4.7, but instead separates the COCO halos by their local environment densities. The upper panel shows the fraction of halos that have experienced a major merger in their lifetime (in lime) and early in their lives (before $z = 2$; in cyan) for COCO-COLD. The fraction increases with increasing mass from approximately 0.8 at the lower mass end to around 0.9 at the higher mass end. In the upper left panel, it is clear that all halos have an equal chance of having a major merger in their lifetime regardless of their local environment density. The second and third panels of the upper row (with masses $M = 10^{9.5} - 10^{10}\,\mathrm{M}_\odot$ and $M = 10^{10} - 10^{10.5}\,\mathrm{M}_\odot$ respectively) both show the same trends that halos are more likely to have experienced a major merger if they reside in a high density local environment. The right panel shows that for the highest mass halos studied in this chapter, all halos will have had a major merger in low local density environments, however, there are very few halos in this mass and environment category. The same trends are seen in both lifetime mergers and early major mergers.

The middle row of Fig. 4.8 shows the fractions for the halos in COCO-WARM, where again they are far less likely to have experienced major mergers than their CDM counterparts. The fractions of halos experiencing major mergers increase from approximately 0.3 at the low mass end to around 0.5 at the higher mass end. Typically, the trends for each mass bin as a function of environment are mostly flat, indicating that in WDM, a halo's local

environment does not significantly affect its chances of experiencing a major merger in its lifetime.

The lower row of Fig. 4.8 shows the ratio between the CDM and WDM models. The ratios decrease with increasing mass, hence, as expected, the dark matter models make more differences at lower masses. The highest ratio is approximately 4 times more likely to have experienced mergers at the low mass end, which decreases to around 2 times more likely at the high mass end.

There is more variation in the ratios between CDM and WDM for the large scale environments (shown in Fig. 4.7) than the local scale environments (shown in Fig. 4.8). This could be because a halo's large-scale environment is more likely to remain the same throughout its entire life, while its local scale environment is more susceptible to change over time.

4.3.3 Recent major mergers

It is more likely to observe evidence of recent major mergers, hence, it is important to establish the differences between the fractions of halos experiencing recent mergers in different environments and dark matter models.

Fig. 4.9 shows the fraction of halos that have had recent major mergers (since $z = 1$ and $z = 2$) separated by NEXUS environments for both COCO-COLD (upper row) and COCO-WARM (middle row), in pink and purple. The ratio between the dark matter models is shown in the bottom row.

The upper left panel of Fig. 4.9 shows that the fraction of halos having recent major mergers in the lowest mass bin ($M = 10^9 - 10^{9.5}\,\mathrm{M}_\odot$) decreases with increasing density for both mergers since $z = 2$ (purple) and $z = 1$ (pink). In the three higher mass bins, the trends between environment are less obvious. One commonality for all masses in COCO-COLD is that the lowest fraction of halos experiencing recent major mergers is typically in the cluster environment category. However, at higher masses, this category is not well-populated by halos, and therefore cannot be trusted.

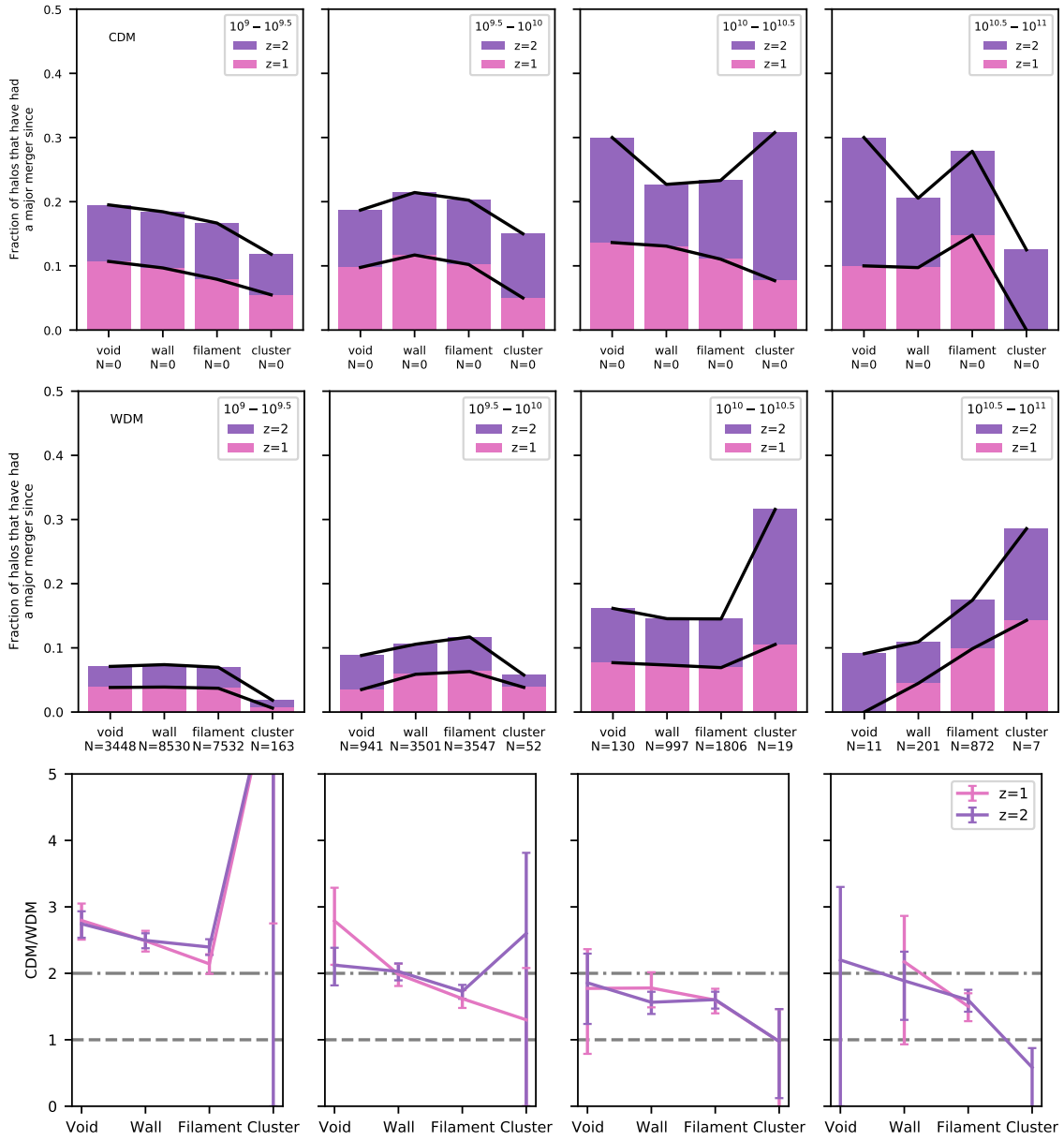

Figure 4.9

The fraction of halos that have had recent major mergers (since $z = 1, 2$) is separated by their NEXUS environment category. The upper and middle panels show the results for COCO-COLD and COCO-WARM (in pink and purple). Black lines connect the different environments for easier comparisons. The lower row shows the ratio between the cold and warm dark matter models in pink and purple for $z = 1$ and $z = 2$, respectively, where error bars represent the Monte Carlo Poisson errors.

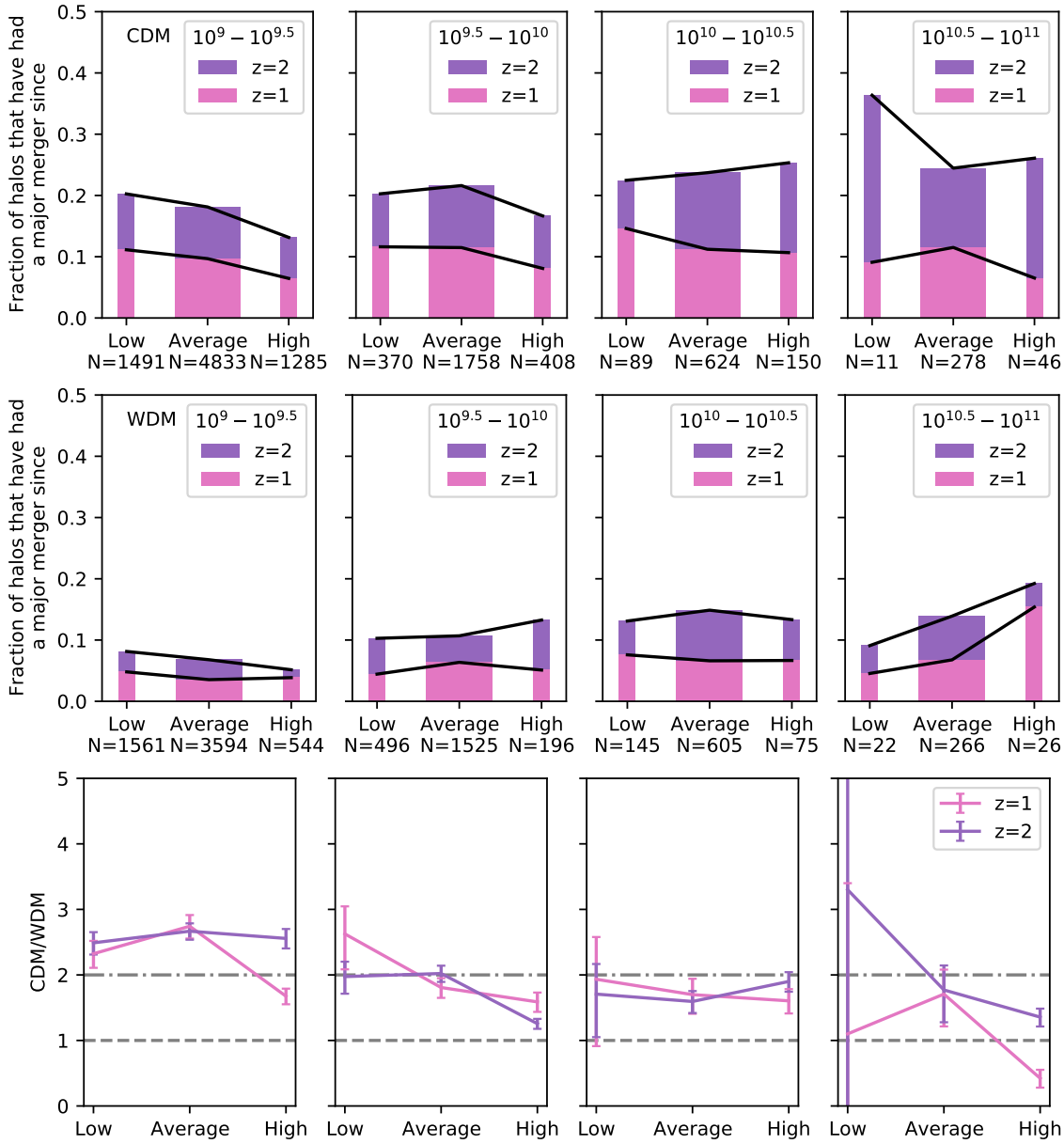

Figure 4.10

Similar to Fig. 4.9 but instead showing the fractions of halos that have had recent major mergers separated by their local environments.

The middle row of Fig. 4.9 shows the fraction of halos that have had recent major mergers in COCO-WARM. The fractions in COCO-WARM are much lower than in COCO-COLD across all masses, particularly the low-mass end, which is affected the most by the cut-off in the halo mass function in WDM. The fractions of halos experiencing recent major mergers do not appear to be as affected by the large-scale environment as in CDM. For the lower-mass halos (below $10^{10}\,\mathrm{M}_{\odot}$), the halos in clusters are far less likely to have had a recent merger than the other environment classes, with only 0.6% (3.8%) of halos with mass $M = 10^{9} - 10^{9.5}\,\mathrm{M}_{\odot}$ ($M = 10^{9.5} - 10^{10}\,\mathrm{M}_{\odot}$) experiencing a major merger by $z = 1$. Halos in clusters are also far less likely to have experienced recent major mergers in the second lowest mass bin ($M = 10^{9.5} - 10^{10}\,\mathrm{M}_{\odot}$, centre-left panel of the middle row). For the higher-mass halos ($M > 10^{10}\,\mathrm{M}_{\odot}$; right two panels), it appears as though there are far more mergers occurring in denser environments. However, we need to take great care in interpreting the results in this mass regime due to the low number statistics.

The ratio between COCO-COLD and COCO-WARM is depicted in the lower row of Fig. 4.9, with error bars representing the Monte Carlo Poisson uncertainty. These uncertainties account for the statistical fluctuations in the number of halos within each environment category, and they were propagated using a Monte Carlo technique. Typically, it is twice as likely that a halo has had a recent major merger in CDM than in WDM across all masses. There is a slight trend indicating that CDM halos are more likely to have experienced recent major mergers in void environments, and the difference between dark matter models decreases with increasing environment density.

Fig. 4.10 shows the fraction of halos that have had recent major mergers (since $z = 1, 2$) according to their local environment. The upper and middle rows show the results for COCO-COLD and COCO-WARM respectively. The lower row shows the ratio between the two dark matter models.

The top left panel of Fig. 4.10 shows that low-mass halos in CDM are more likely to have experienced a recent major merger if they reside in low-density environments. The fraction of halos that have experienced mergers decreases with increasing density. The second panel on the upper row shows that the fraction of halos that have experienced a major

merger is at its peak for halos in an average-density environment. For the third panel, the trends reverse between $z = 1$ and $z = 2$. For mergers since $z = 1$, the halos are more likely to have had a major merger in low-density environments. However, by $z = 2$, they are more likely to have had a major merger in a high-density environment. The upper right panel shows the highest mass bin ($M = 10^{10.5} - 10^{11}\,M_\odot$). In this case, we need to be careful about interpreting the results since there are only 11 halos in the low-density environment.

The middle row shows the results for COCO-WARM. The fraction of halos that have experienced recent major mergers since $z = 1$ and $z = 2$ are shown in pink and purple, respectively. In the $10^9 - 10^{9.5}\,M_\odot$ mass bin, there is a higher fraction of halos experiencing recent major mergers in a low local density environment for both $z = 1$ and $z = 2$. In the $10^{9.5} - 10^{10}\,M_\odot$ mass bin, by $z = 2$, a halo in this mass bin is more likely to have experienced a major merger in a high local density environment. The third panel shows no significant trends.The highest mass bin shows that the fraction of halos that have experienced recent major mergers increases with increasing local density. Overall, COCO-WARM shows fewer differences between the environments compared to COCO-COLD.

The lower row shows the ratio between the CDM and WDM results from the upper two rows. There is less variation than Fig. 4.9, however, the most significant difference between dark matter models remains in the lowest mass bin in a low local environment density, where halos in CDM are up to 3 times more likely to have had a major merger since $z = 2$ than in WDM.

Our results are in agreement with the work presented in Hester & Tasitsiomi (2010), who observed an increasing number of subhalo mergers with decreasing density using the Millennium simulation. Hester & Tasitsiomi (2010) defined their environment using subhalo counts in spheres and shells around halos, similar to the local-scale environment we define in Section 4.2.4. However, our results are not consistent with Fakhouri & Ma (2009), who stated that there is an increasing number of mergers per halo with increasing density using the same simulation. Fakhouri & Ma (2009) defined mergers using FoF halos, whereas in this work (and in Hester & Tasitsiomi, 2010), mergers are defined using subhalos. Not only is the definition of a merger different between this work and Fakhouri

& Ma (2009), but they also used a different method for defining the environment using the particle data. Therefore, it is clear that different definitions of what is considered a merger and the definition of environment can drastically affect the results.

To summarise, halos in CDM see larger differences in the fraction of halos that experience recent major mergers in different environments than in WDM. The large scale environments see slight differences between dark matter models, where void halos are more likely to have experienced recent major mergers. The difference between the dark matter models decreases with increasing large scale environment density. Halos in CDM also see more pronounced differences in the fraction of halos experiencing mergers in different local scale environments. The environment we suggest for targeted dwarf observations are low density environments on a local scale and void regions, where halos are 3-4 times more likely to experience a recent major merger in CDM than WDM.

4.4 Conclusions

We provide the merger rates of dwarf halos as a function of environment for both CDM and WDM versions of COCO. We defined the environment of the dwarf halos using two different methods; a cosmic web finding algorithm, NEXUS, and a local scale environment based on the subhalo counts within a spherical shell. We looked at the cumulative major and minor mergers per subhalo as a function of redshift in different environments and the fractions of halos experiencing early or recent major mergers to determine the optimal region for targeted observations of dwarf galaxies with upcoming surveys to investigate the nature of dark matter. Our main conclusions are as follows:

- When comparing the cumulative number of mergers for CDM and WDM, we found significant differences across all mass bins for both major and minor mergers. The impact of the nature of the dark matter particle is well established for the lowest mass halos. We found that there was also a significant impact on the total number of mergers experienced by larger halos (with mass $M = 10^{11} - 10^{12}\,\mathrm{M}_{\odot}$, roughly

corresponding to the size of an LMC- or MW-like galaxy). In WDM, these halos would have roughly 3 times fewer major mergers than in CDM. This is because at high redshifts these halos are much smaller, and so their merging satellites begin to fall below the mass cutoff in warm dark matter.

- We found that the large-scale environment (NEXUS) had more impact on CDM than WDM, and it had a bigger impact on the major mergers. These differences were also at their greatest for higher mass halos; however, the number of higher mass halos was far smaller in our sample, and so the larger differences could be due to scatter and low number statistics.

- The local environment also made more of a difference in CDM than in WDM. The differences between low and high local density in CDM were apparent across all masses and were present for both minor and major mergers.

- The total number of mergers a halo experiences over its lifetime is roughly independent of its environment (either large-scale or local). However, *when* a halo typically experiences a merger can be affected by the environment, with halos in low-density regions more likely to experience recent mergers.

- The large-scale environment has a greater impact than local environment on the fraction of halos that experienced a major merger at early times. This is likely due to a halo remaining in one category of large-scale environment for its entire lifetime, whereas a halo's local-scale environment is more susceptible to changes with time.

- The biggest differences between dark matter models for recent major mergers were seen in a low density and void environments, where halos were up to 3 times more likely to have experienced recent major mergers.

In summary, we find that the best places to look for differences between cold and warm dark matter models using mergers of dwarf galaxies are in either a low local density environment or a void region with upcoming spectroscopic and photometric surveys such

as Dark Energy Spectroscopic Instrument (DESI), and the Vera Rubin Legacy Survey of Space and Time (LSST).

4.5 Future work

To prepare this thesis chapter for submission as a paper to MNRAS, I would like to show how many of the halo mergers are likely to host galaxies. Not all dark matter halos contain stars, previously Deason et al. (2022) used a model to see which halos in COCO would have stars. I intend to analyse the semi-analytic galaxy formation model, GALFORM (Lacey et al., 2016) to study the possible stellar components of the low mass halos studied in this chapter.

Subhalos in COCO are populated with galaxies using the semi-analytic modelling code GALFORM. This version of GALFORM consolidates many features from previous versions (Cole et al., 1994, 2000), including the assumption of a top-heavy initial mass function (IMF) in starbursts. The adoption of a top-heavy IMF is necessary to reproduce the abundance of star-forming sub-millimeter galaxies (Baugh et al., 2005). Additionally, this GALFORM model incorporates the AGN feedback model introduced by Bower et al. (2006) and utilises the star formation law proposed by Lagos et al. (2011), which relies on the molecular gas content of the interstellar medium (ISM). The free parameters of the Lacey et al. (2016) model are calibrated to match various observational constraints, such as the optical and near-infrared luminosity functions, the HI mass function, and the fraction of early- and late-type galaxies at $z = 0$.

These results from GALFORM could have important implications for observing the differences in dark matter models using dwarf galaxies for future observational surveys.

CHAPTER 5

Conclusions

This thesis has used and developed many methods for studying analogues of the Milky Way and their mergers. In particular, simulations have been an invaluable resource for these studies. Through studying these MW-like galaxies, it has allowed us to gain a deeper understanding of our place in the universe. The simulations have also allowed us to produce predictions for upcoming observations and to find the best regions in the universe to study the nature of dark matter using dwarf galaxies.

Chapter 2 showed that MW-analogues with a constrained accretion history are very rare, with only 0.65% of MW-like galaxies in EAGLE having a similar assembly history to our own Galaxy. These MW-analogues, with a GES-like merger and an LMC-like satellite, have much lower masses than expected at high redshifts. The biggest contributor for reducing the sample size of galaxies in this category was requiring a dearth of major mergers between the GES-like dwarf and the infall of the LMC-like satellite.

Despite the absence of any restrictions regarding morphology, colour, or rate of star formation for the selection of galaxies in the sample, it's noteworthy that all the MW-analogues can be found within the "blue cloud" region on the colour-stellar mass diagram. Galaxies with an LMC host more satellites than those without, including those with a GES event, thanks to the additional satellites introduced by the LMC.

Chapter 3 was inspired by the results from Chapter 2. If the mass of MW-like galaxies was much lower than anticipated at higher redshifts, then this would have immense consequences for observing high redshift progenitors of MW-like galaxies with upcoming JWST surveys. We found that the progenitors of MW-, LMC-, and GES-like galaxies would be observable until redshifts $z \sim 6$, $z \sim 4$, and $z \sim 5$, respectively (see Fig. 3.5). These building blocks of the MW would nearly always be observable within one field of view for the JWST/NIRCam instrument.

One intriguing result of the work in Chapter 3 revealed that the progenitors of MW-, LMC-, and GES-like galaxies are all fairly similar at higher redshifts. It is likely that the reason these galaxies became what they are today–the Milky Way, a massive satellite, and an ancient major merger–is due to their relative locations. The MW and GES were very close together at early times, and so they had to merge. The LMC was slightly further away and thus survived as a satellite to the present day. The Milky Way just happened to be slightly more massive than the GES, and so it survived as the main galaxy.

The colour-magnitude diagrams (CMDs) of the progenitor galaxies resembling the MW-analogues indicate that the three constituents (MW, LMC, GES) should occupy a comparable region of the CMD. While galaxies with a mass similar to those resembling the MW, LMC, and GES in the MW-analogue systems exhibit a broad array of colours, their magnitude range remains quite narrow. The CMDs should be able to help identify possible MW-analogue systems in JWST surveys.

Chapter 3 also demonstrated that the basic dust model employed in this study aligns with the results obtained from the computationally intensive radiative transfer code, SKIRT. This result holds significance as SKIRT is very computationally demanding, whereas the simpler model used here serves as a good approximation for characterising the dust content in simulated galaxies.

Chapter 4 showed that not only are there significant differences for the assembly history of low mass halos, there are also important differences for higher mass halos in CDM vs WDM. Low mass halos experience 5 times more major mergers in CDM and higher mass halos (similar to the halo mass of the LMC or even MW) would experience 3 times more

major mergers in CDM than WDM. For halos in this mass range, the differences between CDM and WDM are the equivalent to having three or one major mergers in their lifetimes on average.

Chapter 4 also showed that the different dark matter models have a much greater impact on the mergers than any type of environment does. Large scale (cosmic web) environments have more of an impact than local scale environment on a halos early mergers, likely due to a halo remaining in one type of cosmic geometry for its entire lifetime whereas a halo's local environment is subject to more changes over time. We found that the best places to look for differences between cold and warm dark matter models using mergers of dwarf galaxies are in either a low local density environment or a void region. This result seemed slightly counter intuitive since there are far fewer nearby subhalos in low density or void environments for potential mergers. However, in higher density or cluster environments, subhalos have much greater relative velocities and so are therefore less likely to merge with one another.

We therefore suggest these regions for upcoming spectroscopic and photometric surveys such as Dark Energy Spectroscopic Instrument (DESI), and the Vera Rubin Legacy Survey of Space and Time (LSST). To finalise the work presented in Chapter 4, additional analysis using GALFORM is required to establish the relationship between subhalo mergers and their stellar counterparts. This connection could significantly impact our capacity to observe the distinctions between CDM and WDM.

5.1 Future work

The field of theoretical astronomy is about to enter a new era due to the upcoming COLIBRE simulations. These cutting-edge simulations will provide unprecedented insights into galaxy formation and evolution and Galactic studies. The COLIBRE simulations are the next generation, state-of the art hydrodynamical cosmological simulations which include major improvements to the galaxy formation and subgrid physics model. There are many proposed boxsizes including one $(250\ \mathrm{Mpc})^3$ simulation and resolution similar to EAGLE.

5.1.1 Can Milky Way analogues with constrained accretion histories form in any environment?

An extension of Chapter 2, would be possible using the upcoming COLIBRE simulations, with better statistics and better sub-grid physics models it will be possible to understand in more detail the atypical properties of the assembly history of the Milky Way. The larger statistics (provided by the proposed (250 Mpc)^3 COLIBRE simulation) will allow us to study the environments in the simulation which are able to form galaxies analogous to the Milky Way, and I will determine if Milky Way galaxies can only form in one specific environment of if they could form anywhere in the universe.

5.1.2 The Aurora in simulations

Following my study of high redshift progenitors of Milky Way analogues for JWST observations in Chapter 3, I will find analogues of the Aurora (the pre-disc Milky Way material) in the upcoming COLIBRE simulations. Key chemical abundances are traced within the simulations and I will compare these chemical abundances in the MW-analogue Auroras and the failed MW Auroras to see if there are any key differences.These chemical signatures can also be compared with those in the spectroscopic surveys, such as GALAH and APOGEE. Investigating the Aurora in simulations will bring new light in how the properties of the early galaxy effects its future growth.

5.1.3 How accretion events affect the density profiles of galactic stellar halos

The driving force for the evolution of the stellar halo must be due to mergers. Merger events occur on very short time scales and having frequent outputs to look at the rapidly changing profile is important. I plan to use state of the art simulations to study the connection between the density profile of stellar halos and the accretion history of the halos in more

detail. High resolution or zoom in simulations would be best for this type of project, such as the VINTERGATAN simulations (Agertz et al., 2021). I will look at the diversity in shape of the density profiles among various halos. I will also look at the evolution of the individual density profiles with time, in particular, focusing on the formation and evolution of the break in the density profile. Finally, I will look at individual accretion events and how stellar halo profiles change during these events (or as a result of these events). Understanding the connection between the surface brightness profiles of galaxies and their mergers will allow us to translate our understanding of the accretion histories of the Milky Way and M31 to broader statements about thousands of galaxies whose halos we will be able to profile with e.g. the Hyper Suprime-Cam (HSC) survey, LSST, and the Roman space telescope.

Bibliography

Abadi M. G., Navarro J. F., Steinmetz M., 2006, Monthly Notices of the Royal Astronomical Society, 365, 747

Adelman-McCarthy J. K., et al., 2007, The Astrophysical Journal Supplement Series, 172, 634

Agertz O., et al., 2021, Monthly Notices of the Royal Astronomical Society, 503, 5826

Anderhalden D., Schneider A., Macciò A. V., Diemand J., Bertone G., 2013, Journal of Cosmology and Astroparticle Physics, 2013, 014

Aragón-Calvo M. A., Jones B. J. T., van de Weygaert R., van der Hulst J. M., 2007, Astronomy and Astrophysics, 474, 315

Asplund M., Grevesse N., Sauval A. J., Scott P., 2009, Annual Review of Astronomy and Astrophysics, 47, 481

Avila-Reese V., Colín P., Valenzuela O., D'Onghia E., Firmani C., 2001, The Astrophysical Journal, 559, 516

Baes M., Verstappen J., Looze I. D., Fritz J., Saftly W., Pérez E. V., Stalevski M., Valcke S., 2011, The Astrophysical Journal Supplement Series, 196, 22

Barbá R. H., Minniti D., Geisler D., Alonso-García J., Hempel M., Monachesi A., Arias J. I., Gómez F. A., 2019, The Astrophysical Journal, 870, L24

Barnes J. E., Hernquist L. E., 1991, The Astrophysical Journal, 370, L65

Barton Gillespie E., Geller M. J., Kenyon S. J., 2003, The Astrophysical Journal, 582, 668

Baugh C. M., Lacey C. G., Frenk C. S., Granato G. L., Silva L., Bressan A., Benson A. J., Cole S., 2005, Monthly Notices of the Royal Astronomical Society, 356, 1191

Bechtol K., et al., 2015, The Astrophysical Journal, 807, 50

Beichman C. A., Rieke M., Eisenstein D., Greene T. P., Krist J., McCarthy D., Meyer M., Stansberry J., 2012, Conference proceedings: Space Telescopes and Instrumentation 2012, 8442, 84422N

Bell E. F., et al., 2008, The Astrophysical Journal, 680, 295

Bell E. F., Monachesi A., Harmsen B., de Jong R. S., Bailin J., Radburn-Smith D. J., D'Souza R., Holwerda B. W., 2017, The Astrophysical Journal Letters, 837, L8

Belokurov V., Koposov S. E., 2016, Monthly Notices of the Royal Astronomical Society, 456, 602

Belokurov V., Erkal D., Deason A. J., Koposov S. E., De Angeli F., Evans D. W., Fraternali F., Mackey D., 2017, Monthly Notices of the Royal Astronomical Society, 466, 4711

Belokurov V., Erkal D., Evans N. W., Koposov S. E., Deason A. J., 2018, Monthly Notices of the Royal Astronomical Society, 478, 611

Belokurov V., Sanders J. L., Fattahi A., Smith M. C., Deason A. J., Evans N. W., Grand R. J. J., 2020, Monthly Notices of the Royal Astronomical Society, 494, 3880

Benitez-Llambay A., 2015, py-sphviewer: Py-SPHViewer v1.0.0, doi:10.5281/zenodo.21703, https://zenodo.org/record/21703

Benitez-Llambay A., Frenk C., 2020, Monthly Notices of the Royal Astronomical Society, 498, 4887

Bennett C. L., Hallin A. L., Naumann R. A., Springer P. T., Witherell M. S., Chrien R. E., Baisden P. A., Sisson D. H., 1981, Physics Letters B, 107, 19

Benson A. J., et al., 2013, Monthly Notices of the Royal Astronomical Society, 428, 1774

Benítez-Llambay A., Frenk C. S., Ludlow A. D., Navarro J. F., 2019, Monthly Notices of the Royal Astronomical Society, 488, 2387

Bertone G., Hooper D., 2018, Reviews of Modern Physics, 90, 045002

Bertone G., Hooper D., Silk J., 2005, Physics Reports, 405, 279

Bertschinger E., 1987, The Astrophysical Journal, 323, L103

Bertschinger E., 2001, The Astrophysical Journal Supplement Series, 137, 1

Besla G., Martínez-Delgado D., van der Marel R. P., Beletsky Y., Seibert M., Schlafly E. F., Grebel E. K., Neyer F., 2016, The Astrophysical Journal, 825, 20

Bignone L. A., Helmi A., Tissera P. B., 2019, The Astrophysical Journal Letters, 883, L5

Bland-Hawthorn J., Gerhard O., 2016, Annual Review of Astronomy and Astrophysics, 54, 529

Bode P., Ostriker J. P., Turok N., 2001, The Astrophysical Journal, 556, 93

Bonaca A., Conroy C., Wetzel A., Hopkins P. F., Kereš D., 2017, The Astrophysical Journal, 845, 101

Bonaca A., et al., 2020, The Astrophysical Journal, 897, L18

Bose S., Hellwing W. A., Frenk C. S., Jenkins A., Lovell M. R., Helly J. C., Li B., 2016, Monthly Notices of the Royal Astronomical Society, 455, 318

Bose S., Deason A. J., Frenk C. S., 2018, The Astrophysical Journal, 863, 123

Bose S., et al., 2019, Monthly Notices of the Royal Astronomical Society, 486, 4790

Bose S., Deason A. J., Belokurov V., Frenk C. S., 2020, Monthly Notices of the Royal Astronomical Society, 495, 743

Bournaud F., Jog C. J., Combes F., 2005, Astronomy and Astrophysics, 437, 69

Bouwens R. J., et al., 2015, The Astrophysical Journal, 803, 34

Bouwens R. J., et al., 2016, The Astrophysical Journal, 830, 67

Bouwens R. J., et al., 2021, The Astronomical Journal, 162, 47

Bower R. G., Benson A. J., Malbon R., Helly J. C., Frenk C. S., Baugh C. M., Cole S., Lacey C. G., 2006, Monthly Notices of the Royal Astronomical Society, 370, 645

Boyarsky A., Ruchayskiy O., Shaposhnikov M., 2009a, Annual Review of Nuclear and Particle

Science, 59, 191

Boyarsky A., Ruchayskiy O., Iakubovskyi D., 2009b, Journal of Cosmology and Astroparticle Physics, 2009, 005

Boylan-Kolchin M., Springel V., White S. D. M., Jenkins A., Lemson G., 2009, Monthly Notices of the Royal Astronomical Society, 398, 1150

Boylan-Kolchin M., Besla G., Hernquist L., 2011a, Monthly Notices of the Royal Astronomical Society, 414, 1560

Boylan-Kolchin M., Bullock J. S., Kaplinghat M., 2011b, Monthly Notices of the Royal Astronomical Society, 415, L40

Boylan-Kolchin M., Bullock J. S., Kaplinghat M., 2012, Monthly Notices of the Royal Astronomical Society, 422, 1203

Boylan-Kolchin M., Weisz D. R., Johnson B. D., Bullock J. S., Conroy C., Fitts A., 2015, Monthly Notices of the Royal Astronomical Society, 453, 1503

Boylan-Kolchin M., Weisz D. R., Bullock J. S., Cooper M. C., 2016, Monthly Notices of the Royal Astronomical Society, 462, L51

Brook C. B., Kawata D., Gibson B. K., Flynn C., 2003, The Astrophysical Journal, 585, L125

Brook C. B., Kawata D., Gibson B. K., Freeman K. C., 2004, The Astrophysical Journal, 612, 894

Bullock J. S., Boylan-Kolchin M., 2017, Annual Review of Astronomy and Astrophysics, vol. 55, issue 1, pp. 343-387, 55, 343

Bullock J. S., Johnston K. V., 2005, The Astrophysical Journal, 635, 931

Busha M. T., Marshall P. J., Wechsler R. H., Klypin A., Primack J., 2011, The Astrophysical Journal, 743, 40

Bustamante S., Sparre M., Springel V., Grand R. J. J., 2018, Monthly Notices of the Royal Astronomical Society, 479, 3381

Callingham T. M., et al., 2019, Monthly Notices of the Royal Astronomical Society, 484, 5453

Calvi V., et al., 2016, The Astrophysical Journal, 817, 120

Calzetti D., Armus L., Bohlin R. C., Kinney A. L., Koornneef J., Storchi-Bergmann T., 2000, The Astrophysical Journal, 533, 682

Campbell D. J. R., et al., 2017, Monthly Notices of the Royal Astronomical Society, 469, 2335

Camps P., Baes M., 2015, Astronomy and Computing, 9, 20

Camps P., Baes M., Saftly W., 2013, Astronomy & Astrophysics, 560, A35

Carlesi E., et al., 2016, Monthly Notices of the Royal Astronomical Society, 458, 900

Cautun M., van de Weygaert R., Jones B. J. T., 2013, Monthly Notices of the Royal Astronomical Society, 429, 1286

Cautun M., Bose S., Frenk C. S., Guo Q., Han J., Hellwing W. A., Sawala T., Wang W., 2015, Monthly Notices of the Royal Astronomical Society, 452, 3838

Cautun M., Deason A. J., Frenk C. S., McAlpine S., 2019, Monthly Notices of the Royal Astronomical Society, 483, 2185

Chabrier G., 2003, Publications of the Astronomical Society of the Pacific, 115, 763

Charlot S., Fall S. M., 2000, The Astrophysical Journal, 539, 718

Chiti A., et al., 2021, Nature Astronomy, 5, 392

Choi J., Dotter A., Conroy C., Cantiello M., Paxton B., Johnson B. D., 2016, The Astrophysical Journal, 823, 102

Cole S., Aragon-Salamanca A., Frenk C. S., Navarro J. F., Zepf S. E., 1994, Monthly Notices of the Royal Astronomical Society, 271, 781

Cole S., Lacey C. G., Baugh C. M., Frenk C. S., 2000, Monthly Notices of the Royal Astronomical Society, 319, 168

Colín P., Avila-Reese V., Valenzuela O., 2000, The Astrophysical Journal, 542, 622

Conroy C., Gunn J. E., 2010, The Astrophysical Journal, 712, 833

Conroy C., Gunn J. E., White M., 2009, The Astrophysical Journal, 699, 486

Conroy C., Naidu R. P., Zaritsky D., Bonaca A., Cargile P., Johnson B. D., Caldwell N., 2019, The Astrophysical Journal, 887, 237

Cooper A. P., et al., 2010, Monthly Notices of the Royal Astronomical Society, 406, 744

Correa C. A., Schaye J., Clauwens B., Bower R. G., Crain R. A., Schaller M., Theuns T., Thob A. C. R., 2017, Monthly Notices of the Royal Astronomical Society, 472, L45

Correa Magnus L., Vasiliev E., 2022, Monthly Notices of the Royal Astronomical Society, 511, 2610

Couchman H. M. P., Rees M. J., 1986, Monthly Notices of the Royal Astronomical Society, 221, 53

Cowley W. I., Baugh C. M., Cole S., Frenk C. S., Lacey C. G., 2018, Monthly Notices of the Royal Astronomical Society, 474, 2352

Cox T. J., Jonsson P., Primack J. R., Somerville R. S., 2006, Monthly Notices of the Royal Astronomical Society, 373, 1013

Cox T. J., Jonsson P., Somerville R. S., Primack J. R., Dekel A., 2008, Monthly Notices of the Royal Astronomical Society, 384, 386

Crain R. A., et al., 2015, Monthly Notices of the Royal Astronomical Society, 450, 1937

Davis M., Huchra J., Latham D. W., Tonry J., 1982, The Astrophysical Journal, 253, 423

Davis M., Efstathiou G., Frenk C. S., White S. D. M., 1985, The Astrophysical Journal, 292, 371

Deason A. J., Belokurov V., Evans N. W., 2011, Monthly Notices of the Royal Astronomical Society, 416, 2903

Deason A. J., Belokurov V., Erkal D., Koposov S. E., Mackey D., 2017, Monthly Notices of the Royal Astronomical Society, 467, 2636

Deason A. J., Belokurov V., Koposov S. E., Lancaster L., 2018, The Astrophysical Journal, 862, L1

Deason A. J., Belokurov V., Sanders J. L., 2019, Monthly Notices of the Royal Astronomical Society, 490, 3426

Deason A. J., Fattahi A., Frenk C. S., Grand R. J. J., Oman K. A., Garrison-Kimmel S., Simpson C. M., Navarro J. F., 2020, Monthly Notices of the Royal Astronomical Society, 496, 3929

Deason A. J., Bose S., Fattahi A., Amorisco N. C., Hellwing W., Frenk C. S., 2022, Monthly Notices of the Royal Astronomical Society, 511, 4044

Debuhr J., Quataert E., Ma C.-P., Hopkins P., 2010, Monthly Notices of the Royal Astronomical Society, 406, L55

Debuhr J., Quataert E., Ma C.-P., 2011, Monthly Notices of the Royal Astronomical Society, 412, 1341

Dekker A., Ando S., Correa C. A., Ng K. C., 2022, Physical Review D, 106, 123026

Di Matteo P., Haywood M., Lehnert M. D., Katz D., Khoperskov S., Snaith O. N., Gómez A., Robichon N., 2019, Astronomy and Astrophysics, 632, A4

Dierickx M. I. P., Loeb A., 2017, The Astrophysical Journal, 836, 92

Digby R., et al., 2019, Monthly Notices of the Royal Astronomical Society, 485, 5423

Dodelson S., Widrow L. M., 1994, Physical Review Letters, 72, 17

Doroshkevich A. G., Zel'dovich Y. B., Novikov I. D., 1967, Soviet Astronomy, 11, 233

Dotter A., 2016, The Astrophysical Journal Supplement Series, 222, 8

Drlica-Wagner A., et al., 2015, The Astrophysical Journal, 813, 109

Efstathiou G., 1992, Monthly Notices of the Royal Astronomical Society, 256, 43P

Eggen O. J., Lynden-Bell D., Sandage A. R., 1962, The Astrophysical Journal, 136, 748

Elbert O. D., Bullock J. S., Garrison-Kimmel S., Rocha M., Oñorbe J., Peter A. H. G., 2015, Monthly Notices of the Royal Astronomical Society, 453, 29

Elias L. M., Sales L. V., Helmi A., Hernquist L., 2020, Monthly Notices of the Royal Astronomical Society, 495, 29

Erkal D., Belokurov V. A., 2020, Monthly Notices of the Royal Astronomical Society, 495, 2554

Erkal D., et al., 2019, Monthly Notices of the Royal Astronomical Society, 487, 2685

Evans N. W., 2020, Proceedings of the International Astronomical Union, 14, 113

Evans T. A., Fattahi A., Deason A. J., Frenk C. S., 2020, Monthly Notices of the Royal Astronomical Society

Fakhouri O., Ma C.-P., 2008, Monthly Notices of the Royal Astronomical Society, 386, 577

Fakhouri O., Ma C.-P., 2009, Monthly Notices of the Royal Astronomical Society, 394, 1825

Fakhouri O., Ma C.-P., Boylan-Kolchin M., 2010, Monthly Notices of the Royal Astronomical Society, 406, 2267

Fardal M. A., van der Marel R. P., Law D. R., Sohn S. T., Sesar B., Hernitschek N., Rix H.-W., 2019, Monthly Notices of the Royal Astronomical Society, 483, 4724

Fattahi A., et al., 2016, Monthly Notices of the Royal Astronomical Society, 457, 844

Fattahi A., et al., 2019, Monthly Notices of the Royal Astronomical Society, 484, 4471

Fattahi A., et al., 2020, Monthly Notices of the Royal Astronomical Society, 497, 4459

Ferrero I., Abadi M. G., Navarro J. F., Sales L. V., Gurovich S., 2012, Monthly Notices of the Royal Astronomical Society, 425, 2817

Finkelstein S. L., et al., 2015, The Astrophysical Journal, 810, 71

Font A. S., Johnston K. V., Bullock J. S., Robertson B. E., 2006, The Astrophysical Journal, 646, 886

Font A. S., et al., 2020, Monthly Notices of the Royal Astronomical Society, 498, 1765

Forbes D. A., 2020, Monthly Notices of the Royal Astronomical Society, 493, 847

Formaggio J. A., de Gouvêa A. L. C., Robertson R. G. H., 2021, Physics Reports, 914, 1

Fragkoudi F., et al., 2020, Monthly Notices of the Royal Astronomical Society, 494, 5936

Frenk C. S., White S. D. M., Davis M., 1983, The Astrophysical Journal, 271, 417

Frenk C. S., et al., 1999, The Astrophysical Journal, 525, 554

Gaia Collaboration et al., 2018, Astronomy and Astrophysics, 616, A1

Gallart C., Bernard E. J., Brook C. B., Ruiz-Lara T., Cassisi S., Hill V., Monelli M., 2019, Nature Astronomy, 3, 932

Gao L., White S. D. M., Jenkins A., Frenk C. S., Springel V., 2005, Monthly Notices of the Royal Astronomical Society, 363, 379

Garavito-Camargo N., Besla G., Laporte C. F. P., Johnston K. V., Gomez F. A., Watkins L. L., 2019, The Astrophysical Journal, 884, 51

Garrison-Kimmel S., Bullock J. S., Boylan-Kolchin M., Bardwell E., 2017, Monthly Notices of the Royal Astronomical Society, 464, 3108

Garrison-Kimmel S., et al., 2019, Monthly Notices of the Royal Astronomical Society, 487, 1380

Genel S., Bouché N., Naab T., Sternberg A., Genzel R., 2010, The Astrophysical Journal, 719, 229

Genina A., et al., 2018, Monthly Notices of the Royal Astronomical Society, 474, 1398

Gilmore G., et al., 2012, The Messenger, 147, 25

Gomez F. A., Besla G., Carpintero D. D., Villalobos A., O'Shea B. W., Bell E. F., 2015, The Astrophysical Journal, 802, 128

Gottlöber S., Klypin A., Kravtsov A. V., 2001, The Astrophysical Journal, 546, 223

Hahn O., Abel T., 2011, Monthly Notices of the Royal Astronomical Society, 415, 2101

Hanany S., et al., 2000, The Astrophysical Journal, 545, L5

Hargis J. R., Willman B., Peter A. H. G., 2014, The Astrophysical Journal, 795, L13

Harmsen B., Monachesi A., Bell E. F., de Jong R. S., Bailin J., Radburn-Smith D. J., Holwerda B. W., 2017, Monthly Notices of the Royal Astronomical Society, 466, 1491

Harris J., 2007, The Astrophysical Journal, 658, 345

Haywood M., Di Matteo P., Lehnert M. D., Snaith O., Khoperskov S., Gómez A., 2018, The Astrophysical Journal, 863, 113

Hellwing W. A., Frenk C. S., Cautun M., Bose S., Helly J., Jenkins A., Sawala T., Cytowski M., 2016, Monthly Notices of the Royal Astronomical Society, 457, 3492

Hellwing W. A., Cautun M., van de Weygaert R., Jones B. T., 2021, Physical Review D, 103, 063517

Helmi A., Babusiaux C., Koppelman H. H., Massari D., Veljanoski J., Brown A. G. A., 2018, Nature, 563, 85

Hernquist L., 1989, Nature, 340, 687

Hernquist L., 1992, The Astrophysical Journal, 400, 460

Hester J. A., Tasitsiomi A., 2010, The Astrophysical Journal, 715, 342

Hoffman Y., Ribak E., 1991, The Astrophysical Journal, 380, L5

Hopkins P. F., Hernquist L., Cox T. J., Di Matteo T., Robertson B., Springel V., 2006, The Astrophysical Journal Supplement Series, 163, 1

Horta D., et al., 2021, Monthly Notices of the Royal Astronomical Society, 500, 1385

Iršič V., et al., 2017, Physical Review D, 96, 023522

Jasche J., Wandelt B. D., 2013, The Astrophysical Journal, 779, 15

Jenkins A., 2013, Monthly Notices of the Royal Astronomical Society, 434, 2094

Jenkins A., Frenk C. S., White S. D. M., Colberg J. M., Cole S., Evrard A. E., Couchman H. M. P., Yoshida N., 2001, Monthly Notices of the Royal Astronomical Society, 321, 372

Jiang L., Helly J. C., Cole S., Frenk C. S., 2014, Monthly Notices of the Royal Astronomical Society, 440, 2115

Johansson P. H., Naab T., Burkert A., 2009, The Astrophysical Journal, 690, 802

Johnston K. V., 1998, The Astrophysical Journal, 495, 297

Johnston K. V., Hernquist L., Bolte M., 1996, The Astrophysical Journal, 465, 278

Kallivayalil N., Marel R. P. v. d., Besla G., Anderson J., Alcock C., 2013, The Astrophysical Journal, 764, 161

Katz N., 1992, The Astrophysical Journal, 391, 502

Katz N., White S. D. M., 1993, The Astrophysical Journal, 412, 455

Kazantzidis S., Bullock J. S., Zentner A. R., Kravtsov A. V., Moustakas L. A., 2008, The Astrophysical Journal, 688, 254

Kennicutt Jr. R. C., Keel W. C., van der Hulst J. M., Hummel E., Roettiger K. A., 1987, The Astronomical Journal, 93, 1011

Kim S. Y., Peter A. H. G., Hargis J. R., 2018, Physical Review Letters, 121, 211302

Kirby E. N., Bullock J. S., Boylan-Kolchin M., Kaplinghat M., Cohen J. G., 2014, Monthly Notices of the Royal Astronomical Society, 439, 1015

Klypin A., Kravtsov A. V., Valenzuela O., Prada F., 1999, The Astrophysical Journal, 522, 82

Komatsu E., et al., 2011, The Astrophysical Journal Supplement Series, 192, 18

Koposov S., Belokurov V., 2008, Conference proceedings, 5, 195

Koposov S., Belokurov V., Torrealba G., Evans W., 2015, Conference proceedings, 29, 2256759

Koposov S. E., et al., 2023, Monthly Notices of the Royal Astronomical Society, 521, 4936

Koppelman H. H., Helmi A., Massari D., Price-Whelan A. M., Starkenburg T. K., 2019, Astronomy and Astrophysics, 631, L9

Kriek M., Conroy C., 2013, The Astrophysical Journal Letters, 775, L16

Kruijssen J. M. D., Zwart S. F. P., 2009, The Astrophysical Journal, 698, L158

Kruijssen J. M. D., et al., 2020, Monthly Notices of the Royal Astronomical Society, 498, 2472

Kunkel W. E., Demers S., 1976, Conference proceedings, 182, 241

Lacey C. G., et al., 2016, Monthly Notices of the Royal Astronomical Society, 462, 3854

Lagos C. D. P., Lacey C. G., Baugh C. M., Bower R. G., Benson A. J., 2011, Monthly Notices of the Royal Astronomical Society, 416, 1566

Laporte C. F. P., Gómez F. A., Besla G., Johnston K. V., Garavito-Camargo N., 2018, Monthly Notices of the Royal Astronomical Society, 473, 1218

Larson R. B., Tinsley B. M., 1978, The Astrophysical Journal, 219, 46

Libeskind N. I., Frenk C. S., Cole S., Helly J. C., Jenkins A., Navarro J. F., Power C., 2005, Monthly Notices of the Royal Astronomical Society, 363, 146

Libeskind N. I., et al., 2020, Monthly Notices of the Royal Astronomical Society, 498, 2968

Licquia T. C., Newman J. A., 2015, The Astrophysical Journal, 806, 96

Liu L., Gerke B. F., Wechsler R. H., Behroozi P. S., Busha M. T., 2011, The Astrophysical Journal, 733, 62

Loeb A., Barkana R., 2001, Annual Review of Astronomy and Astrophysics, 39, 19

Longeard N., et al., 2022, Monthly Notices of the Royal Astronomical Society, 516, 2348

Lovell M. R., et al., 2012, Monthly Notices of the Royal Astronomical Society, 420, 2318

Lovell M. R., Frenk C. S., Eke V. R., Jenkins A., Gao L., Theuns T., 2014, Monthly Notices of the Royal Astronomical Society, 439, 300

Lovell M. R., et al., 2016, Monthly Notices of the Royal Astronomical Society, 461, 60

Lovell M. R., Cautun M., Frenk C. S., Hellwing W. A., Newton O., 2021, Monthly Notices of the Royal Astronomical Society, 507, 4826

Lynden-Bell D., 1976, Monthly Notices of the Royal Astronomical Society, 174, 695

Lyubimov V. A., Novikov E. G., Nozik V. Z., Tret'yakov E. F., Kozik V. S., Myasoedov N. F., 1981, Soviet Journal of Experimental and Theoretical Physics, 54, 616

Mackereth J. T., Bovy J., 2020, Monthly Notices of the Royal Astronomical Society, 492, 3631

Mackereth J. T., et al., 2019, Monthly Notices of the Royal Astronomical Society, 482, 3426

Mackey A. D., Koposov S. E., Erkal D., Belokurov V., Da Costa G. S., Gómez F. A., 2016, Monthly Notices of the Royal Astronomical Society, 459, 239

Mackey D., Koposov S., Da Costa G., Belokurov V., Erkal D., Kuzma P., 2018, The Astrophysical Journal, 858, L21

Majewski S. R., et al., 2017, The Astronomical Journal, 154, 94

Malhan K., et al., 2022, The Astrophysical Journal, 926, 107

Maneewongvatana S., Mount D. M., 1999, arXiv e-prints

van der Marel R. P., Kallivayalil N., 2014, The Astrophysical Journal, 781, 121

van der Marel R. P., Alves D. R., Hardy E., Suntzeff N. B., 2002, The Astronomical Journal, 124, 2639

Marinacci F., et al., 2018, Monthly Notices of the Royal Astronomical Society, 480, 5113

Martell S. L., et al., 2017, Monthly Notices of the Royal Astronomical Society, 465, 3203

Mathis H., Lemson G., Springel V., Kauffmann G., White S. D. M., Eldar A., Dekel A., 2002,

Monthly Notices of the Royal Astronomical Society, 333, 739

Matsuno T., Aoki W., Suda T., 2019, The Astrophysical Journal, 874, L35

McAlpine S., et al., 2016, Astronomy and Computing, 15, 72

McAlpine S., et al., 2022, Monthly Notices of the Royal Astronomical Society

McConnachie A. W., 2012, The Astronomical Journal, 144, 4

McGibbon R. J., Khochfar S., 2023, Monthly Notices of the Royal Astronomical Society, 523, 5583

Melchiorri A., et al., 2000, The Astrophysical Journal, 536, L63

Metz M., Kroupa P., Libeskind N. I., 2008, The Astrophysical Journal, 680, 287

Mihos J. C., Hernquist L., 1994, The Astrophysical Journal, 425, L13

Moore B., 1994, Nature, 370, 629

Moore B., Ghigna S., Governato F., Lake G., Quinn T., Stadel J., Tozzi P., 1999, The Astrophysical Journal, 524, L19

Moster B. P., Macciò A. V., Somerville R. S., Johansson P. H., Naab T., 2010, Monthly Notices of the Royal Astronomical Society, 403, 1009

Munshi F., Brooks A. M., Applebaum E., Christensen C. R., Quinn T., Sligh S., 2021, The Astrophysical Journal, 923, 35

Murante G., et al., 2004, The Astrophysical Journal, 607, L83

Murante G., Poglio E., Curir A., Villalobos A., 2010, The Astrophysical Journal, 716, L115

Myeong G. C., Evans N. W., Belokurov V., Sanders J. L., Koposov S. E., 2018, The Astrophysical Journal Letters, 863, L28

Myeong G. C., Vasiliev E., Iorio G., Evans N. W., Belokurov V., 2019, Monthly Notices of the Royal Astronomical Society, 488, 1235

Naab T., Burkert A., 2003, The Astrophysical Journal, 597, 893

Naidu R. P., Conroy C., Bonaca A., Johnson B. D., Ting Y.-S., Caldwell N., Zaritsky D., Cargile P. A., 2020, The Astrophysical Journal, 901, 48

Naidu R. P., et al., 2021, The Astrophysical Journal, 923, 92

Naiman J. P., et al., 2018, Monthly Notices of the Royal Astronomical Society, 477, 1206

Navarrete C., et al., 2019, Monthly Notices of the Royal Astronomical Society, 483, 4160

Necib L., et al., 2020, Nature Astronomy, 4, 1078

Negroponte J., White S. D. M., 1983, Monthly Notices of the Royal Astronomical Society, 205, 1009

Nelson D., et al., 2018, Monthly Notices of the Royal Astronomical Society, 475, 624

Nelson D., et al., 2019, Monthly Notices of the Royal Astronomical Society, 490, 3234

Newberg H. J., Yanny B., Willett B. A., 2009, The Astrophysical Journal, 700, L61

Newton O., Cautun M., Jenkins A., Frenk C. S., Helly J. C., 2018, Monthly Notices of the Royal Astronomical Society, 479, 2853

Newton O., Cautun M., Jenkins A., Frenk C. S., Helly J. C., 2019, Conference proceedings, 344,

109

Nidever D. L., et al., 2019, The Astrophysical Journal, 874, 118

Noll S., Burgarella D., Giovannoli E., Buat V., Marcillac D., Munoz-Mateos J. C., 2009, Astronomy and Astrophysics, 507, 1793

Oesch P. A., et al., 2013, The Astrophysical Journal, 773, 75

Oesch P. A., et al., 2014, The Astrophysical Journal, 786, 108

Oesch P. A., Bouwens R. J., Illingworth G. D., Labbé I., Stefanon M., 2018, The Astrophysical Journal, 855, 105

Okamoto T., Frenk C. S., Jenkins A., Theuns T., 2010, Monthly Notices of the Royal Astronomical Society, 406, 208

Patej A., Loeb A., 2015, The Astrophysical Journal, 815, L28

Patel E., Besla G., Sohn S. T., 2017a, Monthly Notices of the Royal Astronomical Society, 464, 3825

Patel E., Besla G., Mandel K., 2017b, Monthly Notices of the Royal Astronomical Society, 468, 3428

Paxton B., Bildsten L., Dotter A., Herwig F., Lesaffre P., Timmes F., 2011, The Astrophysical Journal Supplement Series, 192, 3

Paxton B., et al., 2013, The Astrophysical Journal Supplement Series, 208, 4

Paxton B., et al., 2015, The Astrophysical Journal Supplement Series, 220, 15

Penarrubia J., Walker M. G., Gilmore G., 2009, Monthly Notices of the Royal Astronomical Society, 399, 1275

Perlmutter S., et al., 1999, The Astrophysical Journal, 517, 565

Peñarrubia J., Gómez F. A., Besla G., Erkal D., Ma Y.-Z., 2016, Monthly Notices of the Royal Astronomical Society: Letters, 456, L54

Pfeffer J. L., Trujillo-Gomez S., Kruijssen J. M. D., Crain R. A., Hughes M. E., Reina-Campos M., Bastian N., 2020, Monthly Notices of the Royal Astronomical Society, 499, 4863

Pietrzyński G., et al., 2013, Nature, 495, 76

Pillepich A., et al., 2018, Monthly Notices of the Royal Astronomical Society, 475, 648

Pillepich A., et al., 2019, Monthly Notices of the Royal Astronomical Society, 490, 3196

Planck Collaboration et al., 2014, Astronomy and Astrophysics, 571, A1

Planck Collaboration et al., 2016, Astronomy and Astrophysics, 594, A13

Press W. H., Schechter P., 1974, The Astrophysical Journal, 187, 425

Purcell C. W., Kazantzidis S., Bullock J. S., 2009, The Astrophysical Journal, 694, L98

Quinn P. J., Hernquist L., Fullagar D. P., 1993, The Astrophysical Journal, 403, 74

Read J. I., Lake G., Agertz O., Debattista V. P., 2008, Monthly Notices of the Royal Astronomical Society, 389, 1041

Read J. I., Agertz O., Collins M. L. M., 2016, Monthly Notices of the Royal Astronomical Society, 459, 2573

Reddy N. A., et al., 2015, The Astrophysical Journal, 806, 259

Reddy N. A., et al., 2018, The Astrophysical Journal, 853, 56

Rees M. J., 1986, Monthly Notices of the Royal Astronomical Society, 218, 25P

Riess A. G., et al., 1998, The Astronomical Journal, 116, 1009

Rocha M., Peter A. H. G., Bullock J., 2012, Monthly Notices of the Royal Astronomical Society, 425, 231

Rocha M., Peter A. H. G., Bullock J. S., Kaplinghat M., Garrison-Kimmel S., Oñorbe J., Moustakas L. A., 2013, Monthly Notices of the Royal Astronomical Society, 430, 81

Roman N. G., 1950, The Astrophysical Journal, 112, 554

Saftly W., Baes M., Camps P., 2014, Astronomy & Astrophysics, 561, A77

Sales L., 2016, HST Proposal, p. 14582

Sales L. V., Navarro J. F., Theuns T., Schaye J., White S. D. M., Frenk C. S., Crain R. A., Dalla Vecchia C., 2012, Monthly Notices of the Royal Astronomical Society, 423, 1544

Sanchez-Blazquez P., et al., 2006, Monthly Notices of the Royal Astronomical Society, 371, 703

Sanders D. B., Soifer B. T., Elias J. H., Madore B. F., Matthews K., Neugebauer G., Scoville N. Z., 1988, The Astrophysical Journal, 325, 74

Santistevan I. B., Wetzel A., El-Badry K., Bland-Hawthorn J., Boylan-Kolchin M., Bailin J., Faucher-Giguère C.-A., Benincasa S., 2020, Monthly Notices of the Royal Astronomical Society, 497, 747

Santos-Santos I. M. E., Fattahi A., Sales L. V., Navarro J. F., 2021, Monthly Notices of the Royal Astronomical Society, 504, 4551

Savitzky A., Golay M. J. E., 1964, Analytical Chemistry, 36, 1627

Savorgnan G. A. D., Graham A. W., Marconi A., Sani E., 2016, The Astrophysical Journal, 817, 21

Sawala T., et al., 2015, Monthly Notices of the Royal Astronomical Society, 448, 2941

Sawala T., et al., 2016, Monthly Notices of the Royal Astronomical Society, 457, 1931

Sawala T., McAlpine S., Jasche J., Lavaux G., Jenkins A., Johansson P. H., Frenk C. S., 2022, Monthly Notices of the Royal Astronomical Society, 509, 1432

Schaller M., et al., 2015a, Monthly Notices of the Royal Astronomical Society, 451, 1247

Schaller M., Dalla Vecchia C., Schaye J., Bower R. G., Theuns T., Crain R. A., Furlong M., McCarthy I. G., 2015b, Monthly Notices of the Royal Astronomical Society, 454, 2277

Schawinski K., et al., 2014, Monthly Notices of the Royal Astronomical Society, 440, 889

Schaye J., et al., 2015, Monthly Notices of the Royal Astronomical Society, 446, 521

Schechter P., 1976, The Astrophysical Journal, 203, 297

Schneider A., Smith R. E., Macciò A. V., Moore B., 2012, Monthly Notices of the Royal Astronomical Society, 424, 684

Schommer R. A., Suntzeff N. B., Olszewski E. W., Harris H. C., 1992, The Astronomical Journal, 103, 447

Searle L., Zinn R., 1978, The Astrophysical Journal, 225, 357

Seaton M. J., 1979, Monthly Notices of the Royal Astronomical Society, 187, 73P

Sestito F., et al., 2023, arXiv e-prints

Shao S., Gao L., Theuns T., Frenk C. S., 2013, Monthly Notices of the Royal Astronomical Society, 430, 2346

Shao S., Cautun M., Frenk C. S., 2019, Monthly Notices of the Royal Astronomical Society, 488, 1166

Shipp N., et al., 2021, The Astrophysical Journal, 923, 149

Simpson C. M., Grand R. J. J., Gómez F. A., Marinacci F., Pakmor R., Springel V., Campbell D. J. R., Frenk C. S., 2018, Monthly Notices of the Royal Astronomical Society, 478, 548

Somerville R. S., Gilmore R. C., Primack J. R., Domínguez A., 2012, Monthly Notices of the Royal Astronomical Society, 423, 1992

Song M., et al., 2016, The Astrophysical Journal, 825, 5

Sorce J. G., Dubois Y., Blaizot J., McGee S. L., Yepes G., Knebe A., 2021, Monthly Notices of the Royal Astronomical Society, 504, 2998

Spergel D. N., Steinhardt P. J., 2000, Physical Review Letters, 84, 3760

Spergel D. N., et al., 2003, The Astrophysical Journal Supplement Series, 148, 175

Springel V., 2005, Monthly Notices of the Royal Astronomical Society, 364, 1105

Springel V., 2010, Monthly Notices of the Royal Astronomical Society, 401, 791

Springel V., Di Matteo T., Hernquist L., 2005a, Monthly Notices of the Royal Astronomical Society, 361, 776

Springel V., et al., 2005b, Nature, 435, 629

Springel V., et al., 2008, Monthly Notices of the Royal Astronomical Society, 391, 1685

Springel V., et al., 2018, Monthly Notices of the Royal Astronomical Society, 475, 676

Stanimirović S., Staveley-Smith L., Jones P. A., 2004, The Astrophysical Journal, 604, 176

Stefanon M., et al., 2017, The Astrophysical Journal, 851, 43

Steinmetz M., et al., 2020, The Astronomical Journal, 160, 82

Tacchella S., Bose S., Conroy C., Eisenstein D. J., Johnson B. D., 2018, The Astrophysical Journal, 868, 92

Tollerud E. J., Bullock J. S., Strigari L. E., Willman B., 2008, The Astrophysical Journal, 688, 277

Tollerud E. J., Barton E. J., Bullock J. S., Trinh C., 2011, EAS Publications Series, 48, 455

Tolstoy E., Hill V., Tosi M., 2009, Annual Review of Astronomy and Astrophysics, 47, 371

Tomczak A. R., et al., 2014, The Astrophysical Journal, 783, 85

Tononi J., Torres S., García-Berro E., Camisassa M. E., Althaus L. G., Rebassa-Mansergas A., 2019, Astronomy & Astrophysics, 628, A52

Toomre A., 1977. `https://ui.adsabs.harvard.edu/abs/1977egsp.conf..401T`

Toomre A., Toomre J., 1972, The Astrophysical Journal, 178, 623

Tormen G., Bouchet F. R., White S. D. M., 1997, Monthly Notices of the Royal Astronomical

Society, 286, 865

Trayford J. W., et al., 2015, Monthly Notices of the Royal Astronomical Society, 452, 2879

Trayford J. W., et al., 2017, Monthly Notices of the Royal Astronomical Society, 470, 771

Vasiliev E., Belokurov V., Erkal D., 2021, Monthly Notices of the Royal Astronomical Society, 501, 2279

Velazquez H., White S. D. M., 1999, Monthly Notices of the Royal Astronomical Society, 304, 254

Viel M., Becker G. D., Bolton J. S., Haehnelt M. G., 2013, Physical Review D, 88, 043502

Villalobos A., Helmi A., 2008, Monthly Notices of the Royal Astronomical Society, 391, 1806

Vogelsberger M., Zavala J., Loeb A., 2012, Monthly Notices of the Royal Astronomical Society, 423, 3740

Vogelsberger M., et al., 2020, Monthly Notices of the Royal Astronomical Society, 492, 5167

Walker A. R., 2012, Astrophysics and Space Science, 341, 43

Waller F., et al., 2023, Monthly Notices of the Royal Astronomical Society, 519, 1349

Wang J., Frenk C. S., Navarro J. F., Gao L., Sawala T., 2012, Monthly Notices of the Royal Astronomical Society, 424, 2715

Wang H., Mo H. J., Yang X., Jing Y. P., Lin W. P., 2014, The Astrophysical Journal, 794, 94

Wang H., et al., 2016, The Astrophysical Journal, 831, 164

Wang L., et al., 2017, Monthly Notices of the Royal Astronomical Society, 468, 4579

Wetzel A. R., Hopkins P. F., Kim J.-h., Faucher-Giguère C.-A., Kereš D., Quataert E., 2016, The Astrophysical Journal Letters, 827, L23

Whitaker K. E., Pope A., Cybulski R., Casey C. M., Popping G., Yun M. S., 2017, The Astrophysical Journal, 850, 208

White S. D. M., Rees M. J., 1978, Monthly Notices of the Royal Astronomical Society, 183, 341

White S. D. M., Frenk C. S., Davis M., 1983, The Astrophysical Journal, 274, L1

Wilkins S. M., et al., 2013, Monthly Notices of the Royal Astronomical Society, 435, 2885

Williams C. C., et al., 2018, The Astrophysical Journal Supplement Series, 236, 33

Yanny B., et al., 2009, The Astronomical Journal, 137, 4377

Yepes G., Gottlöber S., Hoffman Y., 2014, New Astronomy Reviews, 58, 1

Younger J. D., Hayward C. C., Narayanan D., Cox T. J., Hernquist L., Jonsson P., 2009, Monthly Notices of the Royal Astronomical Society, 396, L66

Yuan Z., et al., 2020, The Astrophysical Journal, 891, 39

Yung L. Y. A., Somerville R. S., Finkelstein S. L., Popping G., Dave R., 2019, Monthly Notices of the Royal Astronomical Society, 483, 2983

Zentner A. R., Bullock J. S., 2003, The Astrophysical Journal, 598, 49

Zhao G., Zhao Y.-H., Chu Y.-Q., Jing Y.-P., Deng L.-C., 2012, Research in Astronomy and Astrophysics, 12, 723

Zolotov A., et al., 2012, The Astrophysical Journal, 761, 71

Zwicky F., 1933, Helvetica Physica Acta, 6, 110

APPENDIX A

The dust parameter $\tau_{\mathbf{dust}}$

The scale factor, τ_{dust}, scales like the average dust-to-metal ratio. The scale factor as a function of redshift used in Chapter 3 is the same as that in Vogelsberger et al. (2020). Below is a summary their methods and motivations (discussed in more detail in section 3.4 of Vogelsberger et al., 2020).

Numerous prior studies have indicated that the connection between dust attenuation or dust optical depth and gas metallicity and column density changes over cosmic time due to a redshift dependant dust-to-metal ratio. In numerous past theoretical investigations, a static relationship often results in a considerable overestimation of the impact of dust attenuation on high-redshift galaxies (e.g., Somerville et al., 2012; Wilkins et al., 2013; Reddy et al., 2015; Whitaker et al., 2017; Reddy et al., 2018; Yung et al., 2019).

In their study, Vogelsberger et al. (2020) conducted a χ^2 best-fitting test on 81 τ_{dust} values obtained from observations spanning the redshift range $z = 2 - 10$. The χ^2 test was weighted towards the brighter galaxies since these are the most affected by dust. The results of this process are shown in Fig. A.1 which is well described by a power law relation with $z^{-1.92}$. The redshift dependence Vogelsberger et al. (2020) found is similar to the dust relation scaling presented in Yung et al. (2019) for a similar dust model.

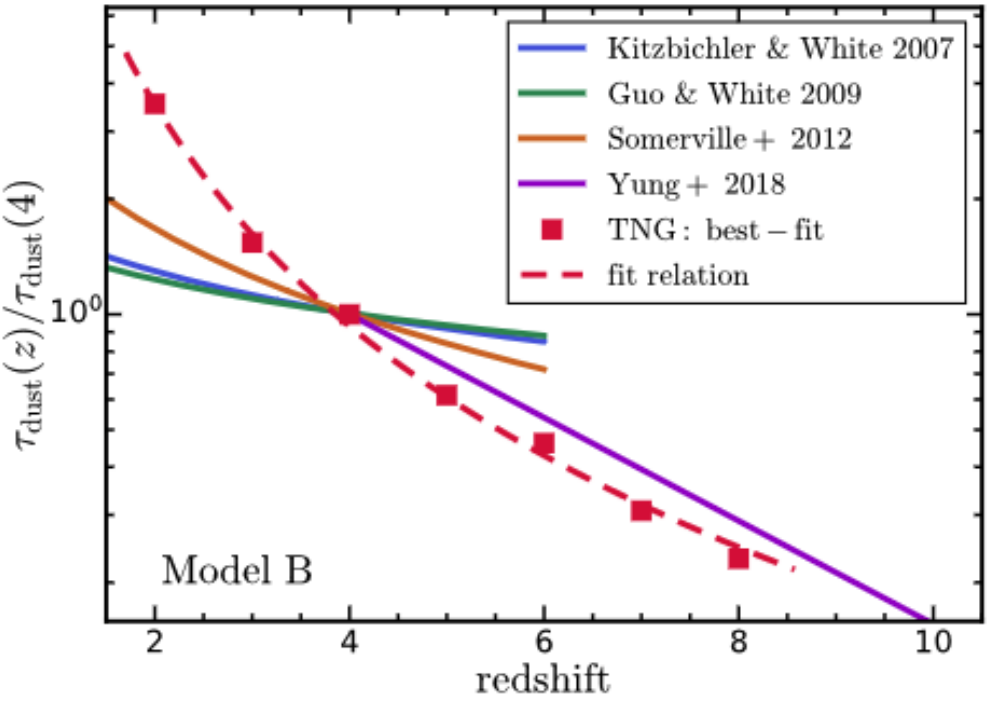

Figure A.1
The best fitting $\tau_{\rm dust}$ values. Image credit: Vogelsberger et al. (2020)

APPENDIX B

Resolution checks and magnitude corrections

We compare the dust-corrected apparent magnitudes for all galaxies in the EAGLE-Ref and EAGLE-Recal volumes in order to quantify the effects of resolution on our results. The relationship between apparent magnitude and stellar mass for the two volumes is shown in Fig. B.1. The median values for the two volumes are consistent with each other. However, as shown in the figure, there is a large amount of scatter at the low mass end for the EAGLE-Ref volume due to the lack of resolution.

In order to get a better representation of the magnitudes at the low mass end, we apply a magnitude correction to galaxies of stellar mass $M_* < 10^8\,\mathrm{M}_\odot$ as this is where the scatter in the EAGLE-Ref data starts to increase dramatically. Such corrections, however, are not necessary for brighter galaxies as these are resolved with enough star particles. (See agreement at the bright end in Fig. B.1).

For the magnitude corrections below $M_* < 10^8\,\mathrm{M}_\odot$, we model the distribution of apparent magnitudes for the higher resolution Recal50 dataset in a given mass bin between the $[5^{th} - 95^{th}]$ percentile values (shown as red errorbars on Fig. B.1) and resample values for EAGLE-Ref from this distribution. These corrections are performed at all redshifts for magnitudes with and without dust, and for all passbands used in this work.

Fig. B.2 shows the original data from EAGLE-Ref (blue points) and the new corrected magnitudes (orange points). As shown in the figure, the median values are unchanged. The corrected magnitude data points no longer show such a large scatter at the low mass end.

B.0.1 CMDs at high redshift

Fig. B.3 shows the CMDs for the m_{F115W} and m_{F200W} passbands at high redshifts. The red contours in each redshift panel highlight the regions where progenitors of MW-like galaxies are most likely to reside. As the redshift increases, the MW-like progenitors occupy a larger region of the CMD; by redshift $z = 8$, the contours cover the entirety of the CMD, but are more concentrated at fainter magnitudes and redder colours.

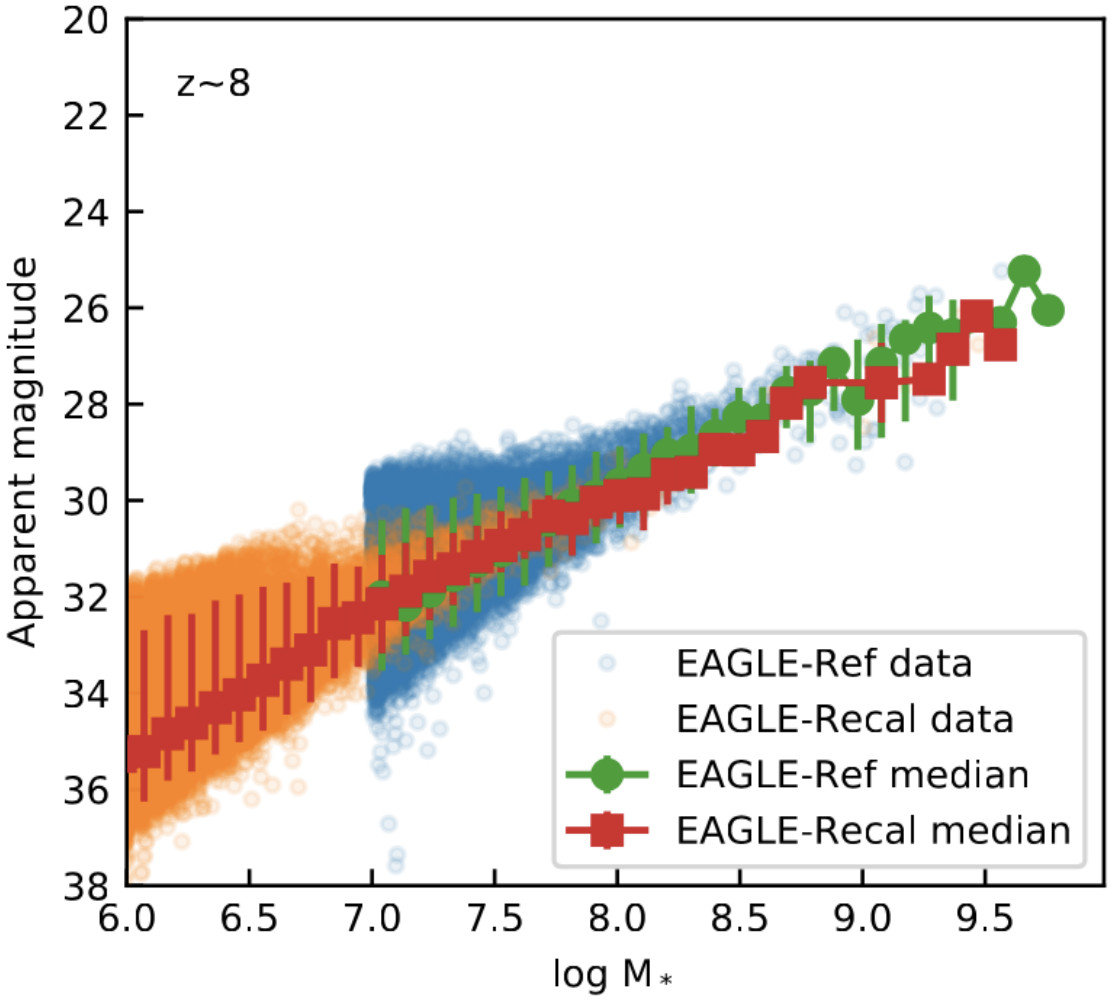

Figure B.1

The relationship between apparent magnitude and stellar mass for the EAGLE-Ref (blue points) and EAGLE-Recal (orange) volumes at $z = 8$. The median values for each sample are shown as green circles and red squares for EAGLE-Ref and EAGLE-Recal, respectively. The errorbars represent the $[5^{th} - 95^{th}]$ percentiles of the data.

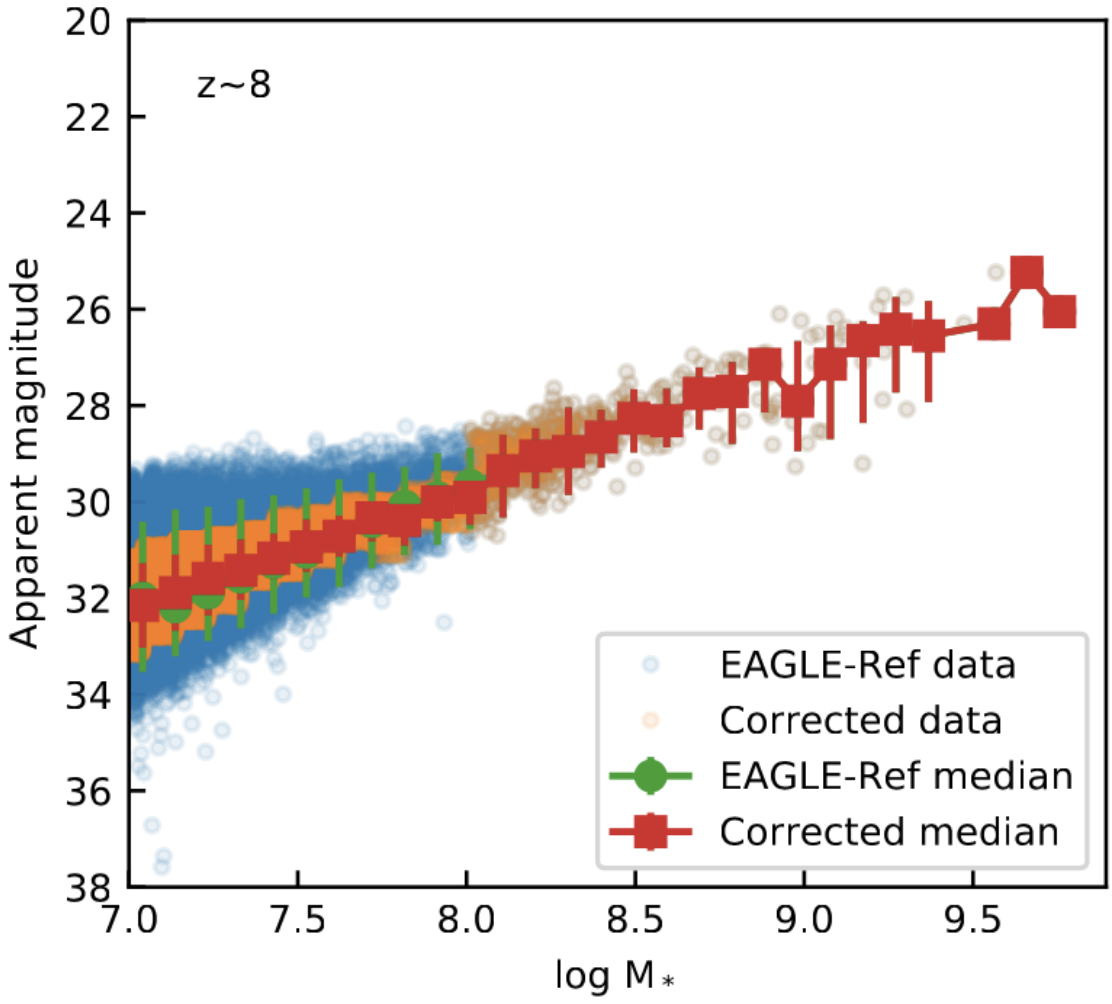

Figure B.2

The apparent magnitude-stellar mass relation for the uncorrected (blue points) and corrected (orange points) EAGLE-Ref data.

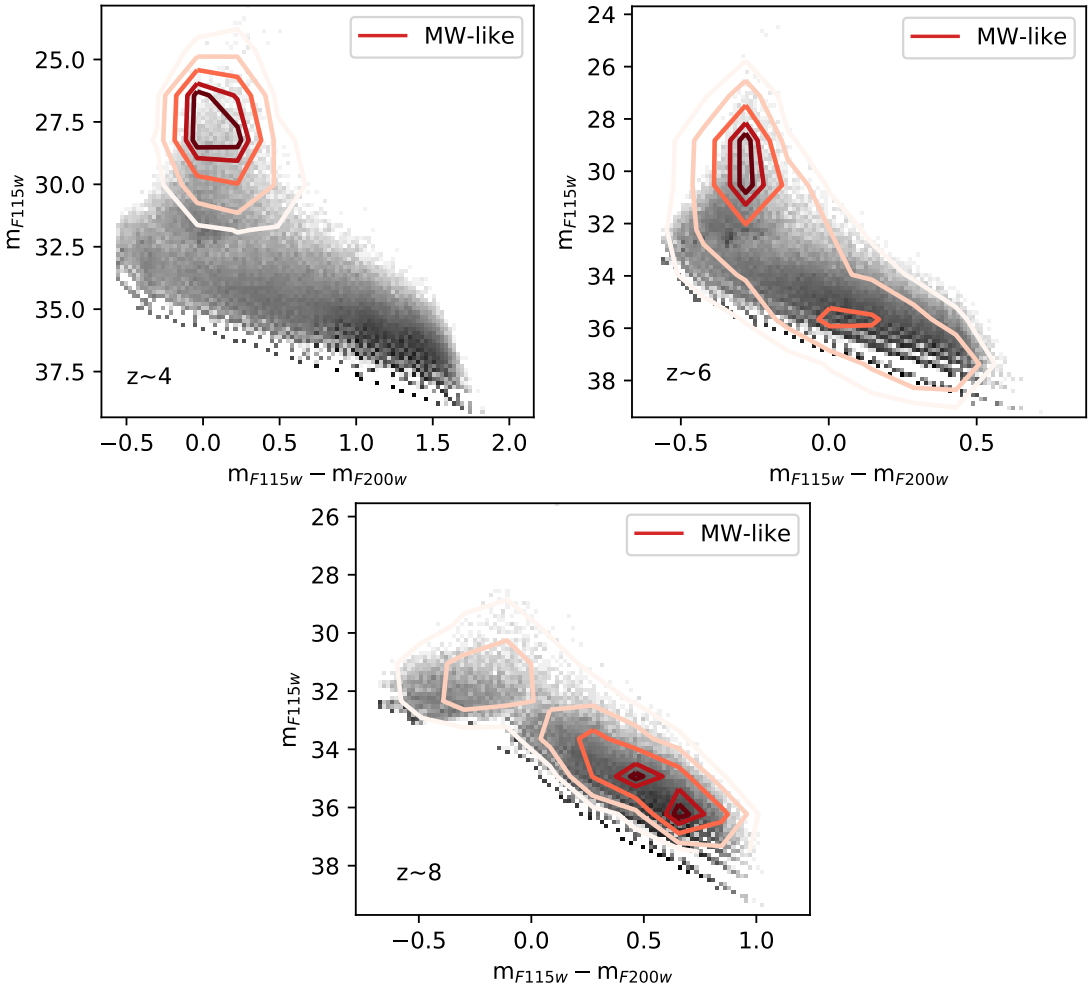

Figure B.3

CMDs for all EAGLE-Recal galaxies (grey) at redshifts $z = 4, 6, 8$ with overlaid red contours to show the region where 10, 25, 50, 75 and 90 percent of MW-like galaxies are enclosed.

B.0.2 Milky Way analogues as Lyman break galaxies

The dust-free spectra of three MW-analogues are shown in Fig. B.4. These spectra were made using the MILES Stellar library as part of FSPS, which include features such as absorption from the intergalactic medium and emission from nebulae.

The higher redshift spectra for the progenitors of these galaxies are shown as red and purple lines for $z = 6, 8$ respectively. These indicate that at these high redshifts, the progenitors of MW analogues could be seen as Lyman break galaxies in the bluer wavelength passbands, i.e. F070w, F090w and F115W. The Lyman break features of these spectra may help distinguish MW-analogues from other galaxies in the field.

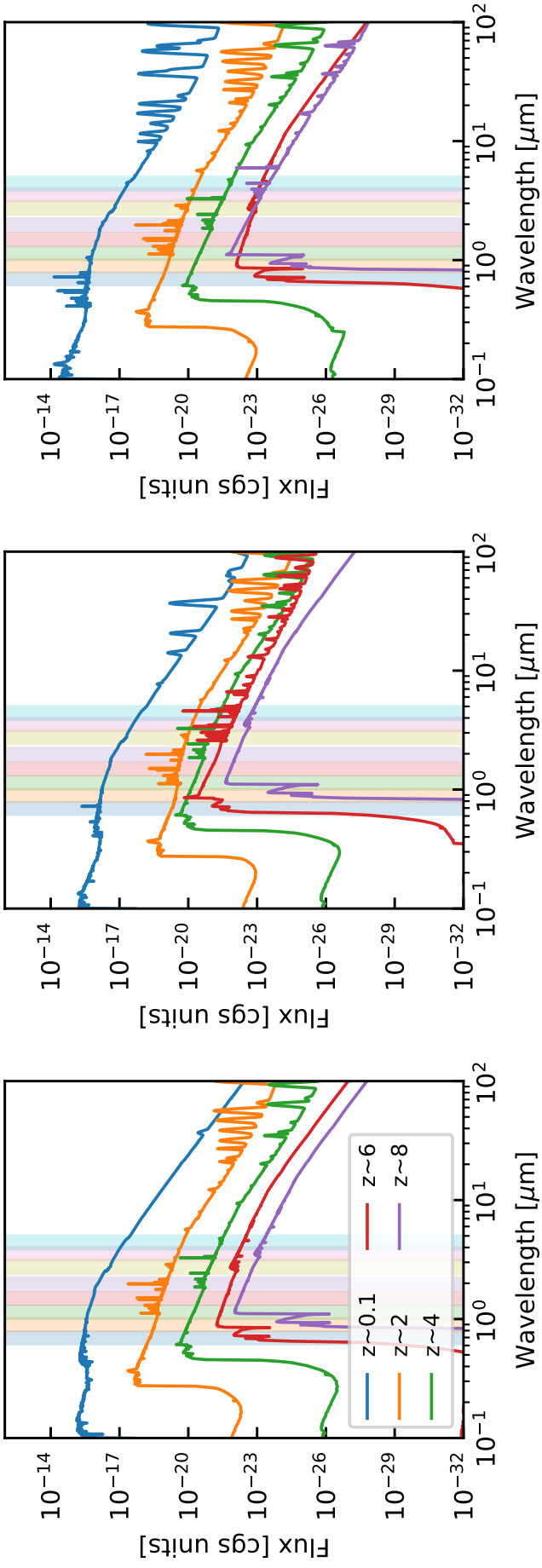

Figure B.4
The dust free spectra of the progenitors of three of the MW analogues. Spectra are shown for each galaxy at redshifts $z = 0.1, 2, 4, 6, 8$ in blue, orange, green, red, and purple respectively. The vertical coloured bands represent the *JWST*/NIRCam passbands (from left to right: F070W, F090W, F115W, F150W, F200W, F277W, F356W, F444W). MW analogues may have Lyman break features at high redshifts, i.e. $z = 6$ and 8.